



Calhoun: The NPS Institutional Archive
DSpace Repository

Theses and Dissertations

1. Thesis and Dissertation Collection, all items

1997-06

Iceland-FÆROE front structure and variability

Arends, Christopher J

Monterey, California. Naval Postgraduate School

<http://hdl.handle.net/10945/8484>

Downloaded from NPS Archive: Calhoun



Calhoun is the Naval Postgraduate School's public access digital repository for research materials and institutional publications created by the NPS community. Calhoun is named for Professor of Mathematics Guy K. Calhoun, NPS's first appointed -- and published -- scholarly author.

Dudley Knox Library / Naval Postgraduate School
411 Dyer Road / 1 University Circle
Monterey, California USA 93943

<http://www.nps.edu/library>

NPS ARCHIVE
1997
ARENDS, C.

NAVAL POSTGRADUATE SCHOOL MONTEREY, CALIFORNIA



THESIS

ICELAND-FÆROE FRONT STRUCTURE AND VARIABILITY

by

Christopher J. Arends

June 1997

Thesis Advisor:

Pierre-Marie Poulain

Approved for public release; distribution is unlimited

Thesis
A6495

UDLEY KNO. (DRY)
NAVAL POSTGRADUATE SCHOOL
MONTEREY 3042-5101

REPORT DOCUMENTATION PAGE			Form Approved OMB No. 0704-0188	
Public reporting burden for this collection of information is estimated to average 1 hour per response, including the time for reviewing instructions, searching existing sources, gathering and maintaining the data needed, and completing and reviewing the collection of information. Send comments regarding this burden estimate or any other aspect of this collection of information, including suggestions for reducing this burden to Washington Headquarters Services, Directorate for information Operations and Reports, 1215 Jefferson Davis Highway Suite 1204, Arlington, VA 22202-4312, and to the Office of Management and Budget, Paperwork Reduction Project (0704-0188), Washington, DC 20503.				
1. AGENCY USE ONLY (Leave blank)		2. REPORT DATE June 1997		3. REPORT TYPE AND DATES COVERED Master's Thesis
4. TITLE AND SUBTITLE ICELAND-FÆROE FRONT STRUCTURE AND VARIABILITY			5. FUNDING NUMBERS	
6. AUTHOR(S) Christopher J. Arends				
7. PERFORMING ORGANIZATION NAME(S) AND ADDRESS(ES) Naval Postgraduate School Monterey, CA 93943-5000			8. PERFORMING ORGANIZATION REPORT NUMBER	
9. SPONSORING/MONITORING AGENCY NAME(S) AND ADDRESS(ES)			10. SPONSORING/MONITORING AGENCY REPORT NUMBER	
11. SUPPLEMENTARY NOTES The views expressed in this thesis are those of the author and do not reflect the official policy or position of the Department of Defense or the U.S. Government.				
12a. DISTRIBUTION/AVAILABILITY STATEMENT Approved for public release; distribution is unlimited.			12b. DISTRIBUTION CODE	
13. ABSTRACT (Maximum 200 words) During the period June 1991 to August 1993, 107 Argos-tracked drifters, drogued to 15 m depth, were released in the Greenland, Iceland, and Norwegian (GIN) Seas. The drifter movements revealed the strong and spatially confined current systems along the Iceland-Færoe Front (IFF) and provided tracking of the Norwegian Atlantic Current and the general cyclonic gyre circulation in the GIN Sea. Of the 107 drifters released, 59 were selected for this study due to their proximity to the IFF. Tracked by the Argos system aboard the NOAA polar orbiters, the drifters provided accurate location and sea surface temperature (SST) data. Interpolated and low-pass-filtered position data were used to construct maps of drifter displacement and surface velocity field estimates and to study the correlation between drifter trajectories and satellite derived SST frontal features. Drifter SST data were compared to spatially and temporally coincident satellite retrieved SST data. The individual data sets were in good agreement with each other, resulting in a temperature difference of less than 1 °C. Satellite imagery used to estimate surface currents through SST feature tracking provided a snapshot of the flow field over a short time scale. The drifters revealed a distinct frontal zone (IFF) where the topographically steered flow field approached velocities of 1 m/s. This relatively strong flow became unstable as it propagated eastward and an intense eddy field developed. What began as a stable demarcation between water masses became a flow field dominated by warm and cold instabilities and intrusions. This dynamic transformation occurred over relatively short time (less than 5 days) and distance (several hundred kilometers) scales, testament to the vigorous activity in the IFF. These Lagrangian drifter measurements compose the first comprehensive, accurate near-surface velocity data set in the IFF region.				
14. SUBJECT TERMS ICELAND-FÆROE FRONT, NOAA AVHRR, SST, ARGOS, DRIFTERS			15. NUMBER OF PAGES 150	
			16. PRICE CODE	
17. SECURITY CLASSIFICATION OF REPORT Unclassified	18. SECURITY CLASSIFICATION OF THIS PAGE Unclassified	18. SECURITY CLASSIFICATION OF ABSTRACT Unclassified	20. LIMITATION OF ABSTRACT UL	

Approved for public release; distribution is unlimited.

ICELAND-FÆROE FRONT STRUCTURE AND VARIABILITY

Christopher J. Arends
Lieutenant, United States Navy
B.S., Cornell University, 1990

Submitted in partial fulfillment of the
requirements for the degree of

MASTER OF SCIENCE IN METEOROLOGY AND
PHYSICAL OCEANOGRAPHY

from the

NAVAL POSTGRADUATE SCHOOL
June 1997

NPS ARCHIVE

1997.06

AREWDS, C.

~~10510~~
~~AL4/95~~
~~1.2~~

ABSTRACT

During the period June 1991 to August 1993, 107 Argos-tracked drifters, drogued to 15 m depth, were released in the Greenland, Iceland, and Norwegian (GIN) Seas. The drifter movements revealed the strong and spatially confined current systems along the Iceland-Færoe Front (IFF) and provided tracking of the Norwegian Atlantic Current and the general cyclonic gyre circulation in the GIN Sea.

Of the 107 drifters released, 59 were selected for this study due to their proximity to the IFF. Tracked by the Argos system aboard the NOAA polar orbiters, the drifters provided accurate location and sea surface temperature (SST) data. Interpolated and low-pass-filtered position data were used to construct maps of drifter displacement and surface velocity field estimates and to study the correlation between drifter trajectories and satellite derived SST frontal features.

Drifter SST data were compared to spatially and temporally coincident satellite retrieved SST data. The individual data sets were in good agreement with each other, resulting in a temperature difference of less than 1 °C.

Satellite imagery used to estimate surface currents through SST feature tracking provided a snapshot of the flow field over a short time scale.

The drifters revealed a distinct frontal zone (IFF) where the topographically steered flow field approached velocities of 1 m/s. This relatively strong flow became unstable as it propagated eastward and an intense eddy field developed. What began as a stable demarcation between water masses became a flow field dominated by warm and cold instabilities and intrusions. This dynamic transformation occurred over relatively short time (less than 5 days) and distance (several hundred kilometers) scales, testament to the vigorous activity in the IFF. These Lagrangian drifter measurements compose the first comprehensive, accurate near-surface velocity data set in the IFF region.

TABLE OF CONTENTS

I.	INTRODUCTION	1
II.	BACKGROUND	5
A.	THE GIN SEA	5
1.	Bathymetry and Geography	5
2.	Water Masses and Circulation	5
B.	THE GREENLAND-ICELAND-UNITED KINGDOM GAP	7
1.	Bathymetry	7
2.	Circulation	7
C.	THE ICELAND-FÆROE FRONT	10
1.	Water Mass Interaction	11
2.	Iceland-Færoe Ridge Influenced Flow	12
3.	Movement and Tracking	12
4.	Overflow	14
5.	Eddies	15
III.	DATA	29
A.	THERMAL SATELLITE IMAGERY	29
B.	SHIP MEASUREMENTS	36
C.	DRIFTER MEASUREMENTS	37
1.	Argos Tracking and Telemetry	39
2.	Drifter Deployments	40

3.	Data Distribution	41
4.	Data Editing	42
IV.	METHODS	57
A.	REGRESSION OF DRIFTER SST VS. SATELLITE SST	57
B.	SURFACE VELOCITY FIELD FROM DRIFTERS	58
C.	SST IMAGES AND DRIFTER DISPLACEMENTS	64
D.	SST FEATURE DISPLACEMENT AND ESTIMATED SURFACE VELOCITY FIELD	67
E.	SATELLITE SST IMAGES WITH COLOR CODED DRIFTER/ SHIP SST OVERLAYS	72
V.	RESULTS AND CONCLUSIONS.....	117
	APPENDIX. SST DATA	121
	LIST OF REFERENCES	129
	INITIAL DISTRIBUTION LIST	133

LIST OF FIGURES

1. Bathymetry and Major Features of the GIN Sea (from Hopkins, 1991).	19
2. Schematic T-S Diagram Showing the Different Water Masses of the GIN Sea (from Hopkins, 1991).	20
3. Schematic of Surface Circulation of the GIN Sea as Derived from Lagrangian Drifter Data. Thicker arrows represent the strong flows with speed in excess of 40 cm/s. The East Greenland Current is not depicted in this schematic map since it was not sampled by the drifters due to the ice coverage (from Poulain <i>et al.</i> , 1996a).	21
4. Iceland-F��roe Ridge Area Topography.	22
5. Circulation Across the Greenland-Iceland-United Kingdom Gap and in the GIN Sea. Red arrows represent relatively warm North Atlantic Water (NAW) and the blue arrows represent colder GIN Sea water (from ��sterhus, 1991).	23
6. Mean Temperature and Salinity Distributions Around Iceland During July (from Hopkins, 1991).	24
7. Temperature and Salinity Distribution over a Meridional Cross Section of the IFR (south is to the left). Hatched areas indicate North Atlantic Water (from Hopkins, 1991).	25
8. Mean Location of the IFF Over the IFR for Different Years (from Hansen and Meincke, 1979).	26
9. Schematic Representation of the Near-Surface and Bottom Circulation on the IFR According to Hansen and Meincke (1979). Arrows with numbers (cm/s) are based on measurements from moored instruments (Becker <i>et al.</i> , 1973; Koltermann <i>et al.</i> , 1976).	27
10. Infrared Transmittance of Several Gases in the Earth's Atmosphere and Combined Total Atmospheric Transmittance (from Kidder and Vonder Haar, 1995).	45
11. AVHRR Image of the GIN Sea Area from NOAA 11 Polar Orbiter, 1514 UTC 24 October 1992.	46
12. Photograph of a WOCE/TOGA Lagrangian Drifter Recovered after 8 months in the Norwegian Coastal Current (from Poulain <i>et al.</i> , 1996b).	47
13. Schematic Diagram of the WOCE/TOGA Lagrangian Drifter with Computation of Drag Area Ratio (from Poulain <i>et al.</i> , 1996a).	48

14. Individual Drifter Release Sites (Red Stars) Overlaid on Iceland-Færoe Ridge Bathymetry.	49
15. Number of Drifter Observations (Drifter-Days Per Day) in the GIN Sea as a Function of Time.	50
16. Same as Figure 15, but for IFR Region (60-70° N, 0-20° W). The days with the partially cloud-free satellite images considered in this study are also indicated.	51
17. Regression Analysis of Coincident Drifter and Satellite Retrieved SSTs from October 1992 to September 1992, which includes GIN92 and GIN93	77
18. Regression Analysis of Coincident Drifter and Satellite Retrieved SSTs for GIN92. ..	78
19. Drifter Trajectory Segments for August 1992. Star symbols indicate deployment sites or the drifter location at the beginning of the month. Circles are drawn at the location of last transmission (solid circle) or at the drifter location at the end of the month (open circle).	79
20. Same as Figure 19 for September 1992.	80
21. Same as Figure 19 for October 1992.	81
22. Same as Figure 19 for November 1992.	82
23. Same as Figure 19 for December 1992.	83
24. Same as Figure 19 for January 1993.	84
25. Same as Figure 19 for February 1993.	85
26. Same as Figure 19 for March 1993.	86
27. Same as Figure 19 for April 1993.	87
28. Same as Figure 19 for May 1993.	88
29. Same as Figure 19 for June 1993.	89
30. Same as Figure 19 for July 1993.	90
31. Same as Figure 19 for August 1993.	91

32. Same as Figure 19 for September 1993.	92
33. Same as Figure 19 for October 1993.	93
34. Same as Figure 19 for November 1993.	94
35. Same as Figure 19 for December 1993.	95
36. Composite "Spaghetti" Diagram Showing all the Drifter Tracks Between August 1992 and December 1993. The tracks are color-coded with respect to the deployment dates, i.e., blue (before GIN92), magenta (GIN92), green (between GIN92 and GIN93), and orange (GIN93). Dotted lines represent the tracks of un-drogued drifters.	96
37. MCSST Image of the IFR Region on 16 October 1992 at 1512 UTC. Light (dark) gray shades correspond to relatively cold (warm) sea surface temperatures. Cloud-covered pixels are shown in white. Superimposed drifter displacements begin the day before the image and end the day after. Star (circle) symbols denote the drifter location at the beginning (end) of the day.	97
38. Same as Figure 37 for 19 October 1992 at 1435 UTC.	98
39. Same as Figure 37 for 22 October 1992 at 1359 UTC.	99
40. Same as Figure 37 for 23 October 1992 at 1528 UTC.	100
41. Same as Figure 37 for 24 October 1992 at 0845 UTC.	101
42. Same as Figure 37 for 24 October 1992 at 1335 UTC.	102
43. Same as Figure 37 for 24 October 1992 at 1514 UTC.	103
44. Same as Figure 37 for 17 November 1992 at 1347 UTC.	104
45. Same as Figure 37 for 25 December 1992 at 1429 UTC.	105
46. Same as Figure 37 for 22 August 1993 at 1433 UTC.	106
47. Same as Figure 37 for 25 September 1993 at 1601 UTC.	107

48. MCSST Image of the IFF on 24 October 1992 at 0845 UTC with Overlay Showing Surface Velocity Vectors (Red Arrows) as Estimated by Manually Tracking the Major SST Features Between that Image and the Previous One (23 October 1992 at 1528 UTC). The cyan arrows are trajectories derived from the drifters.	108
49. Same as Figure 48 for Image Pair 24 October 1992 at 0845 UTC and 24 October 1992 at 1335 UTC.	109
50. Same as Figure 48 for Image Pair 24 October 1992 at 1335 UTC and 24 October 1992 at 1514 UTC. Velocity vectors estimated by two independent operators are depicted with blue and red arrows.	110
51. Close View of the IFF MCSST Field on 19 October 1992 at 1435 UTC. Cloud cover pixels are shown in black. Drifter and ship tracks for that day are overlaid on the satellite image and are color-coded with SST. The temperature scales for the satellite retrievals and the in-situ measurements are shown to the right of the image in units of degrees Celsius.	111
52. Same as Figure 51 for 22 October 1992 at 1359 UTC.	112
53. Same as Figure 51 for 23 October 1992 at 1528 UTC.	113
54. Same as Figure 51 for 24 October 1992 at 1514 UTC.	114

LIST OF TABLES

1. AVHRR Channels with Corresponding Wavelengths (Kidder and Vonder Haar, 1995).	52
2. NOAA Coefficients for Global SST Retrieval Algorithms (from Essen <i>et al.</i> , 1996).	53
3. Error Budget for AVHRR Measurements (from Minnett, 1991).	54
4. Individual High Quality in situ Instruments Listed from Most Accurate to Least Accurate (from Minnett, 1991).	55
5. Spatial and Temporal Variability Errors Between AVHRR and in situ SST Measurements (from Minnett, 1991).	56
6. Infrared Satellite Images used from October 1992 to September 1993.....	115
7. Results of SST Feature Tracking in the IFF.	116

ACKNOWLEDGMENT

Foremost, I would like to thank Dr. Pierre-Marie Poulain. This thesis would not have been possible without his insight, involvement, and knowledge. For their assistance on numerous MATLAB programs, I am indebted to Brian Brown, Mike Cook, and Craig Norheim.

The NATO SACLANT Undersea Research Centre La Spezia, Italy is acknowledged for making the satellite and drifter data available; specifically, I would like to thank Elvio Nacini for processing the raw satellite images.

I. INTRODUCTION

The area north of a line drawn from Greenland to Iceland and then to the United Kingdom (GIUK Gap) is known as the GIN Sea, which is the collective waters of the Greenland, Iceland and Norwegian Seas and together with the Polar Sea constitutes the Arctic Ocean (Hopkins, 1991). The relatively cold and fresh waters of the GIN Sea interact with the warmer and saltier waters of the North Atlantic. A dynamic boundary between these water masses exists from the east coast of Iceland to an area north of the Færoe Islands and is called the Iceland-Færoe Front (IFF). The bathymetry of the region plays a vital role in the dynamics of its circulation. In addition, the geographic setting and the bathymetric connections with other oceanic regions act to determine the thermohaline characteristics of the waters in this region.

Lagrangian drifters were deployed as part of the NATO SACLANT GIN Sea Project which sought to develop an understanding of the complex physical processes causing synoptic and mesoscale frontal variability (GSP Group, 1990). The characteristics and variability of near surface ocean currents and temperature distribution are crucial in support of Anti-Submarine Warfare (ASW) and Mine Counter-Measures (MCM) operations.

Strategically, the GIUK Gap is an area of high submarine traffic even in the late 1990's. The few entry points in the GIUK Gap become choke points for submarines entering and exiting the area. The water mass interactions across the frontal boundaries along the GIUK Gap are complicated and significantly affect the temperature and sound speed profile on a large range of scales, creating a complex operating environment.

Sonar capability and prediction requires accurate and timely analysis of ocean dynamics and the associated spatial and temporal variability. Ocean dynamics, through the resultant current structures, determine the temperature, salinity, and sound speed distributions. Regions of high mesoscale variability like the IFF require frequent (real-time) data collection to constantly update the sound speed information (Peggion, 1993). Better understanding of this dynamic region and its affects on acoustics will provide a tactical advantage.

Oceanographically, the GIUK Gap is one of the world's most important boundaries by allowing a strong two-way advective exchange between the ice-covered Polar Sea and the North Atlantic Ocean. The GIN Sea is the primary site for Northern Hemisphere bottom water formation which occurs through active convection driven by large cyclonic gyres (Hopkins, 1991). North Atlantic Bottom Water (NABW) exits the GIN Sea primarily through the Denmark Strait, sinks to a level of equal density, and spreads south along its characteristic isopycnals. Relatively warm Atlantic Water originating from the North Atlantic Drift, crosses the GIUK Gap in two main locations: the Iceland-Færoe Ridge (IFR) and the Færoe-Shetland Channel. These conduits of Atlantic Water are gateways to the Polar Sea, as the Norwegian Atlantic Current moves the water rapidly northward toward Fram Strait and into the Barents Sea.

Satellite-tracked drifters, drogued in the surface mixed layer (15 m nominal depth), were released in the IFF and GIN Sea by the NATO SACLANT Undersea Research Centre La Spezia, Italy, in order to study the spatial and temporal variability of the surface currents and surface temperature over about 3 years. The majority of drifters were deployed east of

Iceland from NRV *Alliance* during hydrographic surveys, providing unique measurements of current and temperature in the complex IFF. After deployment and data recovery in the IFF, the drifters were dispersed by prevailing currents to sample most of the ice-free GIN Sea. Surface drifters indicated the presence of topographically-controlled flow patterns over the shallow features of the Iceland-Færoe Ridge and significant mesoscale structures having time scales of several days and space scales of several tens of kilometers in the IFF (Poulain *et al.*, 1996a)

The drifters provided the first basin scale, accurate, near surface data set from which many important circulation characteristics were discovered, quantified and interpreted. The location data were used to construct surface velocity field estimates and drifter displacement diagrams. The results of the drifter experiment demonstrate that drifter measurements can be a practical and cost effective alternative to the extensive use of moored current meters. Oceanographic information is obtained from satellite-tracked drifters remotely, without costly and prolonged residence time for on-site research vessels and platforms.

In this thesis several approaches are used to describe the surface spatial characteristics (temperature and currents) and temporal evolution of the IFF, using 59 drifters (11,605 drifter days) and 11 AVHRR satellite images. Data and images are manipulated independently, and in conjunction with each other, maximizing their descriptive potential for analysis of physical processes.

Drifter SST measurements are used to validate satellite remotely sensed SST data, schematically with figure overlays, and numerically through a regression analysis. Surface drifter location data provides detailed analysis of the flow field with schematic diagrams

depicting trajectories of individual drifters. These diagrams are modified spatially and temporally to provide the best possible analysis of mesoscale activity in the IFF. SST features revealed by satellite imagery and augmented by drifter trajectory overlays are the most comprehensive and accurate ways of describing the flow field. Further estimates of surface velocities are achieved by tracking SST features through sequential satellite images.

This thesis is organized as follows. In section 2, the bathymetry, water masses, and circulation of the GIN Sea area are reviewed leading into a discussion about surface currents in and around the Greenland-Iceland-United Kingdom (GIUK) Gap. Attention is focused on the intricacies of the IFF, examining water mass interactions, IFR-influenced flows, IFF movement and tracking, overflow of GIN Sea water over the IFR, and the formation of eddies and instabilities. In section 3, subsection A details the extraction of sea surface temperatures (SST) from satellites and provides information concerning the latest algorithms and expected accuracies achieved by spaceborne radiometers. Subsection B discusses drifter measurements and deployments as well as Argos tracking and telemetry followed by the data distribution and editing process. In section 4, the methods of data extraction, analysis, and display are examined, encompassing the research core of this thesis. Specifically, subsections A and E compare surface measurements with remotely sensed data, while subsections B-D investigate the surface velocity field of the IFF. Finally, section 5 contemplates the most notable discoveries and conclusions derived from our interpretation of the data set. All figures mentioned in the text are grouped following their respective chapters.

II. BACKGROUND

A. THE GIN SEA

1. Bathymetry and Geography

The Arctic Ocean consists of the Greenland, Iceland, and Norwegian (GIN) Seas together with the Polar Sea (Hopkins, 1991). The GIN Sea has six open boundaries through which important exchanges occur. Two boundaries are on the northern flank of the GIN Sea and they exchange with the Barents Sea and the Polar Sea (Fram Strait). The remaining four boundaries exchange with the Atlantic Ocean over a ridge connecting Greenland, via Iceland and the Færoe Islands Plateau, to the north European continental shelf. There are three major gaps in this ridge, the Denmark Strait, the Iceland-Færoe Ridge (IFR) and the Færoe-Shetland Channel. These gaps and other major features are displayed in Figure 1.

The Denmark Strait is the primary exit of Polar Water into the Atlantic Ocean whereas the Færoe-Shetland Channel is the primary entrance for North Atlantic Water into the GIN Sea and eventually the Polar Sea.

2. Water Masses and Circulation

The following discussion is derived from a detailed analysis of the water masses in the GIN Sea and Polar Sea by Hopkins (1991).

The water masses found in the GIN Sea arise from two parent water masses: the Polar Water (PW) from the Polar Sea, which is relatively cold and of low salinity, and the North Atlantic Water (NAW) from the North Atlantic, which is relatively warm and of high salinity.

The intermediate and deep waters of the GIN Sea (and the rest of the Arctic Ocean) are more dense than those at equivalent depths in the Atlantic, classifying the basin as having a negative thermohaline circulation. Dense waters are formed within the basin at the surface, sink, and feed a dense water output over the sill, which is compensated by inflow of surface NAW. Thus the forcing for this type of circulation is the buoyancy extraction occurring at the surface through losses in heat and/or water.

The basic division in the GIN Sea between water masses occurs longitudinally in salinity, and meridionally in temperature. The result is a water mass of considerable spiciness (hot and salty) (Veronis, 1972) in the southeastern portion of the GIN Sea decreasing diagonally northwest to a colder, fresher water mass structure around the region of Fram Strait discharge.

The waters of each of the three major seas of the GIN Sea occupy different but overlapping regions in T-S space. This is shown schematically in Figure 2 where the Iceland Sea evolves out of the Atlantic Water via the Norwegian and Greenland Seas in that sequence. Because of the geographic variation, the choice of a single density value will not always serve to divide water masses and thus a range of values is preferred. (Hopkins, 1991)

Drifter movements in the GIN Sea revealed strong and spatially confined current systems along the surface salinity fronts of the Iceland-Færoe Frontal zone which divides the GIN Sea from the North Atlantic, the Norwegian coast, and along the continental margins and their extensions to the Barents Sea and Spitsbergen. The Norwegian Atlantic Current is composed of three distinct streams (one coastal and two continental margin branches) which join into one single swift mean current west of the Lofoten and Vesterålen Islands

(~69° N 15° E), where the strongest measured currents are in excess of 110 cm/s. The surface circulation of the ice-free GIN Sea, as derived from drifter data (Poulain *et al.*, 1996a), is shown schematically in Figure 3. In addition to the general cyclonic gyre circulation in the GIN Sea, the drifters indicate smaller cyclonic circulation patterns in all major sub-basins, i.e., the Iceland Plateau, the Norwegian, the Lofoten, and the Greenland Basins.

B. THE GREENLAND-ICELAND-UNITED KINGDOM GAP

1. Bathymetry

Of the southern openings to the North Atlantic, the IFR is the widest, extending about 400 km from Iceland to the Færoe Islands. It is also the shallowest, with a maximum sill depth of 480 m, but it is not so shallow as to necessarily restrict any southern movement of the deeper GIN Sea water masses (Hopkins, 1991). Detailed bathymetry of the area can be seen in Figure 4. The IFR is the blue plateau that extends into the figure where it intersects the depicted crimson peaks of Iceland.

2. Circulation

The following describes what is schematically shown in Figure 5. North Atlantic Water (NAW) breeches the IFR and flows eastward where it joins the largest inflow of NAW passing through the Færoe-Shetland channel into the GIN Sea. The combined flows proceed northward toward the Polar Sea. The Denmark Strait between Greenland and Iceland serves as a conduit for modified Arctic Water to exit the GIN Sea region. Even though this strait serves as the principal outflow of the area, a smaller volume of NAW flows northward through the strait and turns eastward along the northern shores of Iceland becoming the North Icelandic Irminger Current (NIIC). The NIIC originates from the northward flowing Irminger

Current which bifurcates southwest of Iceland in the vicinity of the Reykjanes Ridge. The western branch supplies the NIIC with 9.6 Sv flow into the Irminger Basin (Krauss, 1995).

Between the opposing northern and southern flows across the GIUK gap is the Icelandic Current (IC), which is a zonal current system considered to be the final link in the cyclonic boundary system of currents that exist in the GIN Sea. The westward origin of this current is the NIIC. The IC flows eastward along the northern continental slope of Iceland where it is exposed to two distinct water masses. The northern extent of the current encounters water of the central Iceland Sea which has been modified by mixing with a branch of the very cold and fresh East Greenland Current (EGC) (Perkins *et al.*, 1997). The southern border of the current mixes with Icelandic coastal waters which have been freshened by local runoff. During summer, downward mixing on the shelf is suppressed by insolation and the summer influx of fresh water. The difference in water masses affects the across-shelf slope of the steric level, creating a summer speed maximum in the NIIC (Perkins *et al.*, 1996).

Once the current leaves the coast of Iceland, it continues eastward rather than southward and is no longer considered a coastal boundary current although it remains bathymetrically steered eastward along the north flank of the IFR (Hopkins, 1991).

Current measurements along the southeastern Icelandic continental shelf, south of the IFR, have shown a flow to the southwest, giving the appearance of continuous anticyclonic circulation around Iceland. However, the waters to the southeast are of Atlantic origin and are not a continuation of the IC waters. There is, therefore, a water mass boundary over the

eastern Icelandic shelf corresponding to the eastward turning of the IC. This situation is well illustrated by the circum-Icelandic contours of summer temperature and salinity in Figure 6.

The IC is joined at the IFR from the south by the eastern branch of the Irminger Current which is considerably different in temperature and salinity from its modified western branch. After crossing 62°N , the eastern branch of the Irminger Current transports 8.1 Sv toward the IFR. Of this, 3.0 Sv flow southwest of the F  roe Islands along the bottom contours toward the F  roe-Shetland Channel and continue toward the Norwegian Sea. An estimated 4.6 Sv cross the IFR and flow along it until entering the Norwegian Sea directly northeast of the F  roe Islands. (Krauss, 1995)

In conclusion, once the Atlantic Water fully circumnavigates Iceland and returns to where it began, the water has been completely modified and is now a different water mass which is cooler, fresher, and denser. Thus, the water mass difference across the IFR is partially a direct result of this modification of the IC from freshening along the northern coast of Iceland contrasted with the unmodified NAW to the south.

Even though Krauss (1995) submits volume transport calculations for the Irminger current, the author also states several reasons why these computations are ambiguous for the northern North Atlantic:

1. Eddies dominate the stratification. According to their dependency on the Rossby radius (Krauss *et al.*, 1990), the typical scale is of order less than 100 km. Typical moored buoy station spacing (~ 40 km) or ship observations, the source of Krauss' volume transport estimates, cannot resolve the details of an eddy field of this small size.

2. Many currents in the north are either frontal jets between coastal waters and Atlantic Water or deep currents at the continental slope. Both types of currents reach their maximum in areas with large variations in bottom topography. The extrapolation of dynamic anomalies at the continental slope or the Mid-Atlantic Ridge is to some extent arbitrary.

3. The application of the thermal wind equation in the computation of overflow currents is questionable. Downslope acceleration may increase the speed of these currents, yielding values much higher than those deduced from geostrophic and hydrostatic balances.

C. THE ICELAND-FÆROE FRONT

The importance of the IFR relative to the exchange of waters between the GIN Sea and the North Atlantic Ocean is greatly reduced by a segment of the Arctic Front, called the Iceland Færoe Front (IFF) (Hopkins, 1991). The IFF is defined as the northern boundary of North Atlantic Water which overlies the IFR and is orientated generally parallel to the ridge. Although closely related to bathymetry, the IFF is prone to meandering and its position, while seasonally dependent, can vary up to 200 km on a time scale of several months (Allen *et al.*, 1994).

Described as a demarcation between relatively warm, salty Atlantic water to the south and colder, fresher Arctic and Subarctic water to the north, the IFF is a complex boundary between seven different water masses of Atlantic, Norwegian Sea and Arctic origin. Understanding the detailed mixing processes and water mass transport of this region is made difficult by the strong influence of topography and the complex tides, which at times dominate the velocity field. (Allen *et al.*, 1994)

1. Water Mass Interaction

There is considerable modification of water masses from west to east along the IFF, and before turning north of the Færoe Islands, the IFF becomes more convoluted and ill-defined. At its eastern end, the IFF becomes a more complicated boundary between several water masses (Hansen and Meincke, 1979). The slope of the IFF is also a function of distance from the Icelandic shelf. Near Iceland, the IFF is nearly vertical from the IFR to the surface, then becomes very oblique north of the Færoe Islands with NAW overflowing modified Arctic water.

According to Hallock (1985), thermohaline features are highly variable, particularly in the upper 200 m. Interleaving of cold, Arctic water and warmer, Atlantic water occurs on vertical scales of the order of 50 m, consistent with those predicted by Ruddick and Turner (1979) for intrusions driven by double-diffusive convection. Calculations of heat flux ($5.16 \times 10^4 \text{ W m}^{-2}$) and salt flux ($1.58 \text{ kg} \times 10^{-3} \text{ m}^{-2} \text{ s}^{-1}$) across the front show larger values of the same order as eddy heat fluxes across the IFR found by Willebrand and Meincke (1980).

On the south side of the IFF, the fairly homogeneous North Atlantic Water is found to depths much greater than those on the ridge itself. On the north side, the Icelandic Current occupies the upper 500 m of the water column. In cross section, conducted in June 1977, the water mass interface is well defined by strong gradients (Figure 7). Temperatures decrease from 7 °C to 0 °C and salinity shows a decrease from 35.15 psu to 34.8 psu (Hopkins, 1991).

At its western limit, the IFF extends onto the Iceland shelf where it divides the shelf circulation into two regimes: northward flowing Atlantic Water and southward flowing Icelandic Current Water. The northward confluence of the lighter North Atlantic Water, over

the southeastern Icelandic shelf and over the southern portion of the IFR, forms a sea-level high pressure ridge that extends eastward from Iceland and coincides with the IFR. Thus, the along shelf (north-south) density difference between the Polar Water and the Atlantic Water along the IFR is sufficient to re-orient the offshore geostrophic flow eastward reaching mean speeds of 25 cm/s (Perkins *et al.*, 1996).

2. Iceland-Færoe Ridge-Influenced Flow

The same pressure gradient forces exist across the IFR as those that force the flow through the Færoe Channel, but with a bathymetric difference. This configuration allows a countercurrent, geostrophically adjusted to the pressure changes across the front, to flow parallel to the sill instead of transverse to it. The dynamic height difference across the front, referenced to 300 m, is about 15 cm, and the corresponding transport of NAW is estimated at 3.5 Sv, based on data from moored current meters (Perkins *et al.*, 1997). The actual alignment of the front is oblique to the bathymetry resulting in a situation not quite symmetric east and west, that is, very little outflow occurs east of Iceland whereas considerable inflow does occur west of the Færoe Islands (Hopkins, 1991).

3. Movement and Tracking

The surface manifestation of the IFF is highly variable in space and time. IFF position is defined as the region of maximum horizontal temperature gradient. The best agreement between frontal locations and bottom topography occurs when the deepest frontal zone locations are compared to the shallowest depth regimes (Smart, 1984). In addition to the mid-gradient isotherm, the location is often identified by the 35 psu isohaline. Figure 8 shows five spring positions between 1952 and 1957 for the 35 psu isohaline and an envelope

of the mid gradient isotherms (dotted lines) from five surveys between July 1971 and October 1972. The definition of the IFF diminishes to the east where isotherms become spread apart, particularly during summer, due to surface heating and the mixing associated with large lateral excursions.

Upon further examination of Figure 8, a large northward meandering of the IFF (usually north of 65° N) is evident just east of the Icelandic shelf break. This tongue of NAW protruding into the GIN Sea is spatially variable yet temporally consistent. The northernmost area of this intrusion has been referred to as "Red Square" due to the massive fishing operations conducted there by Russian fishing vessels.

Surface maps of temperature and salinity indicate that the lateral oscillations in the front have periodicities on the order of days rather than months. This finding is substantiated by moored time series records having a dominant time scale over the IFR of 10 days (Willebrand and Meincke, 1980) due to frontal baroclinic instabilities. Movement of the front perpendicular to the IFR is not equivalent to cross frontal exchange, although severe protrusions are the most common situation in which significant exchange occurs. Erosion of the frontal boundary occurs within the surface frictional layer, resulting in a more diffuse water mass boundary. The surface waters in the frontal area are characterized by lower vertical stabilities. Surface frontal mixing plays an important part in the generation of the modified Atlantic Water mass which, being created along the front, is advected southeastward until its confluence with the Norwegian Atlantic Water. (Hopkins, 1991)

The IFF intersects the coast of Iceland at a point varying seasonally from $64^{\circ} 25'$ to $64^{\circ} 10'$, approximately 50 km in a southeastward direction. In summer, the coldest water on

the shelf is found in a pool near the coast just north of the front and streams offshore as a near surface filament along the IFF between NAW and the surface waters normally found north of the front. Deeper portions of this cool feature consist of water entrained at depth rather than subducted from the surface. (Perkins *et al.*, 1997)

4. Overflow

The primary mechanism for overflow is considered to be the mixing processes which occur in the frictional bottom layer. Figure 9 shows a schematic representation of the flow over the IFR for the surface (c) and bottom layers (d). According to Hansen and Meincke (1979), flow on the surface over the north and south flanks follows the general bathymetry, to the southeast and to the northwest, respectively. The flow over the crest (bottom) tends to be to the south over the western portion and to the north over the eastern portion. Maxima in flow, shear, and temperature gradient all occurred within 50 m above the bottom suggesting that the bottom layer may act as a conduit by which a mixed water mass is transported southward. Mixing over the crest zone is also enhanced by the horizontal shear generated by the oppositely directed flows (Hopkins, 1991).

Water from the GIN Sea overflows the IFR at several locations, but the volume, speed and steadiness of this overflow are greater than expected. Current intensity is attributed to local bottom steepness. Its steadiness is surprising, considering the factors that might contribute to its variability, such as formation of eddies along the IFF, passage of intense storms, or modulation by the spring-neap tidal schedule. (Perkins *et al.*, 1996)

The overflow of cold water from the Norwegian Sea across the IFR and through the Færoe Bank Channel is well documented: 1.5-1.9 Sv flows through the Færoe Bank Channel

(Borenas and Lundberg, 1988; Saunders, 1990), and an additional 1 Sv results from occasional overflows across the IFR. The total transport of bottom water is assumed to increase to about 5 Sv south of Iceland owing to entrainment of Atlantic Water (Steele *et al.*, 1962).

5. Eddies

Acting as a free inertial jet, IFF develops into an intense eddy field farther to the east. The surface expression of the front, to a depth of about 100 m, is convoluted by eddy-like features probably along its entire length. The front is a wide (70 km) swath populated by many folds and segments of more intense frontal gradients. The subsurface front, from about 100 m to the depth of the IFR, is a better defined feature and appears to be less convoluted than the surface signature. It slopes significantly from the vertical (southward from the northern edge) and shows strong evidence of intrusive interleaving that may well be driven by double-diffusive convection. While transports of properties across the front by intrusive mixing alone appear insignificant in comparison to overall balances of the Norwegian Sea, they are locally important and are of the same order as eddy transports. The latter are evidenced by the presence of anomalous globs found on both sides of the front. (Hallock, 1985)

When the IFF meanders or sheds eddies into a southwesterly direction, polar water masses close to the bottom flow over the Atlantic slope of the ridge. Once the dense waters merge with the less dense Atlantic waters, they flow downslope under the influence of gravity, Coriolis force, and friction. Therefore, eddies and meanders of the IFF provide a mechanism to increase intermittently the overflow of GIN Sea waters, which are normally

restricted to the narrow notches of the crest zone and to the continental slope east of Iceland. Specifically, cyclonic eddies transport Arctic water southward across North Atlantic Water, and anticyclonic eddies transport North Atlantic Water across the front into Arctic water. (Hansen and Meincke, 1979)

Eddies in the IFF are derived from baroclinic instability (Allen *et al.*, 1994) (releasing energy from mean vertical shear) causing wave perturbations to grow unstable when traveling within a sheared flow over a sloping bottom and then interacting with the evolving current field. These waves have the net effect of draining energy from the vertical shear flow at mid-depth and transferring it to kinetic energy closer to the surface. According to numerical simulations of IFF flow over a smooth ridge (Miller *et al.*, 1995a, b), topography does not strongly influence the developing meanders since the instability process is most active in the middle and upper levels of the water column. However, other models using a high resolution bathymetry (Maskell *et al.*, 1992) show that the effect of ridge topography is important for instability development. Bottom trapping and magnification of instabilities or suppression of their surface signatures depends on how the front interacts with the ridge.

In terms of barotropic and mixed eddies, Hansen and Meincke (1979) concluded that in the case of the IFR, the tendency of the mean bottom currents to follow the isobaths can cause the formation of eddies. A number of prominent features with horizontal scales of order 50 km and with an elevation of up to 100 m characterizes the actual topography of the crest zone. In this case, eddy-like structures should emanate from the near bottom layer into the interior and they should mostly be observed to be connected to a topographic feature.

A second possibility for the generation of eddy-like features is the large change in potential vorticity across the front on the isopycnal layers on which eddies are observed. This was made evident by a large change in layer thickness between two specific isopycnals and supports the notion that eddies are the consequence of baroclinic instability (Allen *et al.*, 1994). Cold core cyclonic eddies have shown thickness decreases along isopycnal surfaces, indicative of an anomaly of high potential vorticity and cyclonic circulation. Large changes in potential vorticity create a barrier across which it is difficult for mixing to take place; however, transport across the front can occur when eddies break off due to unstable meanders of the front (Miller *et al.*, 1995a, b). The IFF is also a zone with a large amount of available potential energy in the mean state, which can be converted into kinetic and potential energy perturbations (Hansen and Meincke, 1979).

Stirring by eddies and subsequent vertical mixing by salt fingering and double diffusive layering contributes to the reduction of horizontal and vertical gradients in temperature and salinity (Krauss, 1995). This gradient reduction is evident on the ill-defined eastern portion of the IFF near the Færoe Islands.

Interpretation of the survey conducted by Gould *et al.* (1987) shows 7 cold eddies south of the IFF; Niiler *et al.* (1992) and Scott and Lane (1990) located 10 cold eddies of 30-50 km size diameter and only 1 warm eddy north of the IFF. Allen *et al.* (1994) found a number of cold-core cyclonic eddies of 15-30 km diameter and a few warm anticyclonic features. For the interpretation of the data statistics, Niiler *et al.* (1992) suggest that the dynamical situation for cold eddy formation is analogous to that of the Gulf Stream (Robinson *et al.*, 1996).

The average salt transport per eddy is $\sim 4.5 \times 10^{10}$ kg (Allen *et al.*, 1994), and therefore an order of magnitude calculation for the salt flux due to eddy activity across the IFF, assuming an average depth of 500 m, gives a value of $\sim 3.5 \times 10^{-3}$ kg m⁻² s⁻¹. The average eddy heat transport is 1.12×10^{18} J per eddy and an estimated heat flux due to eddy activity is 8.0×10^4 W m⁻² (Allen *et al.*, 1994). The calculations of the salt and heat fluxes are dependent upon the reliable estimate for the rate of generation of eddies at the front, and thus the wavelength and period of unstable meanders. From observations made by Allen *et al.* (1994), the estimated wavelength of the frontal meanders was 60 km. This is comparable with the predictions from linear models of the wavelength of baroclinic instabilities.

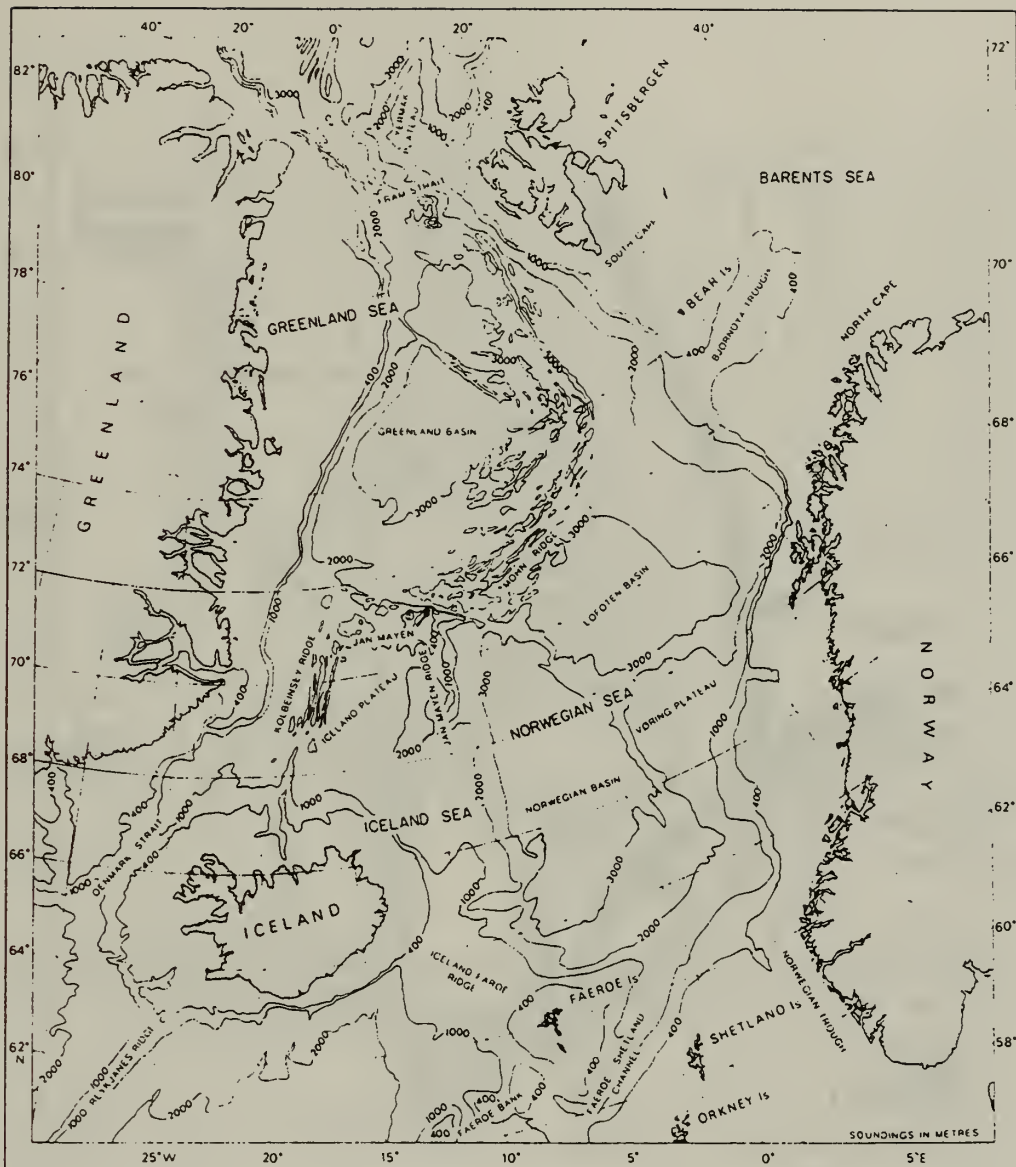


Figure 1. Bathymetry and Major Features of the Gin Sea (from Hopkins, 1991).

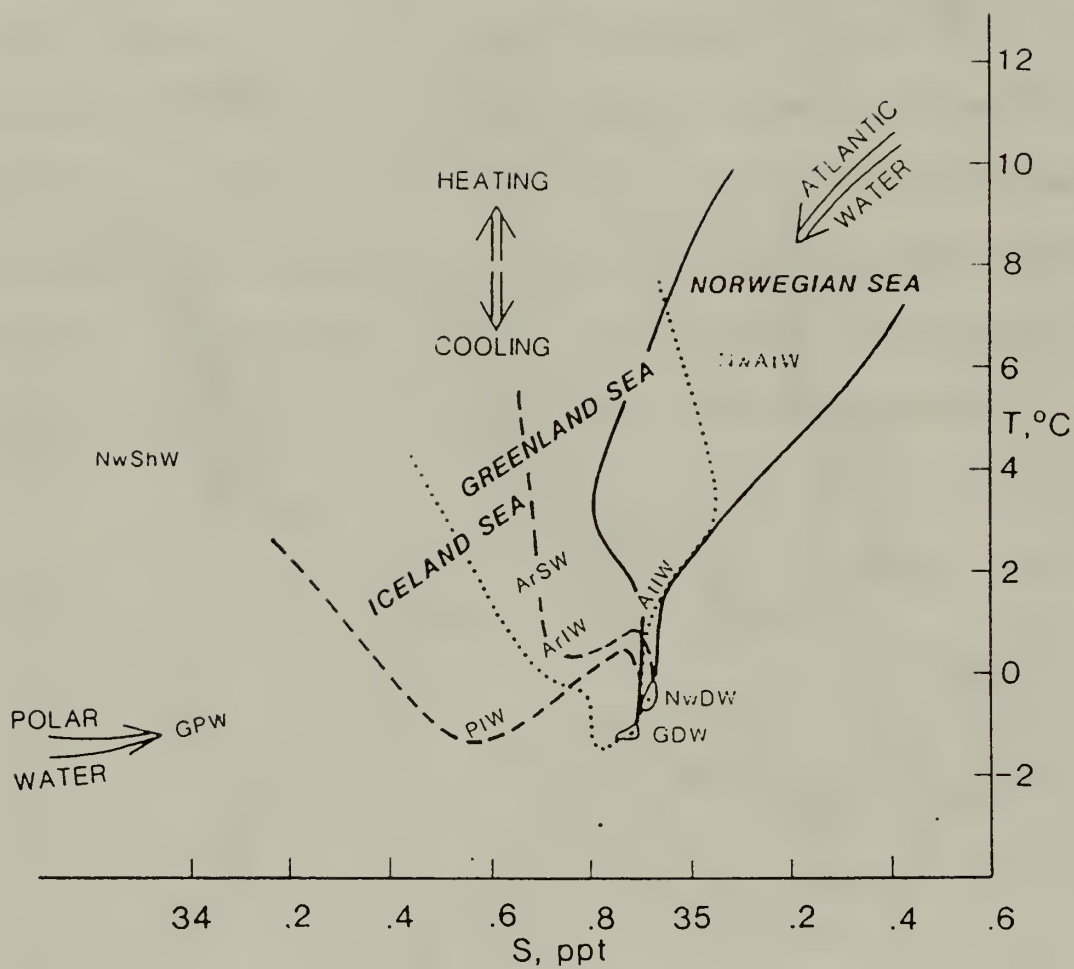


Figure 2. Schematic T-S Diagram Showing the Different Water Masses of the GIN Sea (from Hopkins, 1991).



Figure 3. Schematic of Surface Circulation of the GIN Sea as Derived from Lagrangian Drifter Data. Thicker arrows represent the strong flows with speed in excess of 40 cm/s. The East Greenland Current is not depicted in this schematic map since it was not sampled by the drifters due to the ice coverage (from Poulain *et al.*, 1996a).

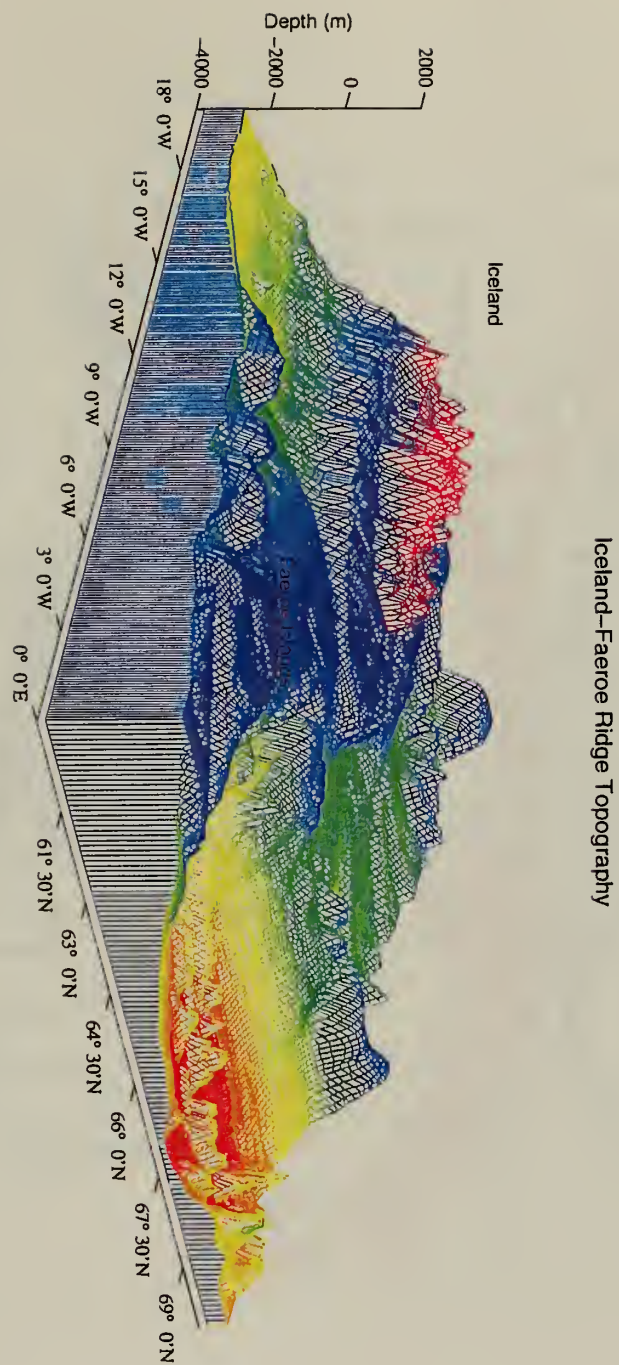


Figure 4. Iceland-Faeroe Ridge Area Topography.

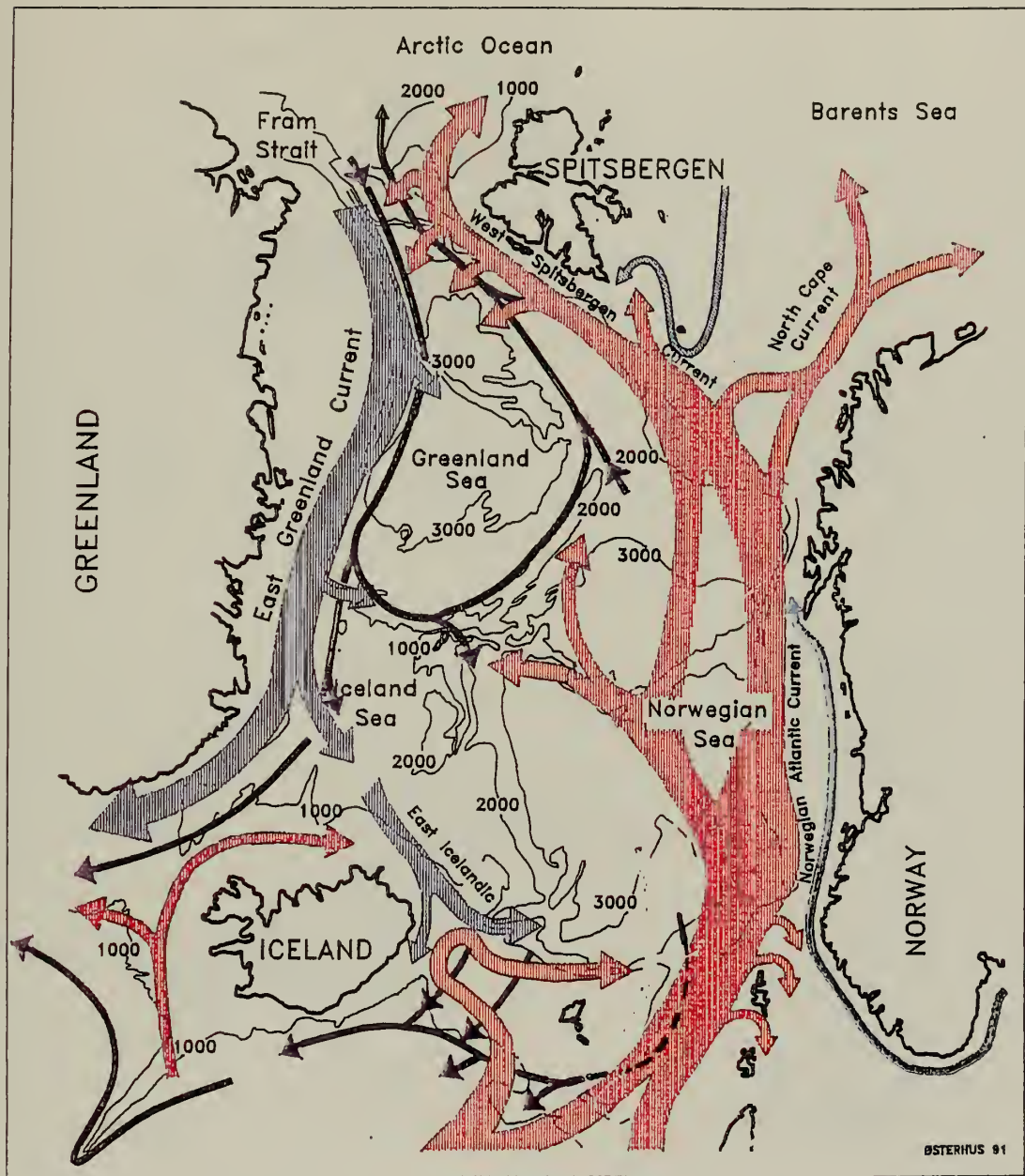


Figure 5. Circulation across the Greenland-Iceland-United Kingdom gap and in the GIN Sea (from Østerhus, 1991). Red arrows represent relatively warm North Atlantic Water (NAW) and the blue arrows represent colder GIN Sea water (from Østerhus, 1991).

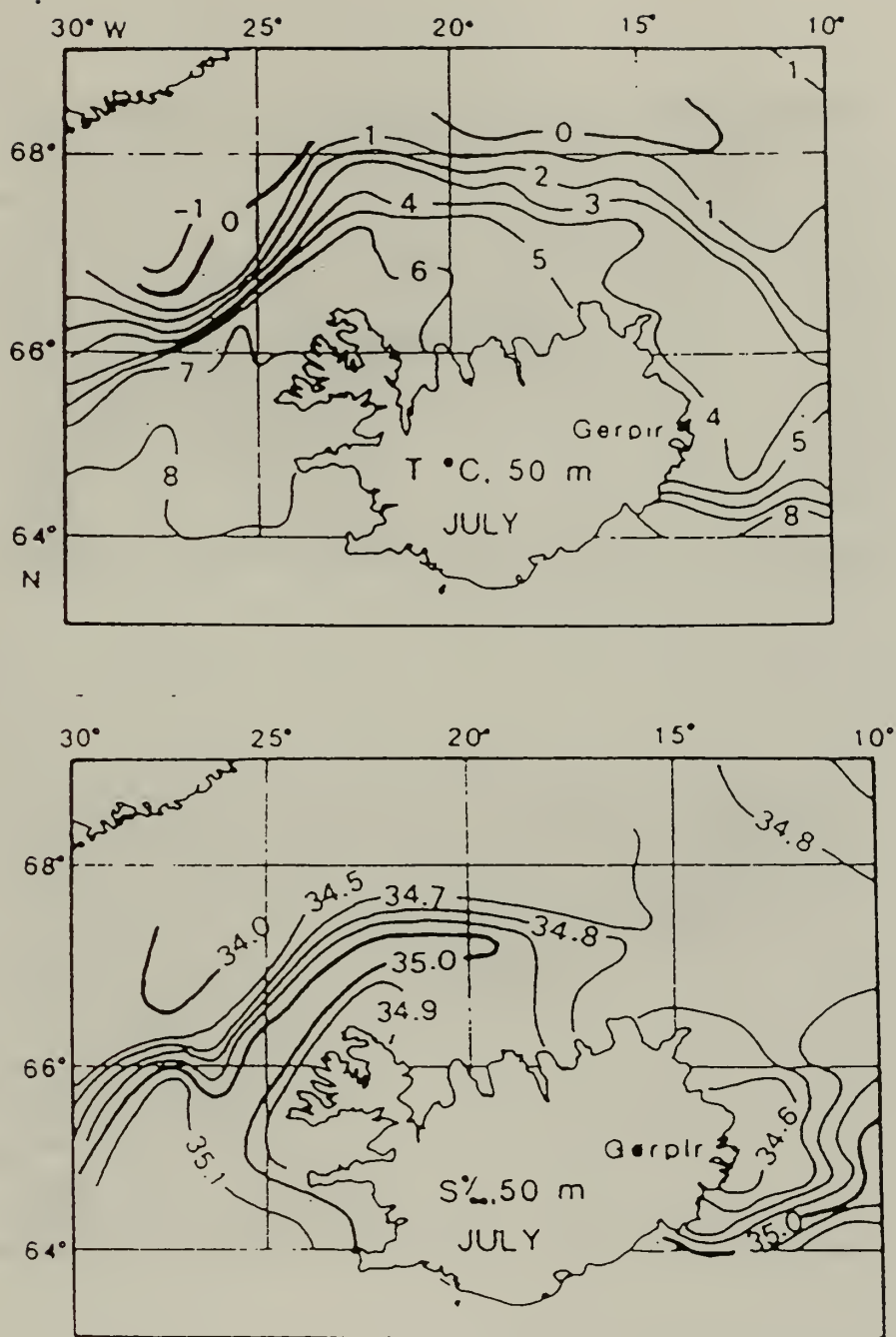


Figure 6. Mean Temperature and Salinity Distributions Around Iceland During July (from Hopkins, 1991).

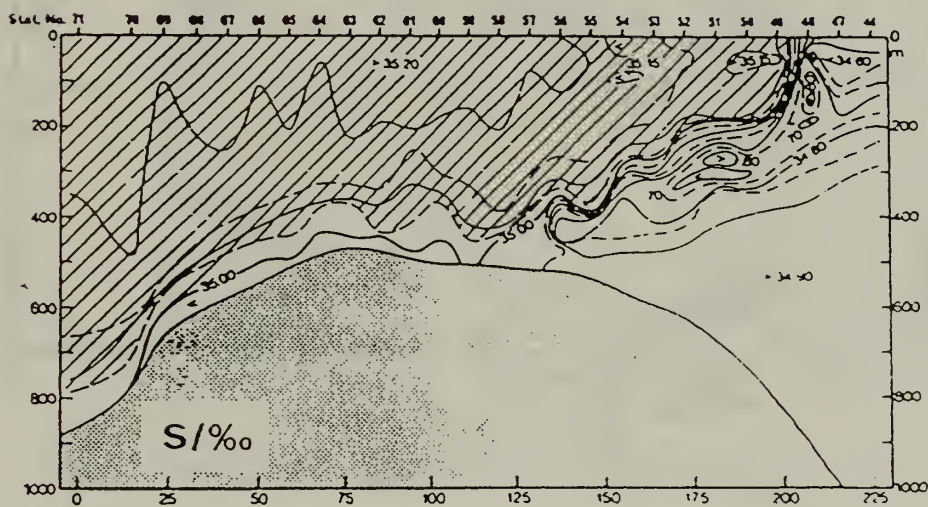
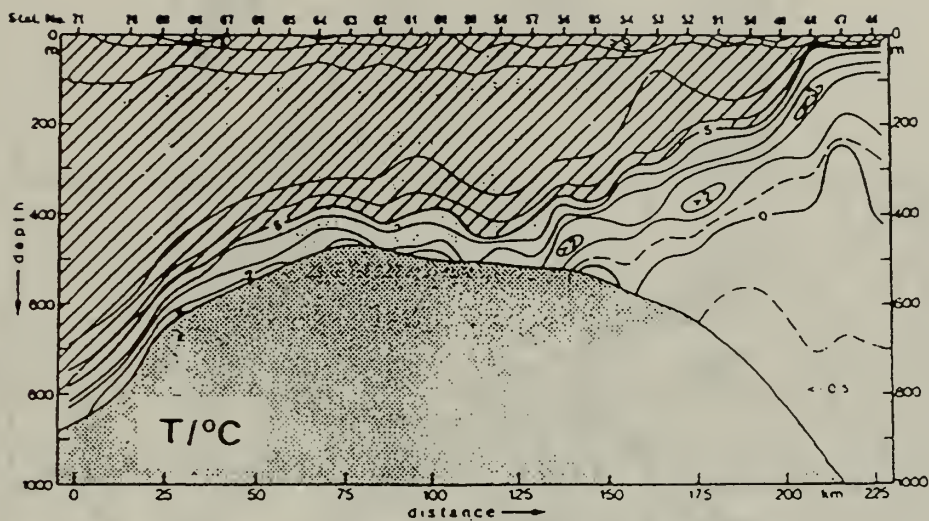


Figure 7. Temperature and Salinity Distribution over a Meridional Cross Section of the IFR (south is to the left). Hatched areas indicate North Atlantic Water (from Hopkins, 1991).

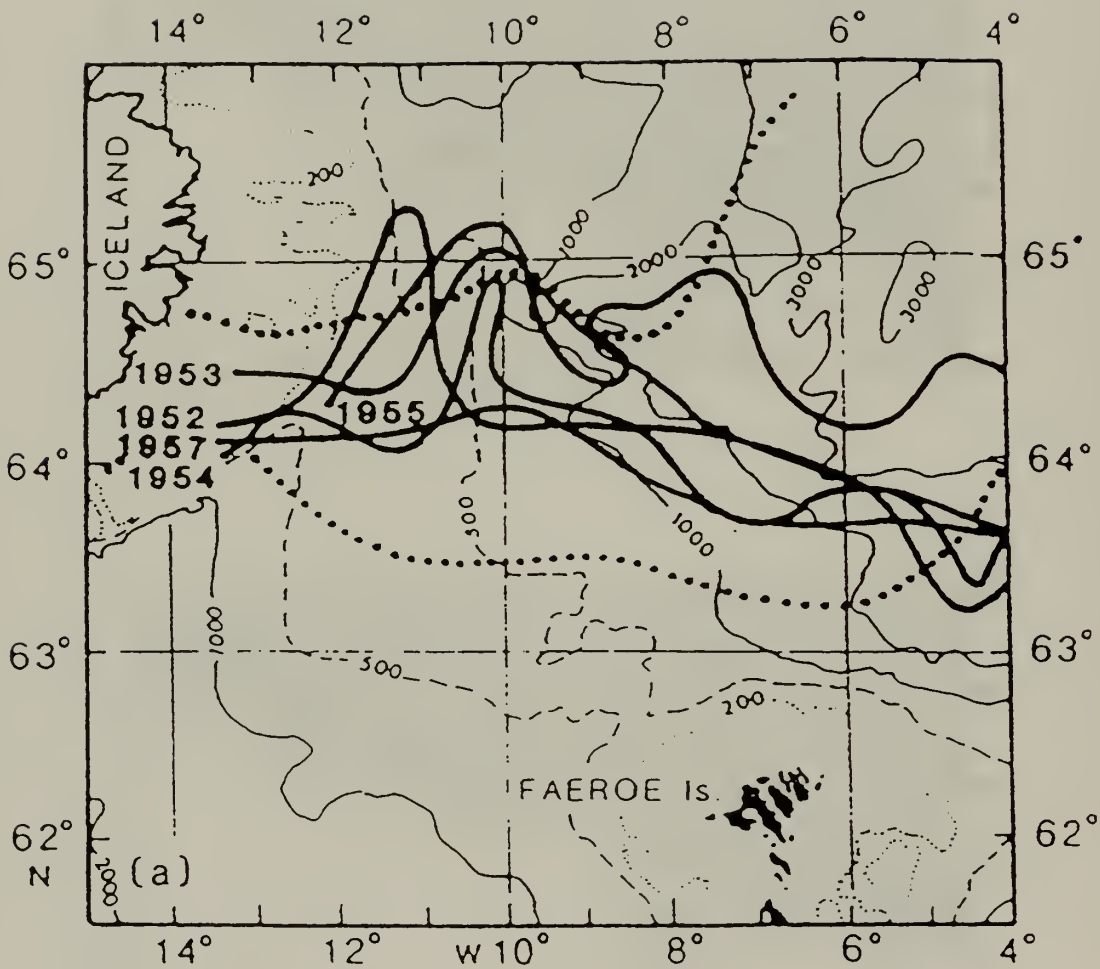


Figure 8. Mean Location of the IFF over the IFR for Different Years (from Hansen and Meincke, 1979).

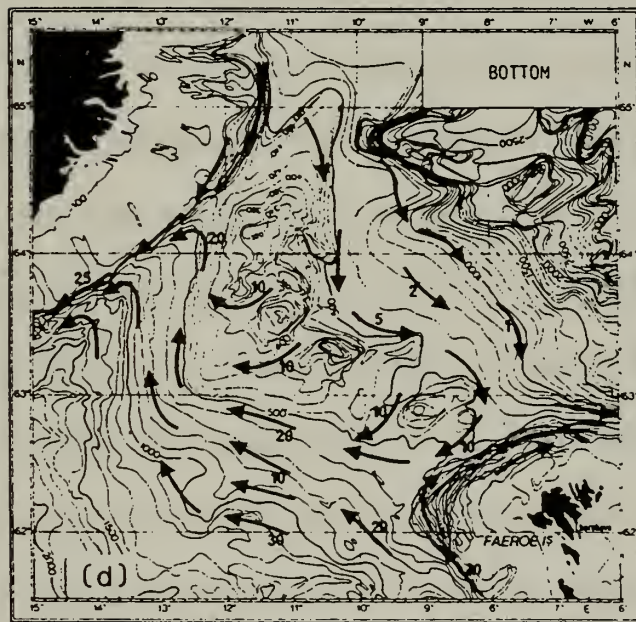
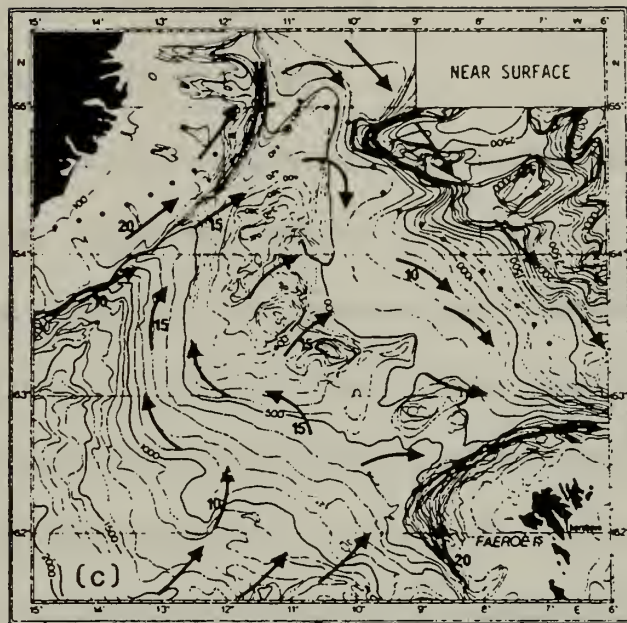


Figure 9. Schematic Representation of the Near-Surface and Bottom Circulation on the IFR According to Hansen and Meincke (1979). Arrows with numbers (cm/s) are based on measurements from moored instruments (from Becker *et al.*, 1973; Koltermann *et al.*, 1976).

III. DATA

A. THERMAL SATELLITE IMAGERY

Remote sensing of sea surface temperature (SST) from satellites provides a powerful source of data for research. The principal instrument for this task is the Advanced Very High Resolution Radiometer (AVHRR), a five channel scanning radiometer sensitive in the visible, near-infrared, and infrared 'window' regions. This instrument forms part of the payload of the TIROS-N series polar-orbiting satellites circling the earth about 840 km above the surface (Kidder and Vonder Haar, 1995). Channels 3, 4, and 5 cover the 'window' regions concerned with sea surface temperature (SST) determination as indicated in Table 1. Figure 11 is a color-enhanced MCSST image of the GIN Sea (clouds are black).

Even at these window wavelengths, infrared radiation is modified by its passage through the atmosphere by several processes, the most important of which are absorption and emission by various molecules, scattering and emission by aerosols, and obscuration by clouds. Transmittance in the Earth's atmosphere, broken down by individual gases, is clearly displayed in Figure 10. All spectral radiance measured at the satellite height above the sea surface is a function of optical depth of the atmosphere (Minnett, 1986).

Remote sensing of terrestrial temperatures is made possible through understanding that all materials above absolute zero temperature emit radiation. The perfect emitter, known as a blackbody, emits the maximum amount of radiation at each wavelength. Although some materials come very close to being perfect emitters in some wavelength ranges, no real material is a perfect blackbody. Planck's law states that blackbody radiation is a function of temperature and wavelength. For typical terrestrial temperatures (300 K), maximum

emission is in the thermal infrared ($\sim 10 \mu\text{m}$). Radiance received at the satellite radiometer is equal to the product of blackbody radiance times the surface emissivity and atmospheric attenuation plus the atmospheric blackbody emission integrated over the atmospheric optical depth.

The AVHRR has real time radiometric calibration, using an on-board black body target and a view of cold space (zero radiance in the visible and infrared). The temperature of the black body, which is close to terrestrial temperatures, is monitored by four platinum resistance thermometers. Even with this innovation, the accuracy of the spaceborne measurement of SST using a self calibration instrument is limited by the accuracy with which the effect of the atmosphere can be corrected (Minnett, 1990).

AVHRR data is tape recorded onboard the spacecraft and then downloaded. Local Area Coverage (LAC), which is used in this study, is 1.1 km high resolution coverage with a swath width of about 3150 km but only about 11 minutes can be stored on a single recorder. Global Area Coverage (GAC) is 4 km resolution and 115 minutes of this lower resolution imagery can be stored on a recorder, enough to cover an entire 102 minute orbit of data.

For the comparison of satellite-retrieved and in-situ drifter measured SST, it is essential that the data are from the same position and taken at the same time since SST is highly variable due essentially to mesoscale features such as fronts, currents, filaments, and eddies. Temporal coincidence of the satellite and drifter data is ensured by the fact that both are collected by instruments on the same satellites. Satellite imagery yields instantaneous synoptic views of SST. Over periods of only a few hours these structures may change

considerably, possibly by advection from surface currents. This must be taken into account when comparing satellite and ground truth data. Even if the satellite and ground truth data are from the same position and taken simultaneously, they may deviate (Essen *et al.*, 1996), as described below.

Satellite data refers to the uppermost millimeter of the sea surface (skin), whereas the drifter measurements are taken at about 40 cm below the surface (bulk). Because of the air-sea heat exchange, surface skin temperature is generally several 0.1 °C's colder than the bulk temperature due to the effects of surface solar heating, radiative cooling, and cooling from wind forcing. All the thermal energy from the sun is absorbed in the uppermost millimeters of the water column where turbulent mixing disperses the heat. In addition, the satellite-retrieved temperatures represent spatial averages over at least 1 km², while in-situ temperatures are from point measurements. (Essen *et al.*, 1996)

There are several processes involved in converting raw brightness temperature images to maps of SST. Beyond prelaunch calibration of the instrument, removal of cloud contaminated pixels by visual/infrared techniques, as well as coordinate transformation of the image to a geographical projection, are all paramount for accuracy (Minnett, 1991). Brightness temperatures measured by the infrared channels do not correspond to temperatures at the sea surface due to atmospheric effects. The largest error source in the computation of SST from infrared satellite imagery is the correction for signal attenuation by atmospheric water vapor. The standard multichannel algorithm (MCSST) uses the difference between two thermal infrared channels to correct for water vapor. Channels 4 and 5, which share the atmospheric window at 10-13 microns, are the channels where retrieval

methods use split-window algorithms for nighttime imagery. Daytime radiance received by channels 3 and 4 is converted into SST using a dual window algorithm. The coefficients for the algorithms are assumed to vary from satellite to satellite, and are different for day and night imagery (Essen *et al.*, 1996).

The net atmospheric effect on the radiation received by the satellite detector is to decrease it, underestimating the SST. The deficit depends primarily on the air-sea temperature difference. Since the atmosphere is less transparent for channel-5 than channel-4, the temperature measured in channel 5 (T_5) is generally cooler than the temperature measured in channel 4 (T_4) (Essen *et al.*, 1996).

The general algorithm for correcting atmospheric effects in SST measurements (Minnett, 1990) takes the form of a simple linear combination of the temperatures measured in the different channels:

$$SST = a_0 + \sum_{i=1}^n a_i T_i, \quad (1)$$

where n is the number of channels, a_0 is constant temperature, a_i are dimensionless coefficients, and T_i are the brightness temperatures measured in the different channels. The minimization of errors in SST measurements is dependent on the correct choice of the coefficients a_0 and a_i . The coefficients are determined by regressing satellite data with in-situ measurements from drifting buoys (Minnett, 1990).

The most frequently used method to retrieve SST from the AVHRR data is by means of a split window algorithm, which uses the difference between the brightness temperatures of channel 4 and channel 5 to correct for the atmospheric effects. These algorithms provide

the greatest accuracy, as they do not use channel 3 data, which can have random noise of up to 1.5°C (Essen *et al.*, 1996). The simplest split window algorithm is:

$$SST = a_0 + a_1 T_4 + a_2 (T_4 - T_5) + a_3 (T_4 - T_5) (\sec \Theta - 1) , \quad (2)$$

where a_0 is constant temperature, a_1 , a_2 , and a_3 are dimensionless coefficients, T_4 and T_5 are the brightness temperatures in channel 4 and 5, respectively, and Θ is the zenith angle. It's introduced to account for an increased optical depth of the atmosphere as the zenith angle increases (Essen *et al.*, 1996).

A second method to retrieve SST from the AVHRR data is with a dual window algorithm, which uses the difference between the brightness temperatures of channel 3 and channel 4 to correct for the atmospheric effects. It's not as accurate as the split window algorithm yet still is effective and usually used during nighttime to avoid contamination by direct solar radiation. The simplest dual window algorithm is:

$$SST = a_0 + a_1 T_4 + a_2 (T_3 - T_4) + a_3 (T_3 - T_4) (\sec \Theta - 1) , \quad (3)$$

where a_0 is constant temperature, a_1 , a_2 , and a_3 are dimensionless coefficients, T_3 and T_4 are the brightness temperatures in channel 3 and 4, respectively. (Essen *et al.*, 1996)

Empirical approach to coefficient determination requires the collection of high quality measurements from in-situ thermometers, such as on drifting meteorological buoys, that are coincident with satellite measurements. A regression analysis of the in-situ temperatures and the satellite data produces the coefficients. The global regression coefficients listed in Table 2 are provided by NOAA for the AVHRR instruments onboard the satellites used in this study. (Essen *et al.*, 1996)

A disadvantage to this method is that satellites measure skin temperature whereas in-situ measurements are bulk temperatures. Spatial and temporal variability in the SST field introduces uncertainty into the comparison: the satellite measurement is a near instantaneous spatial average, whereas the in-situ measurement is either a point sample, a temporal average at a given location, or a temporal and spatial average. The number of usable coincident sets of measurements is relatively small because many are invalidated by the effects of clouds in the satellite data. The presence of undetected clouds in the satellite data is an important source of error. Calibration errors in both the satellite and in-situ data are carried over into the SST retrieval expression. (Minnett, 1990)

According to Minnett (1990), there are a number of approaches for improving the error characteristics of satellite derived SST's in a regional study. The techniques are listed below in the order in which they improve the error characteristics:

Zenith Angle Dependence: Retrieval coefficients derived for near-nadir measurements applied to measurements toward the edge can result in mean errors in excess of 1 K. With increasing zenith angle, there is increased atmospheric path length and a decrease in the measured radiance at the satellite due to larger atmospheric emission with the increased path length away from nadir. Changing surface emissivity can be more important than increased atmospheric path length in terms of zenith angles.

Regional Dependence: The application of coefficients intended for global use in a regional study, such as the GIN Sea area, can result in mean errors up to 1 °K. The errors show a distinct zenith angle dependence.

Seasonal Dependence: Failure to account for the seasonal changes in the atmospheric conditions results in a small mean error. For example, applying coefficients derived from simulated measurements through cold, dry atmospheres of February to the simulated data from the warmer, moist atmospheres of July results in mean errors of only a few tenths of a degree. These surprisingly small errors indicate that the seasonal changes in the GIN Sea area are negligible and the global coefficients (MCSST) are thus applicable to this region.

Spacecraft Dependence: Individual sets of coefficients are required for each instrument, but for the GIN Sea conditions at least, the mean errors that arise when NOAA 9 coefficients are applied to NOAA 7 simulated data are small in the mean.

Spatial and temporal limitations: For calibration, maximum tolerable displacements between in situ measurements and the satellite data is 2 hours temporally and 10 km spatially. This also introduces small errors.

A definitive error budget for the AVHRR SST retrievals (Table 3) is now possible due to sufficient published work on the various sources of uncertainty in the instrument, and corrections for atmospheric effects.

Prelaunch uncertainty of the temperature and emissivity of the laboratory blackbody target, limits the absolute accuracy of the prelaunch infrared calibrations. Upon establishing earth orbit, in-flight calibration scheme assumes a perfectly linear response of the detectors over their full dynamic range. This is not the case and correction tables are necessary to account for the nonlinear response. In addition, combined random detector noise and digitization noise for Channel 4 and 5 is a small uncertainty. However, it can be reduced to negligible levels by spatially averaging over adjacent pixels.

The most optimistic estimate of AVHRR SST accuracy is obtained by combining in-flight calibration uncertainty and the smallest estimate of the residual atmospheric effects which are dependent on the atmospheric path length, errors increasing toward the edges of the image. This assumes that calibration errors are close to zero. (Minnett, 1991)

Sea surface temperature data verification via surface drifter ground truth is essential to determine the accuracy of algorithms that process the AVHRR data. The accuracy of ground truth data is a function of the instrument employed. Table 4 lists the instruments currently used for in situ data collection.

Lack of collocation and simultaneity between AVHRR SST measurements and in situ observations can produce small errors which are given in Table 5.

The most optimistic estimate of the accuracy of the AVHRR SST measurements would be derived by the combination of the in-flight calibration uncertainty, which is at best at the level of $\sim \pm 0.2$ °K, and the smallest estimate of the residual atmospheric effect, also at $\sim \pm 0.2$ °K level, which gives a resultant estimate of $\sim \pm 0.3$ °K. This assumes that the errors in the preflight calibration procedure are close to zero. (Minnett, 1991)

In summary, the accuracy of AVHRR SST retrievals should be in the range of ± 0.3 °K to ± 1.0 °K, with the best AVHRR SST retrieval accuracy achieved through a relatively dry atmosphere close to nadir (Minnett, 1991).

B. SHIP MEASUREMENTS

In situ SST measurements were made onboard NRV *Alliance* during the GIN92 and GIN93 surveys of the IFF. These data were a component of a shipboard meteorological monitoring system including measurements of apparent wind, air temperature, relative

humidity, barometric pressure, as well as the ship location, course and heading. The water temperature was measured at about 2 m below sea level with a Sea-Bird Electronics (SB-3) thermistor mounted on the ship's hull (port side). The ship's positions and SSTs were interpolated to a common time base with 5 minute spacing. At full speed, NRV *Alliance* moves approximately 1.6 km within 5 minutes, about the distance of an AVHRR resolution cell. Navigation information is available from the ship's differential GPS (Essen *et al.*, 1996).

C. DRIFTER MEASUREMENTS

The drifter employed during this experiment is the WOCE/TOGA Lagrangian drifter (Sybrandy and Niiler, 1991). The top flotation element is a small fiberglass sphere housing an Argos transmitter and controller, alkaline battery packs, drogue-presence sensor (sea water switch and strain gauge), and a thermistor for measuring SST. Attached to the surface float is a thin steel tether (coated in polyethylene) terminating in a holey-sock drogue, centered at 15 m nominal depth. A subsurface flotation sphere is attached to the tether about 3 m below the surface to dampen the rapid movement of the drogue assembly, caused by breaking wind waves. Between the surface float and the subsurface sphere is the area of greatest stress and the tether is strongly reinforced.

The sea anchor for the WOCE/TOGA drifter is an eight section holey sock drogue made of Cordura nylon, a plastic-backed fray resistant cloth. Figure 12 is a photograph of a WOCE/TOGA Lagrangian drifter recovered after 8 months in the Norwegian Coastal Current. The size of the drogue (6.41 m by 0.92 m) was chosen such that the drag coefficient times the total frontal area of the drogue divided by the sum of the products of the frontal

areas and drag coefficients of the tether and floats, i.e., the drag area ratio (R), is about 39 (Figure 13). With an R of about 39, the downwind slip of the drogue through the water is expected to be less than 0.1% of the wind speed (Niiler *et al.*, 1995). The climatological winter months mean resultant wind speed in the area of drifter data is less than 4 m/s (Hopkins, 1991). Thus, considering the downwind drogue slip percentage of the wind, the monthly mean wind-induced slip velocity is less than 0.4 cm/s.

The transmission period of the transmitter is 90 ± 6 s. The controller samples the thermistor once a minute and calculates an average temperature every 15 minutes. At the time of drifter manufacture, the SST sensor was calibrated to ± 0.1 °C in the range of -5 to 40 °C. The temperature data is transmitted with 0.1 °C accuracy and 0.05 °C resolution. (Poulain *et al.*, 1996b)

The time of last good temperature transmitted by Argos was estimated by examining the temperature records and comparing them to typical climatological values in the sea area. Failure of the temperature sensor was generally indicated by temperature values near -3.0 °C. (Poulain *et al.*, 1996b)

Drogue presence is monitored by timing the submergence of the surface float with a sea water switch. While the drogue is attached, drag causes the surface sphere to be submerged occasionally. If the drogue has been lost, the surface sphere remains at the surface and is not submerged by waves. When the surface float submerges, the contacts on the top of the sphere are shorted out by sea water. The controller measures the length of time the contacts are shorted and accumulates these values over a 30 minute time period. The submergence number is updated every 30 minutes. (Poulain *et al.*, 1996b)

Drifters deployed after October 1992 were equipped with a strain gauge transducer mounted on the inside of the surface float as a second drogue presence indicator since some sea water switch equipped drifters had failed to activate. Upon drogue separation, the submergence time monitored by the sea water switch decreases abruptly to about zero and the strain gauge will show a dramatic reduction of voltage range, giving a clear indication of drogue loss. (Poulain *et al.*, 1996b)

1. Argos Tracking and Telemetry

The Argos Data Collection and Location System (DCLS), installed on the NOAA polar-orbiting Tiros-N satellites, receives and processes all transmissions of the Argos transmitters aboard the Lagrangian drifters. Since the satellites orbit the earth approximately 14 times per day and two of them have the DCLS, the mean number of passes per 24 hours over the GIN Sea (latitude ~ 65 N) is 22 (Poulain *et al.*, 1996b). This frequent number of passes is essential for data analysis of this small scale, highly variable environment . Once the data from the drifters is transmitted to the passing satellite, it is retained until the satellite flies over a telemetry ground station where the information is finally downloaded.

The platform transmitter location is calculated from the Doppler shift of a fixed frequency signal (401.650 MHz) emitted by the drifter every 90 seconds. Constant Doppler shift corresponds to a field in the form of a half-cone with the satellite at its apex. The intersection of the various location cones obtained during the satellite overpass with the surface gives two possible positions for the transmitter. The ambiguity is removed using additional information such as previous location and range of possible speeds. Positions rejected by Argos include those with excessive erroneous frequency shift and unacceptable

distance from ground track. The drifter position accuracy, which depends on the inclination of the satellite orbit and on the number of transmissions received during the overpass, is provided by Argos in terms of location classes. From all the temperatures obtained during a typical overpass of some 15 minutes, the median value is calculated and assigned to the drifter location (Poulain *et al.*, 1996b).

With the Argos System operational on two satellites (NOAA 11 and 12), position fixes average about seven during an 8 hour period, the most frequent being nine fixes. The transmitter battery conserves power by remaining dormant 16 of every 24 hours. These relatively high statistics show that the sampling rate of the Argos DCLS is optimum for the high latitudes of the GIN Sea (Poulain *et al.*, 1996b).

2. Drifter Deployments

During the period June 1991 to August 1993, Argos-tracked drifters, drogued to 15 m depth, were released by the NATO SACLANT Undersea Research Centre La Spezia, Italy in the Greenland-Iceland-Norwegian (GIN) Sea to study the variability of the near surface circulation and temperature fields at scales ranging from a few kilometers (mesoscale) to thousands of kilometers (basin-wide large scale) (Poulain *et al.*, 1996b). Individual drifter releases in the southern GIN Sea area are displayed as red stars in Figure 14. The majority of drifter releases occurred over the Iceland-Færoe Ridge which is defined by the 600 m isobath. The drifters provided detailed coverage of SST structures that can be used to compliment ocean acoustic measurements and prediction of operational ocean acoustic environmental models, and to study the movement characteristics of water masses (Poulain *et al.*, 1996b). Drifter data are also used to validate satellite sensed oceanic parameters.

Drifter deployments began in June 1991 and by August 1993, 107 drifters had been released from various research vessels and volunteer observing ships. By April 1995, approximately 31,000 days of drifter data had been acquired through Service Argos. The drifter position data were used to construct a velocity data set, from which maps and statistics of the near surface circulation were made. (Poulain *et al.*, 1996a)

3. Data Distribution

The two largest drifter releases were conducted in October 1992 and August 1993 during major hydrographic surveys of the Iceland-Færoe Front (IFF), termed GIN92 and GIN93, respectively. GIN92 was conducted from 12-29 October 1992 (18 days), and included drifter releases, deployments of current meter moorings, and shipboard measurements of water characteristics principally in the IFF. GIN93 occurred from 11-26 November 1993 (16 days), and included similar measurements.

Some 59 of the 107 drifters were deployed within the boundary limits of this study, i.e., 60-70° N and 0-20° W. The drifters were tracked for their entire lifespan up to a maximum of 3 years. Circumstances surrounding termination of data from a drifter were closely studied to determine the cause of the untimely end. Drifter failure was classified into one of four categories: Grounded; Picked-up (fisherman); Battery Failure; Ice edge/Sinking.

The half-life of the drogues in the environment of the GIN Sea was about 157 days, compared with the half-life of transmitters of 190 days. In other words, 50% of the drogues (transmitters) were still operational after 157 (190) days. Thus, two thirds of the data set correspond to drogues with drifters and one third corresponds to the surface floats with no drogue attached. (Poulain *et al.*, 1996a)

Figure 15 shows the number of drifter-days per day versus Julian days in the GIN Sea referenced to January 1991, while Figure 16 shows the same distribution but in the area of interest only. With numerous drifters deployed simultaneously, large amounts of data were processed using several statistical and editing techniques which are explained in detail by Poulain *et al.* (1996b). We will now discuss the major procedures.

4. Data Editing

Editing of location data was the first of several efforts to despike the data. For each drifter, a range of physically possible values of latitude and longitude were defined. Data points outside this range, or flawed latitude or longitude points, were flagged. The records were arranged in ascending temporal sequence. Velocity components were estimated for each satellite separately by finite differencing successive positions. Only velocities computed from the data points inside the same 8-hour transmission window were considered.

Since an unreliable velocity observation corresponds to two position points, the point with the lowest location class was chosen as the flawed observation. In the case of a pair of points with identical classes, the previous and successive velocity magnitudes were used. If the previous (successive) velocity magnitude is larger than the successive (previous) one, the first (second) point was considered flawed.

At the end of the statistical editing process, the data of the different satellites are recombined into a single sequence series. Records with identical times were reduced, retaining only the data stream corresponding to the highest location class, or to the location more similar to the adjacent data points. Those records not flagged were written in a position-edited file (named a P-file) containing the position time, latitude, longitude and

location class. When the position time series are scrutinized, remaining spikes were removed using a manual interactive program which flags the corresponding records in the P-file.

Temperature editing was the next step in the process. For each satellite, the temperature gradients were computed from successive fixes within the same 8-hour transmission time period. When only one temperature record was available in the 8-hour window, this value was compared to the mean temperature during the preceding and subsequent 8-hour time periods, and rejected if both variations exceeded 0.15 °C (threshold value obtained experimentally and equal to three times the temperature resolution).

At the end of the temperature editing process, the data corresponding to the different satellites were combined and records with identical times were reduced. The temperature time series were edited manually and all sensor data records (time, submergence, temperature and battery voltage) are written in a sensor-edited file (called S-file).

The final step required was interpolation and filtering of the data. The despiked data were interpolated into regular intervals using an optimum analysis technique known as Kriging (Hansen and Herman, 1989; Hansen and Poulain, 1996). The Kriging used here employed an analytic function fit to a structure function computed from the entire despiked data set.

The edited drifter data were interpolated at regular 2-hour intervals using the Kriging technique. Following experimentation, 20 observations were selected, 10 preceding and 10 following each interpolation point, to carry out the Kriging interpolation technique. When data are few, as at the beginning or end of a drifter life, or when data are intermittent, interpolations were done with as few as a single observation on either side of the

interpolation time. Both the interpolated value and an estimate of its accuracy were computed. The interpolated positions and SST were then low-pass filtered with a designed filter cut-off period at 36 hours in order to remove high frequency current components, especially the strong tidal and inertial currents. The low-pass time series were finally subsampled every 6 hours and the velocity was computed by finite centered differencing the 6-hourly interpolated/filtered position data. The processed data files (called K-files) contain 6-hourly observations organized in columns of time, latitude, longitude, temperature, u-component, and v-component. If the time difference between the interpolated point and the closest edited observation is larger than 3 days, the corresponding velocity was flagged in order to avoid meaningless interpolated velocity estimates in large data gaps.

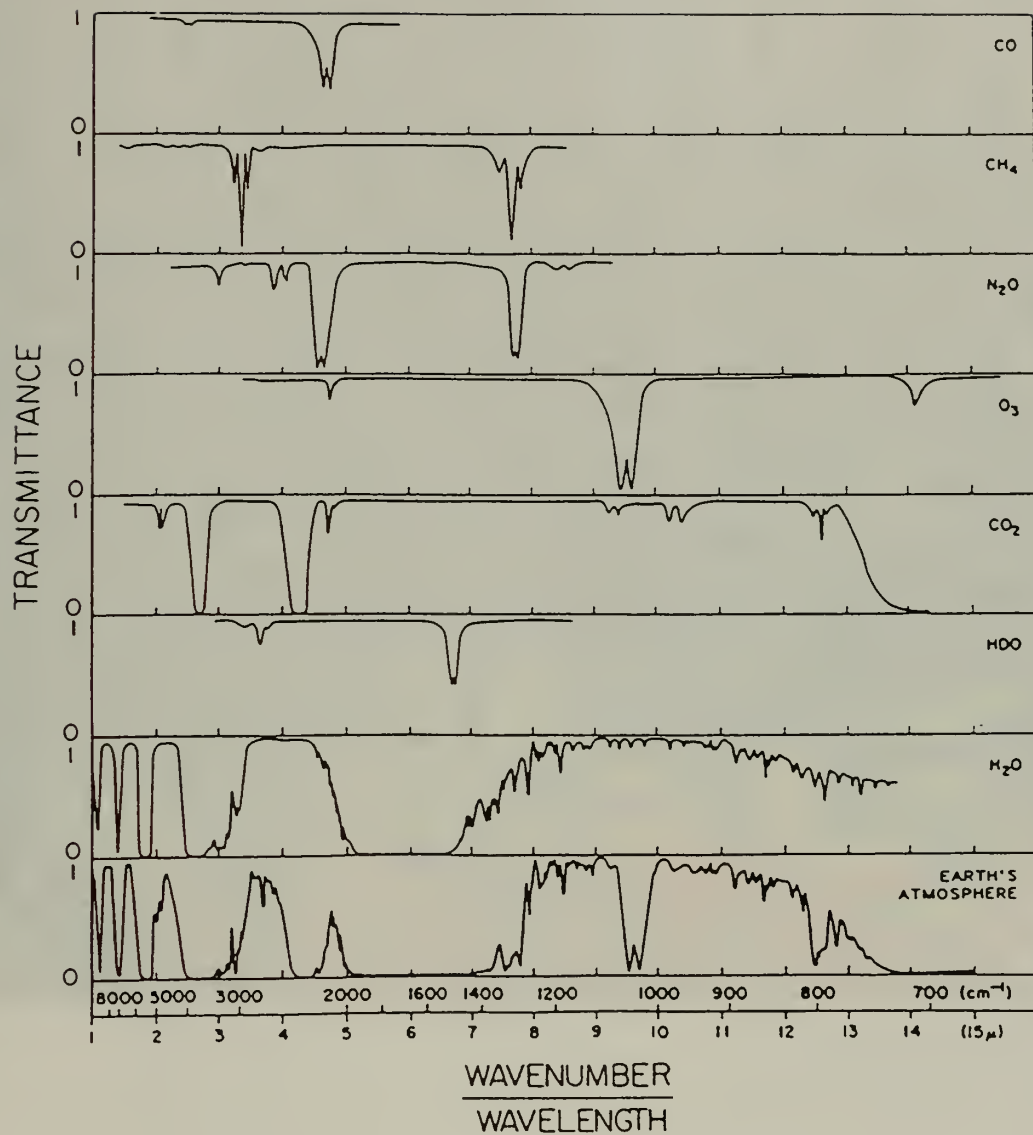


Figure 10. Infrared Transmittance of Several Gases in the Earth's Atmosphere and Combined Total Atmospheric Transmittance (from Kidder and Vonder Haar, 1995).

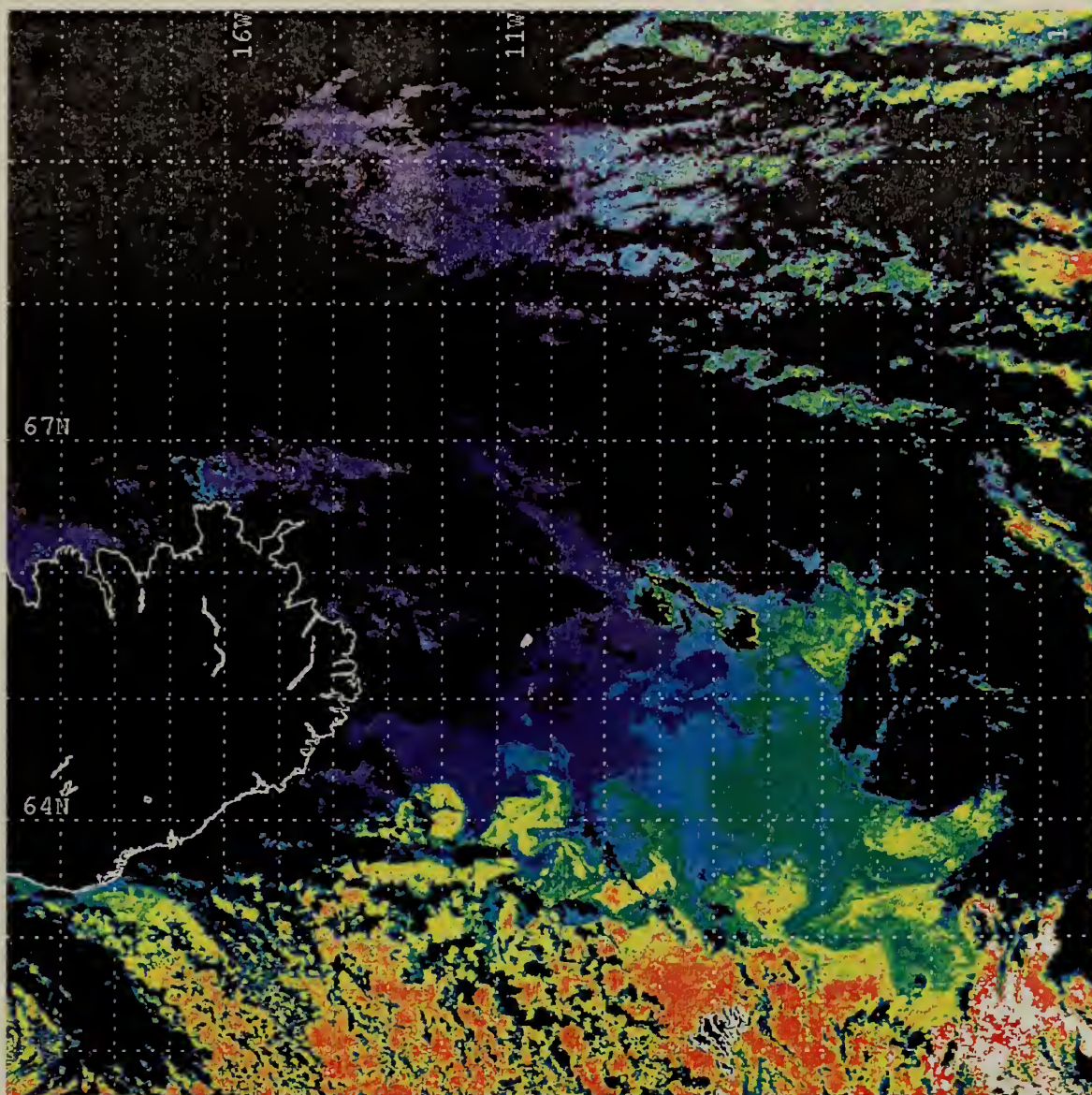


Figure 11. AVHRR Image of the GIN Sea Area from NOAA 11 Polar Orbiter, 1514 UTC 24 October 1992.



Figure 12. Photograph of a WOCE/TOGA Lagrangian Drifter Recovered after 8 Months in the Norwegian Coastal Current (from Poulain *et al.*, 1996).

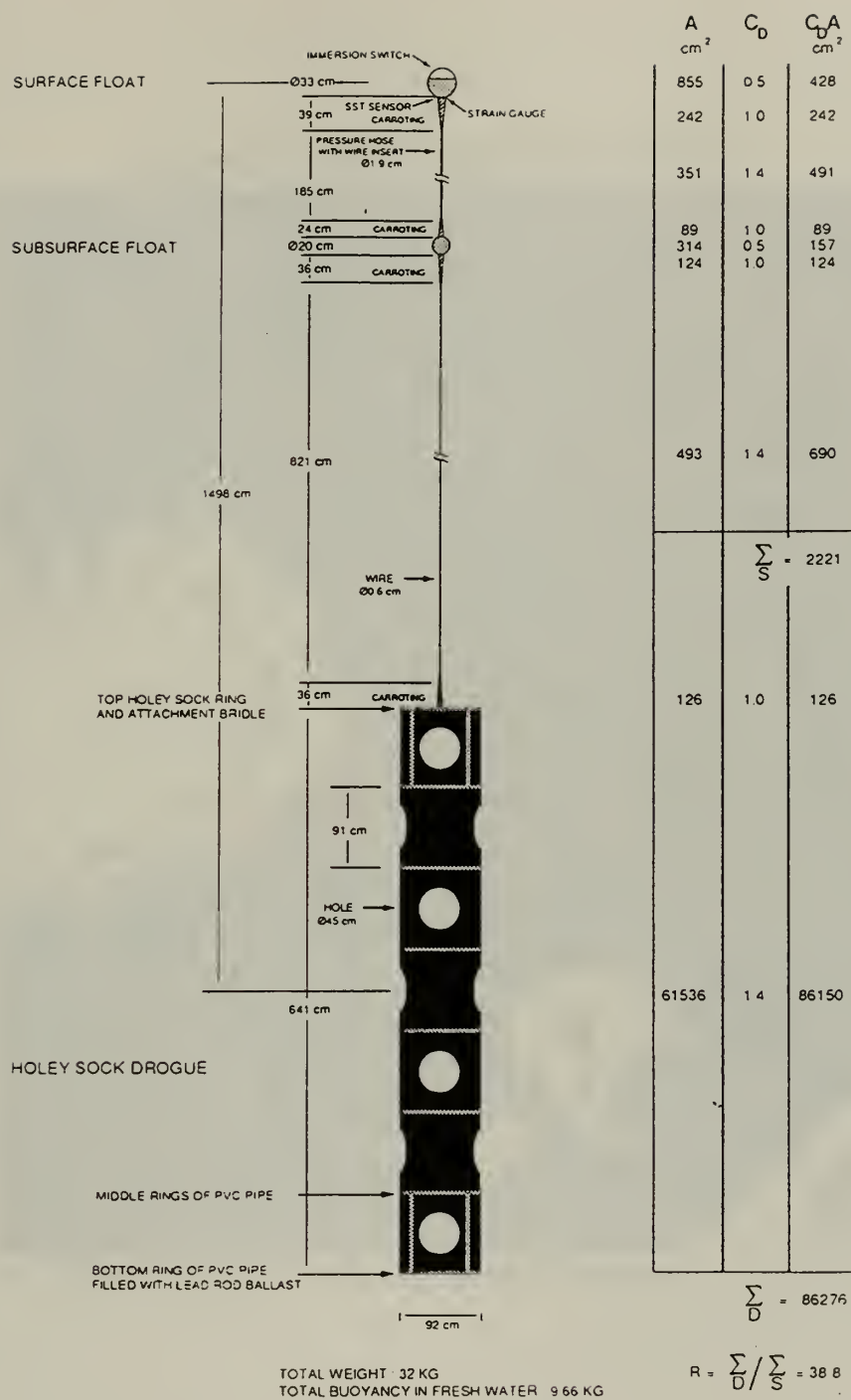


Figure 13. Schematic Diagram of the WOCE/TOGA Lagrangian Drifter with Computation of Drag Area Ratio (from Poulain *et al.*, 1996).

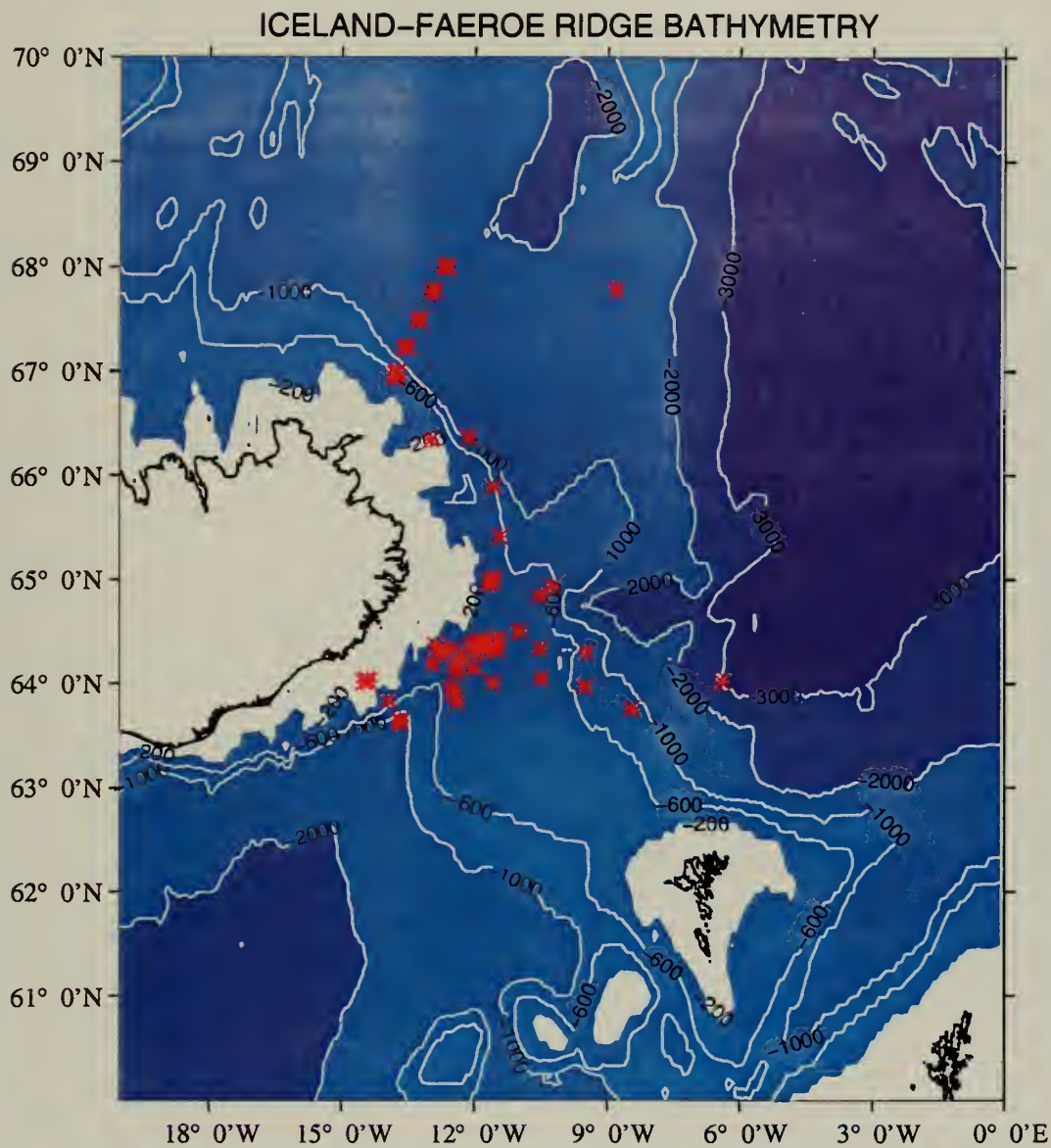


Figure 14. Individual Drifter Release Sites (Red Stars) Overlaid on Iceland-Faeroe Ridge Bathymetry.

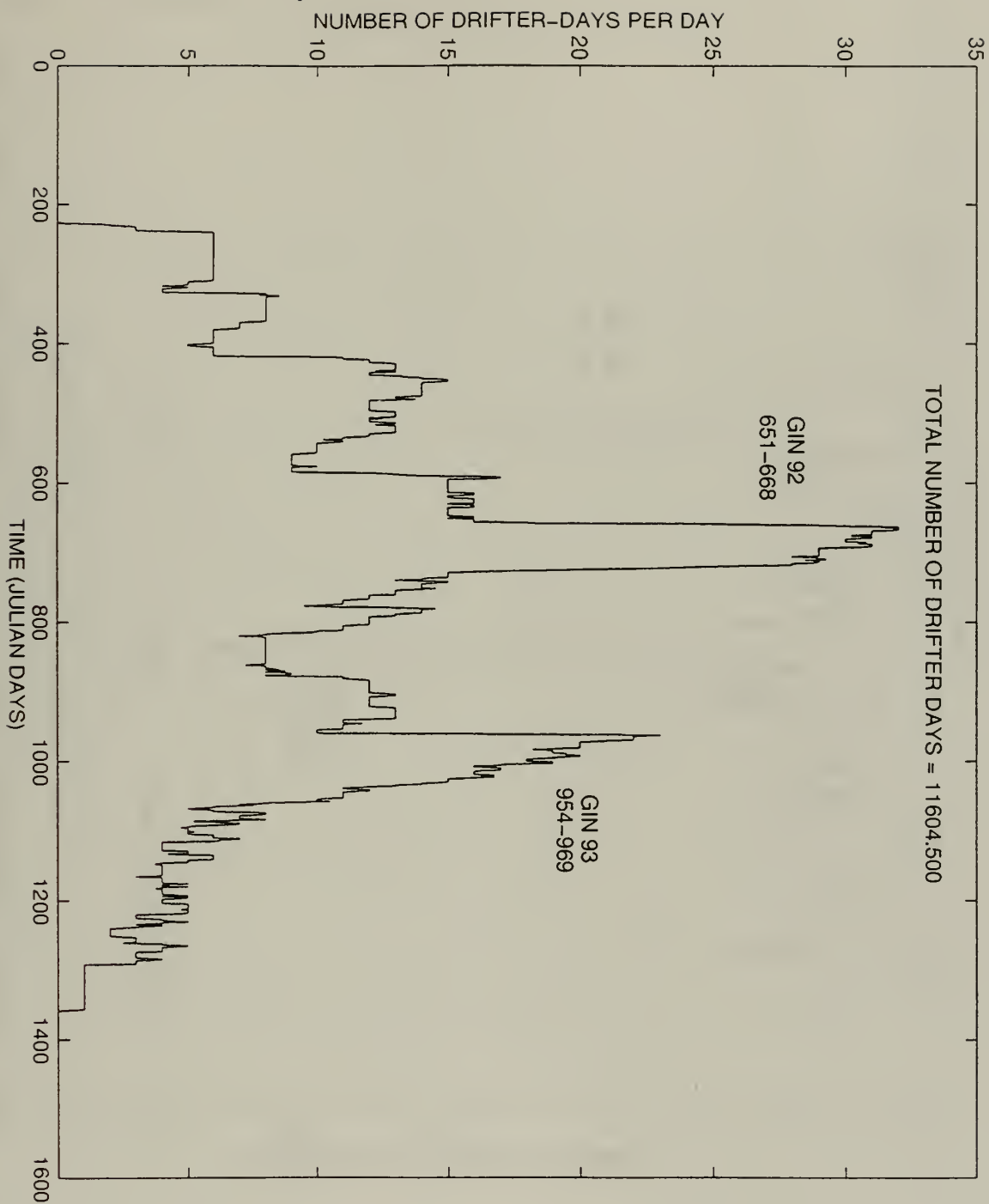


Figure 15. Number of Drifter Observations (Drifter-Days per Day) in the GIN Sea as a Function of Time.

Table 1. AVHRR Channels with Corresponding Wavelengths (Kidder and Vonder Haar, 1995)

Channel	Wavelength (microns)	Primary Uses	Characteristics	Atmospheric Effects
1	0.58 - 0.68 VISIBLE	daytime cloud mapping	solar reflection and scattering	scattering of air molecules / aerosols
2	0.725 - 1.10 NEAR-IR	surface water delineation, ice and snow melt	solar reflection and scattering	scattering of air molecules / aerosols
3	3.55 - 3.93 NEAR-IR	sea surface temperature, nighttime cloud mapping	solar reflection / thermal emission	water vapor window
4	10.30 - 11.30 THERMAL IR	sea surface temperature, day and night cloud mapping	thermal emission of ocean, clouds, and atmosphere	water vapor window
5	11.50 - 12.50 THERMAL IR	sea surface temperature, day and night cloud mapping	thermal emission of ocean, clouds, and atmosphere	water vapor window

Table 2. NOAA Coefficients for Global SST Retrieval Algorithms (from Essen *et al.*, 1996).

ALGORITHM	SATELLITE	TIME	a_0	a_1	a_2	a_3
Split Window	NOAA-11	day	-0.918	1.0135	2.6598	0.5265
Split Window	NOAA-11	night	-1.316	1.0520	2.3971	0.9598
Split Window	NOAA-12	day	-0.912	1.0137	2.4435	0.3143
Split Window	NOAA-12	night	-0.912	1.0137	2.4435	0.3143
Dual Window	NOAA-12	day	1.731	1.0177	0.4266	1.8010
Dual Window	NOAA-12	night	1.731	1.0177	0.4266	1.8010

Table 3. Error Budget for AVHRR Measurements (from Minnett, 1991).

INSTRUMENT ERRORS	UNCERTAINTY (KELVIN)
SOURCE OF UNCERTAINTY (PRELAUNCH)	
BLACK BODY TARGET	UP TO +/- 0.35
CALIBRATION TRANSFER	+/- 0.1
SOURCE OF UNCERTAINTY (INFLIGHT)	
NONLINEARITY CORRECTION	+/- 0.1
DETECTOR NOISE / DIGITIZER	+/- 0.05
TOTAL INSTRUMENT ERROR	+/- 0.2 TO +/- 0.4
ATMOSPHERIC EFFECTS	+/- 0.2 TO +/- 0.6
TOTAL ERROR	+/- 0.35 TO +/- 1.0

Table 4. Individual High Quality in situ Instruments Listed from Most Accurate to Least Accurate (from Minnett, 1991).

SOURCE OF UNCERTAINTY	UNCERTAINTY (KELVIN)
CTD	< +/- 0.01
BUOY	+/- 0.1
RADIOMETER (SEA LEVEL)	+/- 0.1 TO +/- 0.25

Table 5. Spatial and Temporal Variability Errors Between AVHRR and in situ SST Measurements (from Minnett, 1991).

SOURCE OF UNCERTAINTY	SOURCE OF UNCERTAINTY
SPATIAL GRADIENTS	<~ +/- 0.2
TEMPORAL CHANGES	<~ +/- 0.2

IV. METHODS

A. REGRESSION OF DRIFTER SST VS. SATELLITE SST

A total of eleven AVHRR partially cloud-free images over the IFR region were available to us between October 1992 and September 1993. Listed in Table 6, the images were processed (navigation, registration, calibration, cloud masking, and atmospheric correction) at the NATO SACLANT Undersea Research Centre La Spezia, Italy.

The method used to compare the satellite-retrieved SST's and the SST measurements from drifting buoys is as follows: The date and time of each satellite image was translated into a Julian day (referenced to 1 January 1991) for ease of comparison with the drifter data. This value for a specific satellite pass was entered into a MATLAB program that produced a list of all the drifters in the study area near the time of the overpass, along with their respective latitude/longitude and temperature. If the drifter observations were recorded before or after the time of the satellite image, a linear interpolation routine in the program code calculated the percentage of time difference between the observations and the satellite image, then applied the percentage of change to the difference between in situ temperature observations and recorded the value.

The list of location data for each drifter was used to manually extract pixel temperatures from the satellite image using the TeraScan system. Cloud contamination was widespread on many images, from complete masking to reduced SST readings due to cloud influences within individual pixels. Pixel temperatures that deviated greatly from expected values due to proximity to cloudy regions were omitted. Even with cloud masking problems, there was an abundance of temperature data extracted from the satellite images. All 109 SST

observations (in-situ and remotely sensed) are listed in the appendix (Tables 8a-8k) and correspond to the date and time of the 11 satellite images used in this study. The satellite retrieved SST values were compared with the drifter measurements by using a regression analysis (Figures 17 and 18).

Figure 17 is the result of a simple linear regression between in-situ drifter measurements and satellite retrieved temperatures from October 1992 to September 1993.

The square of the correlation coefficient (r^2), which represents the percentage of variation in Y explained by a variation in X, is a measure of the "goodness of fit". For this case $r^2=0.84$, which is quite good. However, during GIN92 alone, $r^2=0.91$ (Figure 18). These results indicate that the satellite-derived SST's are accurate to within 0.1 °C. When combined, the satellite and in-situ measurements are used to construct SST fields (see Subsection E). No further correction or adjustment of MCSST will be applied because the regression bias is less than 1 °C.

The elimination of noise- and cloud-contaminated pixels is essential for obtaining reliable SST's from satellite measurements. In summary, the satellite retrieved temperature observations were very similar to in-situ measurements due to improvements in SST retrieval algorithms developed over the past several years.

B. SURFACE VELOCITY FIELD FROM DRIFTERS

With the drifter data well organized and tabulated in P, S, and K-files, several MATLAB programs were written to visualize the data with various time scales. Monthly "spaghetti" plots of the drifter trajectories (Figures 19-35) revealed the flow from the eastern coast of Iceland to an area north of the Færoe Islands. Star symbols indicate the location of

initial drifter deployment, while circles at the end of the trajectory denote the last observation during the time frame of the plot. A closed, shaded circle means the transmitter failed during the time of the plot while an open circle signifies that the drifter was still operating at the end of the period. Crosses are imbedded in the trajectories every seven days. The distribution of these crosses, whether packed together or spread apart, gives a rough estimate of the flow speed. Dotted trajectories are symbolic of drogue loss for that specific drifter, making the surface buoy completely susceptible to surface wind forcing, thus eliminating trajectory influences by the underlying currents. Current data from these drifters were not considered but SST data still proved to be valuable.

Each monthly plot, except the initial plot of August 1992, is a continuation of the drifter trajectories from the previous plot. The circle symbol at the end of a monthly trajectory becomes a star symbol on the following plot. The flow field in August and September 1992 revealed several features. In general, drifters released east of Iceland are swept eastward toward the Færoe Islands by the flow along the IFF.

In August, two drifters were caught in an anticyclonic (warm core, approximately at 12° W, 64° N) eddy imbedded in the flow field, which is an uncommon event. Usually the most common eddies are located south of the IFF and are cyclonic (cold core) (Niiler *et al.* 1992), as we will see for other months. A third drifter in the region failed shortly after deployment and was unable to provide further data on the warm northward intrusion. The most northern drifter of the cluster in the IFF showed the signature of a cyclonic (cold core) eddy just north of the anomalous warm core eddy. The eddy affected the drifter's trajectory at the end of August into early September.

Drifters released north of the IFF in the Norwegian and Iceland Seas showed good agreement with the cyclonic gyre on the Iceland plateau depicted in Figure 3. Drifters northeast of Iceland appeared to operate in an area of stagnation, likely trapped in the middle of the gyre where rotational velocities are minimum. Two drifters over the eastern continental shelf of Iceland were likely caught in the Icelandic Current (IC) as they eventually enter the IFF in September. During this month, IFF drifters moved farther eastward. They appeared to converge and accelerate when passing just north of the Færoe Islands

Numerous drifters were released into the IFF during GIN92 in October (Figure 21). The three drifters from the previous two months remained on the eastern limits of the figure. The drifter just northeast of the Færoe Islands clearly encountered an anticyclonic (warm core) eddy before exiting the area of interest. Additionally, two drifters south of the main cluster defined a cyclonic (cold core) eddy.

An un-drogued drifter (dotted trajectory) initially situated approximately 67.5° N, 14° W traveled a great distance in a southerly direction possibly indicating strong northerly wind forcing. Upon entering the IFF in late October, the un-drogued drifter was influenced by the flow until possible strong winds in late November (Figure 22) forced it more northerly than the drifters bound by the flow field. Further investigation revealed a return to the flow field in December (Figure 23) suggesting the drifter may have followed a warm intrusion into the GIN Sea during November.

As the drifters proceeded eastward encountering numerous eddies and meanders, a belt of confluence marked an area of zonal flow for many of the drifters (Figures 22, 23).

The drifters converged at around 63.5° N and 7° W and remained tightly clustered together for approximately 200 km. The distribution of imbedded crosses in the trajectories describes a rapidly moving surface current. December shows the drifter trajectories spreading apart, representative of the flow entering a region of horizontal divergence.

The January 1993 plot (Figure 24) has a limited number of tracks, yet significant amounts of information were found. Nearly all the drifters deployed in mid-October during GIN92 had left the area of interest, having spent nearly 10 weeks in the rapidly moving and dynamic IFF. The increased number of un-drogued drifters (dotted trajectories) is directly correlated to the severe North Atlantic winter conditions and the subsequent wear and tear on the drifter system. Drifters that were initially influenced by the cyclonic gyres of the Norwegian and Iceland Seas broke free and started to enter the IFF.

One drifter deployed northeast of Iceland prior to GIN92, was delayed from entering into the IFF circulation system by a small eddy feature. After being trapped by the fast IFF flow, it made a dramatic dip to the south between the Færoe and Shetland Islands during February (Figure 25) before resuming course to the east. Re-examining the passage of the main drifter cluster through this area in December 1992 showed that most drifters altered course to the south. The Færoe-Shetland Channel splits the ridge separating the Færoe and Shetland islands as seen in bathymetry (Figure 14). The flow is evidently bathymetrically steered along the ridge line and around the deep channel, and then continues toward the Norwegian coast. Poulain *et al.* (1996a) showed that steering around the Færoe-Shetland Channel continues farther north as most of the flow moves along bathymetry lines and eventually reaches the Polar Sea via Fram Strait.

In March, three drifters define the IFF flow during that period (Figure 26). One drifter failure is apparent over the Færoe-Shetland Channel where the bathymetrically-steered drifter described in February made a hasty exit from the area of interest. Comparing the length of the three trajectories within the IFF to those to the north clearly suggests greater flow rates in the IFF. As the remaining two drifters pass north of the Færoe Islands in April (Figure 27), they became trapped in languid waters, moving northerly for months: one exits the area in July, the other remains until September. Drifters that are still loitering in the cyclonic gyres north of the IFF remained in this status through July when approximately half made it into the IFF and were swept eastward. Of the remaining three in the gyres, two became un-drogued by August and the one closest to Iceland entered the IC which eventually transported it into the IFF and out of the area by the new year.

Three new drifters were deployed in the IFF during May (Figure 28). Two of the three were immediately moved by the flow field and encountered an anticyclonic (warm core, located approximately 64° N, 10° W) eddy in June (Figure 29). Examining the imbedded crosses to estimate the translation speed of this mesoscale feature, one drifter encountered it during its second week of movement while the other drifter passed around the eddy in its fourth week of movement. This suggests that the eddy was quasi-stationary in the flow field during June.

The second major drifter release (GIN93) was conducted in August 1993. Throughout this month and into September (Figures 31, 32), the tracks were initially zonal and then became convoluted by mesoscale meanders and eddies. A drifter from an earlier release made three complete revolutions during August and September around a cyclonic

(cold core) eddy over the Færoe-Shetland Channel ($\sim 61^\circ$ N, 4° W). The revolutions took approximately six weeks to complete before the drifter left the area.

A large anticyclonic recirculation was sampled in September by the southwestern most drifter whose course was completely altered in a clockwise direction from northerly to westerly and eventually back to a northerly heading. It appears that once the drifter was caught in the recirculation feature, it translated northwest with the lateral motion of the disturbance over a period of three weeks. It is highly unusual for a drifter to move opposite to the mean flow field unless other forces are involved. Smaller cold core eddies can also be seen within the IFF.

A large warm core eddy was evident when two full rotations were made by a drifter during October (Figure 33). This eddy, however, is well north of the IFF located approximately at 66.3° N and 2° W. It was possibly created by an instability of the Norwegian Atlantic Current (NwAtC) which transports NAW northward through the Norwegian Sea from the Færoe-Shetland Channel into the Greenland Sea. Throughout the northward course of the NwAtC embedded elongated eddies are formed due to variations in cross-stream shear generated by interaction with the bathymetry.

November and December 1993 corresponds to the end of drifters in the area of interest (Figure 34, 35). The strong currents prevent long residence times in the area, except when drifters were trapped in the large cyclonic gyres north of the IFF. Eventually, the gyres transport the drifters into the main flow field, expediting their removal from the IFF.

The color, composite "spaghetti" diagram (Figure 36) displays drifter trajectories through the entire time period (517 days) and area of interest. Local circulation patterns are

exposed and the flow field in the IFF is accentuated. As indicated by the legend, the color coded trajectories represent the different time periods of each drifter release in the region. Between Iceland and the Færoe Islands, the IFF is dynamically active with warm and cold intrusions, instabilities, eddies, and large meanders of the mean flow. All of these flow perturbations caused the drifter trajectories to be convoluted and to cover a large area from 62.5°-64.5° N. However, the flow entered an area of convergence north of the Færoe Islands and moved zonally until it reached the entrance to the Færoe-Shetland Channel where the drifter tracks horizontally diverged. Since the drifter tracks represent numerous deployments over a 517 day period, areas of horizontal convergence and divergence are thought to be significant features in the flow field of the IFF. North of the IFF, drifter tracks demonstrated long residence times as they slowly migrated in large gyres and areas of reduced flow. The composite plot cannot demonstrate detailed instabilities like the monthly plots, but the mean flow and mean perturbations to the flow are evident.

C. SST IMAGES AND DRIFTER DISPLACEMENTS

For the satellite pictures obtained for this study, each one was manually navigated to ensure the greatest accuracy possible. The direct comparison of drifter tracks, superimposed over SST features, was made possible using a MATLAB program (Figures 37-47). Essentially, the program first defined the spatial limits of the image which were determined with careful navigation, then ensured that the correct palette was established where white was cold water and black indicated warm water, and then ingested the 512 x 512 pixel TeraScan image. Once the image was loaded, the coastline was overlaid as well as the drifter tracks,

beginning a day before the time of the image and ending the day after. The symbols displayed along the tracks are identical to those on the "spaghetti" plots (Figures 19-35).

The first two satellite images (Figures 37, 38) have considerable cloud contamination, but the IFF is clearly visible in the cloud-free area southeast of Iceland. The darker water is the warmer North Atlantic Water (NAW) and the light grey water represents the colder waters of the GIN Sea. The 19 October 1992 image shows a cluster of drifters moving rapidly along the frontal boundary. Except for a cold intrusion east of the drifters, the IFF appears simply as a straight east-west boundary.

On 22 October 1992, many drifters were already deployed, but cloud coverage allows only speculation as to their true interaction with surface features. Growing instabilities may explain the sudden curvature in the trajectories which were relatively zonal two days earlier. An anticyclonic (warm core) eddy was possibly responsible for the clockwise drifter tracks around 64° N and 10° W. Just west of the cloudy area along the IFF, a warm instability is forming. The bulge of warm water grew in a northerly direction over time and become known as the "blob" instability.

The next four satellite images (on 23 and 24 October 1992, Figures 40-43) show remarkable agreement between drifter tracks and surface instabilities. Specifically, the warm surface feature at 64.25° N, 10° W, shaped like a "knight's helmet", will be studied throughout the sequence. Beginning with the only image on 23 October, note the drifter tracks are completely controlled by the edge of the "knight's helmet" instability. The drifters moved in a clockwise manner typical of a warm core eddy. The drifters did not penetrate into the feature but remained at the dynamic boundary between the water masses. A smaller

cold core instability can be seen just south of the main warm core eddy, and it became evident due to a cyclonic sense of rotation of individual drifters trapped along its edges. Further data was needed to substantiate whether these eddies were a counter-rotating eddy pair.

The first of three images on 24 October 1992 (0845 UTC, Figure 41), clearly shows the developing "knight's helmet" instability. The feature protruded well into the cold GIN Sea waters and continued to steer drifters around its periphery. The second and third images that day (1335 and 1514 UTC respectively, Figures 42, 43) revealed more instabilities in the flow field as the clouds began to clear. West of the "knight's helmet" instability, the large "blob" instability grew and protruded into the GIN Sea. As the flow translated the "blob" to the east, it may have become too unstable and 'pinched off' or remained attached like the "knight's helmet". Farther to the east (63.5° - 64.5° N and 8° W), a northward intrusion of warm water can be seen but it appears to be diffuse due to mixing with the surrounding cold water. At its base the intrusion is warm (dark), but as it entered the GIN Sea it became colder (lighter) as it cooled through horizontal turbulence and vertical mixing including salt fingering and double diffusive layering. Finally, the eastern most instability shaped like a "fist" protruded in colder waters north of the F  roe Islands.

November 17th provides another example of drifter trajectories influenced by surface features (Figure 44). Two drifters, nearly due north of the F  roe Islands, outlined the cyclonic motion of a cold eddy while three others flowed eastward across a counteracting warm intrusion ($\sim 63.5^{\circ}$ N, 8° W).

December 25th (Figure 45) proved to be a relatively cloud-free day over the IFF, but unfortunately the drifter data were sparse. The IFF is well defined and instabilities were at a minimum, except for a small cold intrusion around 10° W. The most prominent feature was the large northward meander just east of the Icelandic shelf break. This is the region known as the "Red Square".

The last two satellite images were taken during and after the GIN93 experiment. A relatively permanent southward projecting cold intrusion near 9° W persisted for over a month with little change, from 22 August until 25 September 1993 (Figure 46, 47). The feature migrated about 1° eastward between satellite images. In the August 22nd image the eastern outflow of the intrusion dominated the cluster of drifters launched as part of GIN93, moving them rapidly eastward. One drifter on the western outflow region of the intrusion was forced northward as the cold water curled clockwise back toward its origin in the GIN Sea. The September imagery displayed a similar situation where another drifter flowed in the direction of the western outflow region of the intrusion.

Also apparent on the 22 August satellite image, were two imbedded eddies of warm water north of the intrusion. Rotation within these features is unknown due to the lack of ground truth drifter data, but because these eddies are warm, it can be inferred that rotation is anticyclonic.

D. SST FEATURE DISPLACEMENTS AND SURFACE VELOCITY FIELD

Surface current computation from sequential infrared satellite images employs a technique called feature tracking, where surface temperature features are visually identified in a series of satellite images (Emery *et al.*, 1992). The displacements of the SST features

are computed by repeatedly displaying each of the images to subjectively determine the movement of the surface temperature patterns. This technique is time and labor intensive.

SST feature tracking is valid only if SST can be considered a passive tracer that is advected by the surface currents. Moreover, it is also completely subjective in the selection of surface temperature features to be tracked and is limited by the ability of the operator to locate the same features in each of the sequential images. The spatial resolution of the motion vector field is a function of the number of features tracked, requiring a greater investment in time and effort for a higher spatial resolution in the final vector field (Emery *et al.*, 1992). Precision depends on the quality of the navigation performed on the images. In our case, each image was navigated independently using recognizable land masses (Iceland and the F eroe Islands), ensuring the best possible accuracy.

Of the eleven satellite pictures obtained, four were selected to study instability development rates during an active 48 hour time frame (Table 7). To better visualize the growing instabilities and estimate speed and direction, the limits of the image were decreased such that only the northern F eroe Islands and very eastern coast of Iceland were visible. This area encompasses the IFF.

Employing the TeraScan system, individual points on prominent SST features recognizable in two sequential images, were tagged with the cursor and the exact latitude and longitude were manually recorded. Between 20 and 48 distinct points (see Table 7) from SST instabilities were recorded as location data for each image. This process was repeated for the image that immediately followed the initial image and the same selected points were carefully located. Even though lateral translation of the features to the east was evident,

deformation of the instabilities during the time frame was minimal. This continuity of feature size and shape helped ensure that the same points were selected from one image to the other.

Because knowledge of the location data at the beginning and end of a specified time frame is required, a time-distance problem emerged. A MATLAB program was created to compute course, speed, and distance traveled by the SST features from given latitude and longitude data. Velocity vectors were overlaid as arrows on the second sequential satellite image. Furthermore, the drifter velocities coincident with the time frame of the image pair were plotted as cyan colored arrows for comparison. Each image pair is examined below in chronological order.

From 23 to 24 October (Figure 48), many features were visible yet vector magnitudes revealed a rather slow moving IFF over a time frame of 17.28 hours. The "blob" instability west of the "knight's helmet" instability gained momentum and aligned north-south from an east-west orientation. The "knight's helmet" instability continued its development with greater velocities evident at its northern tip, causing further deformation. A drifter vector at the top of the instability pointed more southeasterly than the satellite-derived velocity vectors, but the magnitude was nearly identical. Just to the south of this instability was an imbedded cold core eddy whose cyclonic circulation is shown by the satellite displacement and drifter vectors. With a "tear drop" shape, it is intuitive that the higher velocity vectors creating cyclonic shear are at the wider eastern end of the eddy. Correlation of drifter velocity vectors with satellite-derived velocity vectors was good, especially at the eastern end of the "tear drop" instability. The velocity estimates were of the same order of magnitude.

Finally, the eastern most instability shaped like a "fist" had two satellite-derived vectors to demonstrate the flow along its northern edge. From the limited data available on this instability it appeared to be quasi-stationary compared to the more active features to the west.

From 0845-1335 on 24 October (Figure 49), a dramatic shift in feature displacement occurred as most warm instabilities developed a southerly component of motion. Starting from west to east, the "blob" instability has rapidly developed in less than 24 hours. As indicated on the previous image with only one vector, the instability rotated to a more north-south position. As it matured in the flow, the "blob" showed greater growth potential at its southern portion where vector magnitudes were significantly larger than elsewhere.

The "knight's helmet" instability became too unstable as cold GIN Sea water squeezed it from both sides. Imagery for the rest of the month was unavailable to support the notion that the top half of the instability could eventually be "pinched off", becoming a warm core eddy in the GIN Sea. The cold anomaly just south of this instability increased in size, spreading southwest. This feature appears to be associated with the cold intrusion penetrating the North Atlantic Water between the "knight's helmet" and "fist" instabilities.

The intricacies of frontal flow at small scales were visible on the northern boundary of the "fist" instability. Here, individual vectors illustrate the flow as it moves in and around every wave-like perturbation along the dynamic boundary of the parent instability. Except for the active interface, the instability continued to be quasi-stationary.

Correlation between the drifter and satellite vectors was satisfactory, showing motion in a southerly direction vice easterly as before. Satellite-derived velocity vectors were slightly overestimated in comparison to ground truth.

From 1335-1514 on 24 October (Figure 50), the red and blue colored vectors represent calculations of the same flow field by two operators working independently, portraying qualitative similarity between estimates. The first operator picked 35 points of interest on both images while the second operator picked 40 points. Examining the image from the Icelandic shelf to north of the Færoe Islands, the IFF appeared to become active with high rates of eastward lateral translation.

The "blob" instability continued development and eastward movement while a cold intrusion rapidly filled in behind it. The tip of the "knight's helmet" instability appeared to oppose the flow, but cold water dug into the warm instability gaining velocity as it cyclonically bored through the top of it.

The earlier cold intrusion abated and the residual of a weak warm intrusion shown as a grey area, persisted at approximately 8° W. Overall, the increase in velocity along the entire front was significant with velocities in most areas approaching 100 cm/s. The most spectacular increase in activity was the "fist" instability which went from a dormant and quasi-stationary feature to an extremely dynamic frontal feature.

This image shows a dramatic increase in frontal velocity as depicted by the data gathered by the operators. The correlation between the red and blue arrows is high, with similar magnitudes and directions. However, the limited amount of ground truth magnitude is only a fraction of the ones derived from feature tracking and the direction is more

southerly. When the time difference between images becomes very small (1.65 hours in this case) problems occur due to the limited resolution of the images. Since the pixel size is about 1 km, an error as large as 2km is associated with the displacement. When the time difference is small (e.g., < 6 hours), this error is amplified, and satellite-derived velocity magnitudes are overestimated.

In summary, vector analysis of frontal instabilities and eddies has proven to be a valuable tool for comprehending the magnitude of currents involved in such a dynamically active area. The SST feature tracking method was subjected to review by independent operators working on the same image. Their similar findings (see similar mean values and standard deviations in Table 7), suggest that further subjective analysis by other operators would produce similar results. However, the SST feature tracking for the final image pair overestimated the velocity compared with the in-situ drifter vectors, while the first two image pairs demonstrated good correlation between drifter and feature tracking derived velocities. Even though SST feature tracking appears to be a robust technique for flow field analysis, drifter validation should be used in conjunction. Finally, if ground truth data is unavailable, a time difference from 12 to 24 hours between images would ensure good estimates of surface velocities.

E. SATELLITE SST IMAGES WITH COLOR CODED DRIFTER/SHIP SST OVERLAYS

The technique employed to create these images was similar to Subsection C. The overlaid drifter tracks demonstrate drifter displacements as before, but also change color according to the temperature of the water the drifter is sampling. In this case, the drifter

displacements over an entire day were superimposed on the satellite images. Another difference is the importation of a TeraScan SST grey scale bar and the SST colorbar corresponding to the color coded drifter tracks. Both scales are displayed on the right side of the image. In addition, the color coded lines that predominantly run north-south in a symmetrical pattern are shipboard SST measurements from the NRV *Alliance* as it crisscrossed the IFF. The SST image of the IFF and the color coded tracks were created and overlaid with the development of two MATLAB programs. Black areas represent cloud cover and are discernable from relatively warm (greyer) SST temperatures.

On 19 October 1992 at 1435 UTC (Figure 51), seven drifters and a north-south ship track provided data along the IFF. The ship track clearly defined the frontal boundary as NRV *Alliance* steamed east and then south after taking shelter from high seas in an Icelandic fjord. A fragment of the Icelandic coast is visible in the upper left portion of the image. The frontal discontinuity of approximately 4 °C according to the colorbar is confirmed by examining the satellite SST gray shades with the corresponding scale.

Of the five drifters deployed near the ship crossing of the IFF, two were active and moved eastward rapidly. These two drifters moved eastward along the warm side of the frontal boundary and their trajectories revealed a zonal flow hidden beneath the clouds. The in-situ data showed a distinct frontal boundary underneath the cloud cover masking the middle section of the image. Cloud-free areas confirm the ground truth information. The orientation of the front and the apparent lack of instabilities suggests the IFF was moderately stable on this day. However, a single drifter in the middle of the image showed a cool SST relative to the drifters passing to the north. The SST reading, merely a degree less than the

frontal boundary drifters, was possibly caused by remnants of a cold intrusion earlier in the month that mixed with the NAW or the first signature of the "tear drop" eddy considered later.

On 22 October 1992 at 1359 UTC (Figure 52), cloud masking covered the eastern half of the image where the drifter and ship tracks were collocated. Four drifters west of 12° W moved to the southeast through warm pockets of water dispersed within an area of cooler NAW. The drifter and ship data under the cloud cover described a more complex IFF, with anomalous SST measurements on both sides of an active front.

Curvature of drifter trajectories are also indicative of an unstable frontal boundary. As instabilities and eddies develop in a baroclinically unstable environment, zonal flow becomes distorted. Drifters launched at approximately 10° W near the eastern end of the ship track, outline the beginning of a warm instability which became the most spectacular feature during the following days. Again, the surface temperature difference across the IFF is approximately 4 °C.

The longest north-south ship track alternated in color frequently as the ship temperature sensors passed through warm and cold SST's. Perpendicular to the IFF, this swath is representative of an active frontal boundary with warm (cold) intrusions north (south) of the IFF. Allowing for some temporal variability, drifter and ship SST measurements in the area showed excellent correlation.

On 23 October 1992 at 1528 UTC (Figure 53), cloud coverage was less extensive enabling good analysis of SST features with both the satellite and drifter data. The "knight's helmet" instability, introduced in Subsection C, is clearly visible at 64° N and 10° W. Drifter

displacement around the instability showed the anticyclonic rotation and further defined the eddy with warm core temperature measurements. Along the eastern side of the eddy, drifter and ship SST readings defined a warm filament under its rotational influence. Due to the filaments proximity and association to the parent eddy, formation was likely caused by shear vorticity and mixing along the rotating warm water. Because of the active mixing along the eddy boundary, the temperature discontinuity was only 1-2 °C.

South of the "knight's helmet" instability was a cold eddy previously identified as having a "tear drop" shape. The drifter showed the cyclonic rotation and relatively cool SST measurement indicative of a cold core eddy. A warm drifter trajectory overlapped the initial position of the previous eddy-bound drifter several hours later, showing an eastward translation of the eddy as it spun counterclockwise.

North of the "knight's helmet" instability, the color coded ship track described a water mass with uniform cold temperature characteristics. However, the ship's thermistor recorded a warm anomaly north of the "knight's helmet" instability that correlates well with a drifter measurement to the west of this temperature reading. Apparently, the region north of the eddy consisted of anomalous pockets of warm water that broke free from the rotating instability.

On 24 October 1992 at 1514 UTC (Figure 54), the "knight's helmet" and "blob" instabilities were nearly clear of clouds. Five drifters surrounding the northern portion of the "knight's helmet" instability displayed a blue shade corresponding to SST of approximately 4 °C. The northern most drifter on the image exhibited a slightly warmer SST in waters appearing to have originated from the instability, or to be a remnant of a previous

warm intrusion. As the instability rotated clockwise and translated eastward, warm water was eroded away by the colder, denser GIN Sea waters through shear generated vorticity. The warm plume of water north of the instability was the result of ongoing eddy destruction. Again, the circulation and temperature characteristics of the "knight's helmet" and "tear drop" instabilities were made apparent by the color coded tracks. Between the "blob" and "knight's helmet" instabilities was a single 'blue' drifter which revealed a clockwise thrust of cold water around the "blob", an apparent attempt to close on itself.

On the eastern limits of the image, the ship track revealed a warm intrusion with warmest values recorded in its northernmost area. The subtle differences between northern and southern SSTs within the intrusion were resolved by the ship sensor. The weak temperature gradient along the intrusion's boundary indicated active mixing with the colder GIN Sea water.

Instabilities develop, become unstable and then are destroyed by shear and mixing. Figure 54 is an excellent representation of these stages in the life of an instability. The cohesive and relatively symmetrical "blob" represents the developmental stage while the "knight's helmet" has reached maturity and has undergone some deformation and destruction. Finally, the intrusion east of these instabilities was probably a well-defined SST feature before dense GIN Sea water broke its continuity and mixed through it.

16 OCT 92 - 25 SEPT 93

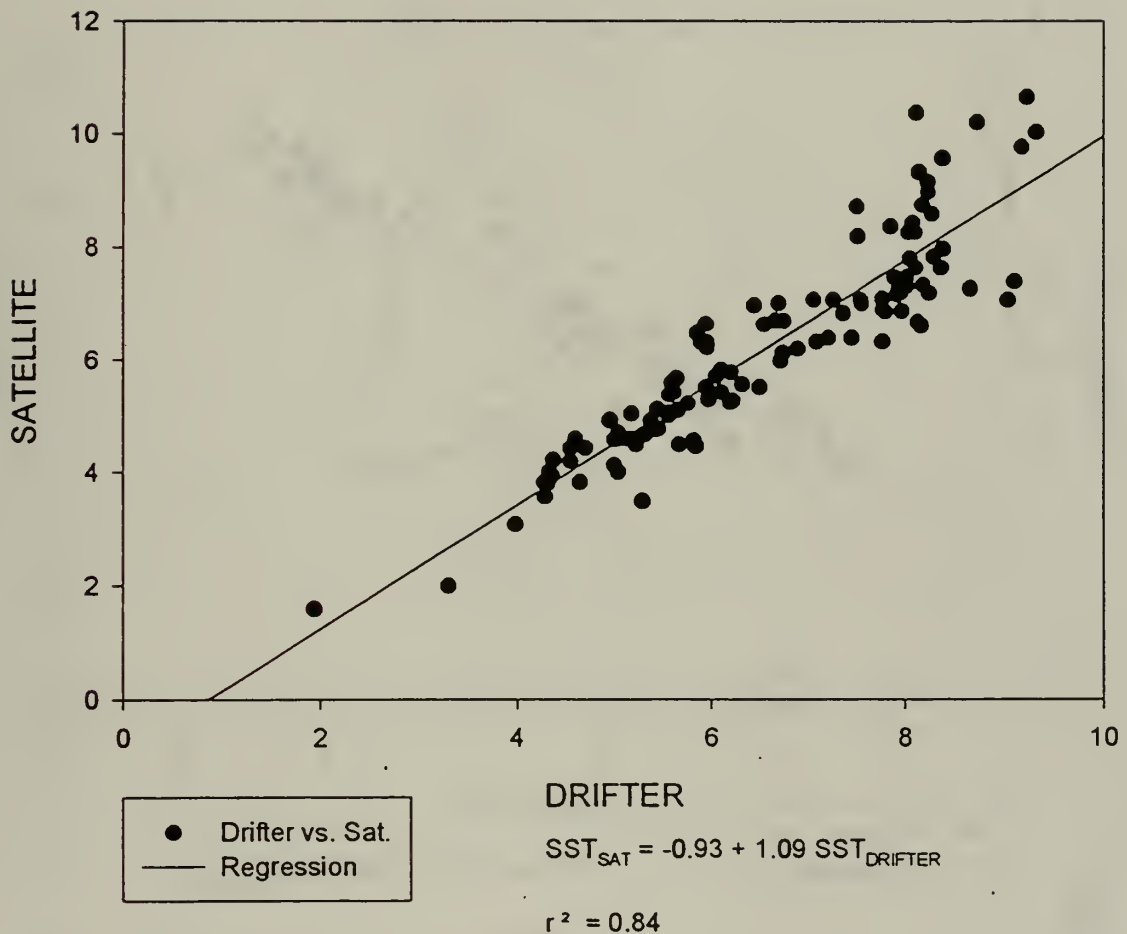


Figure 17. Regression Analysis of Coincident Drifter and Satellite Retrieved SSTs from October 1992 to September 1993, which Includes GIN92 and GIN93.

16 - 24 OCT 92

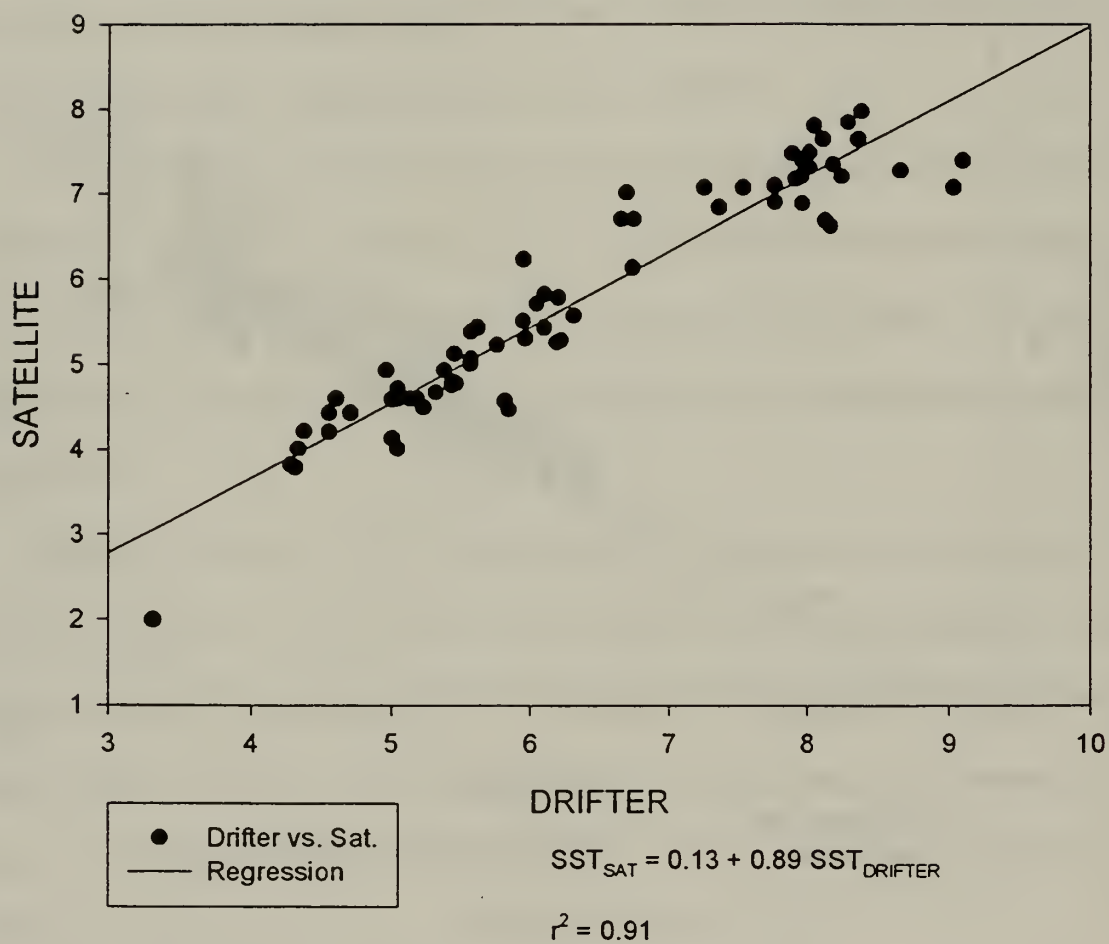


Figure 18. Regression Analysis of Coincident Drifter and Satellite Retrieved SSTs for GIN92.

LAGRANGIAN DRIFTER TRACKS FOR AUGUST 1992

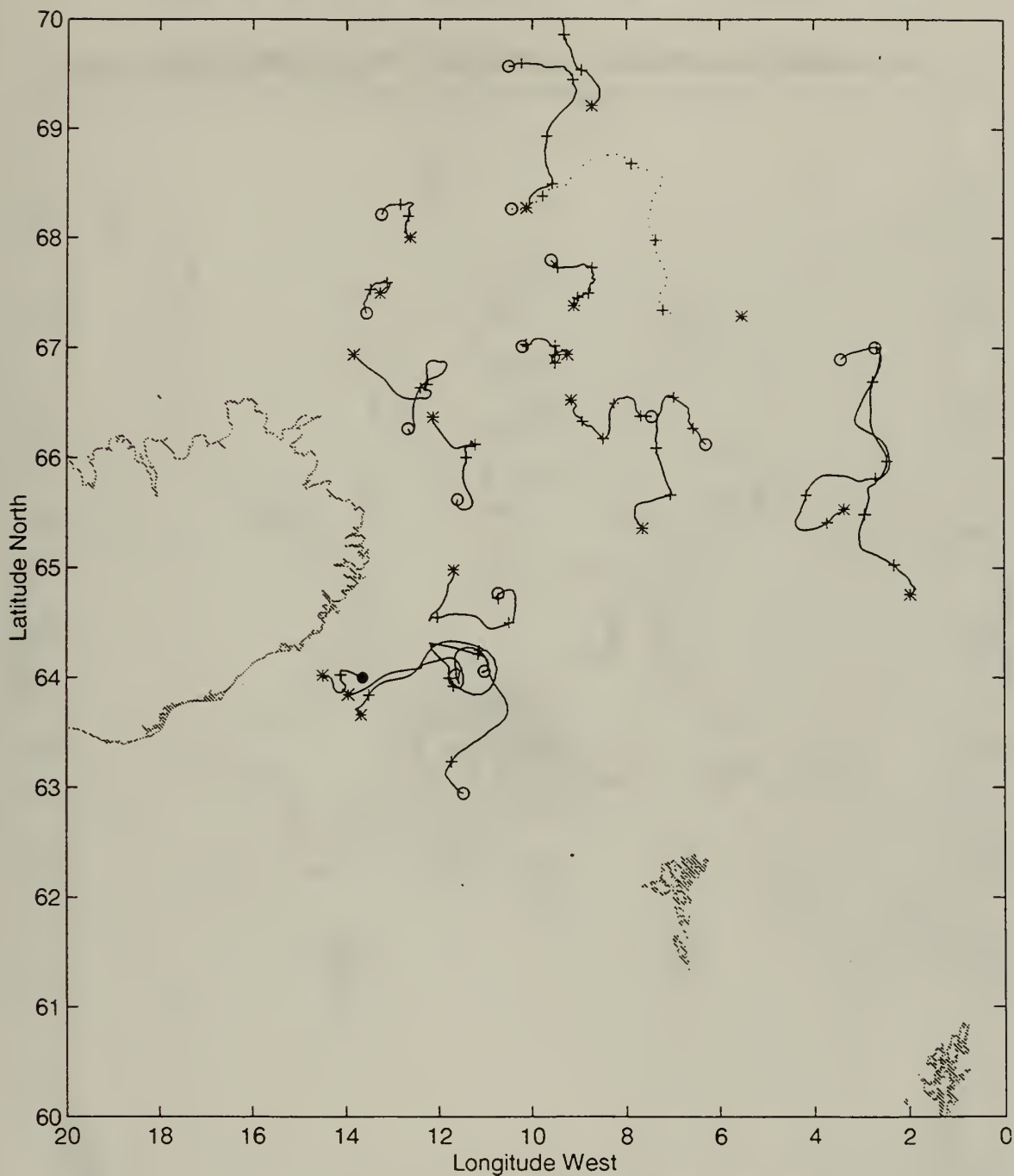


Figure 19. Drifter Trajectory Segments for August 1992. Star symbols indicate deployment sites or the drifter location at the beginning of the month. Circles are drawn at the location of last transmission (solid circle) or at the drifter location at the end of the month (open circle).

LAGRANGIAN DRIFTER TRACKS FOR SEPTEMBER 1992

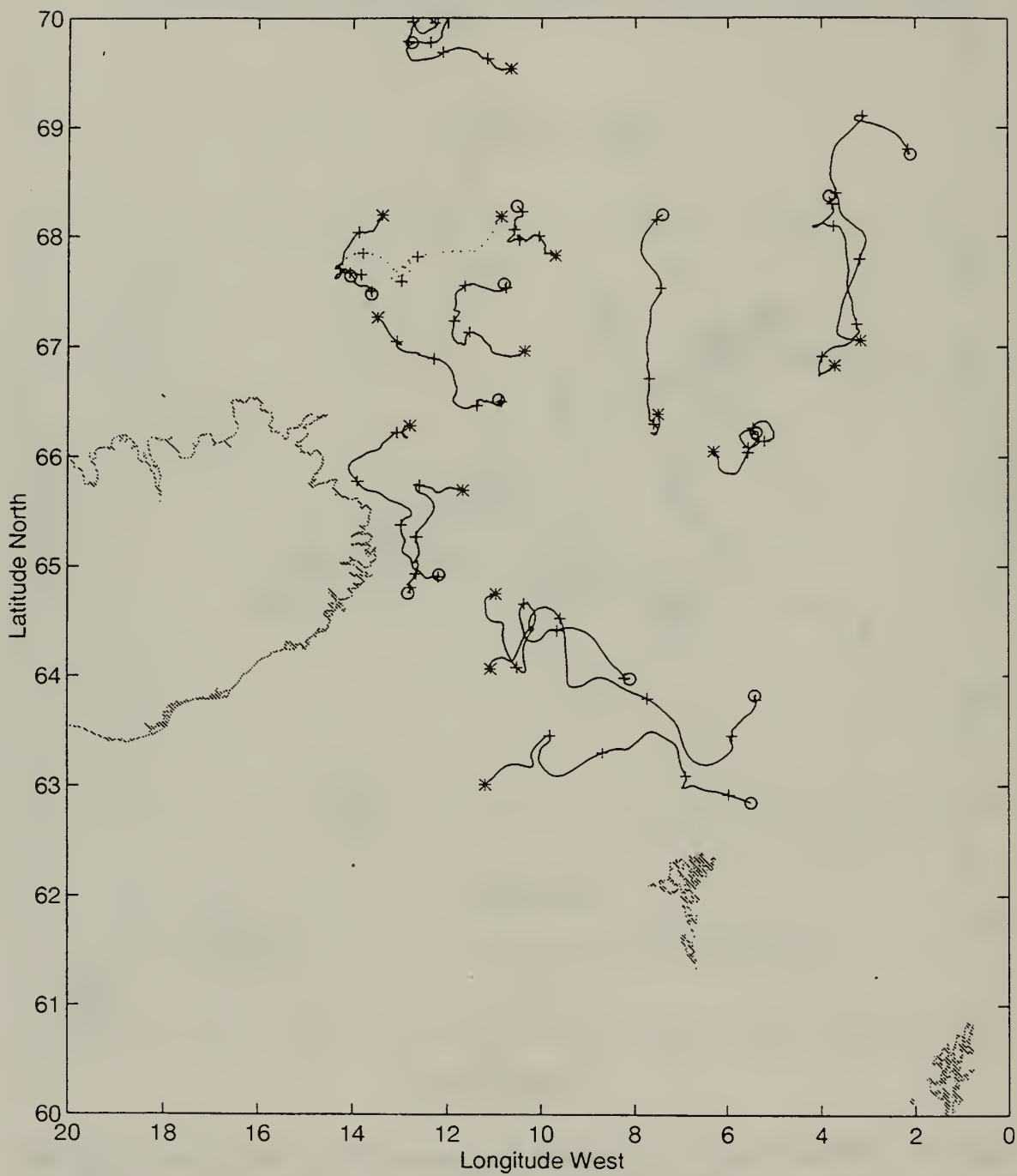


Figure 20. Same as Figure 19 for September 1992.

LAGRANGIAN DRIFTER TRACKS FOR OCTOBER 1992

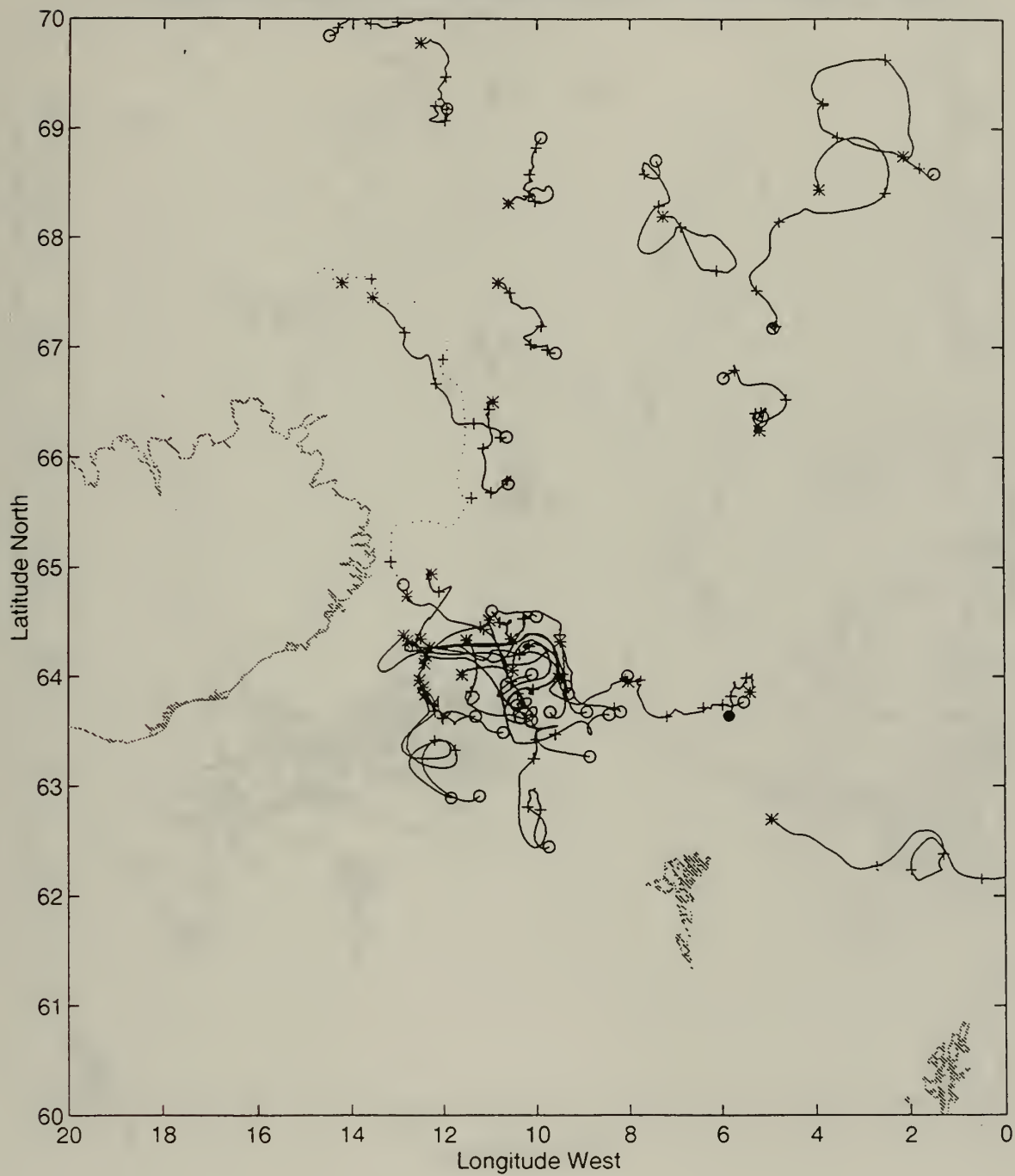


Figure 21. Same as Figure 19 for October 1992.

82

LAGRANGIAN DRIFTER TRACKS FOR DECEMBER 1992

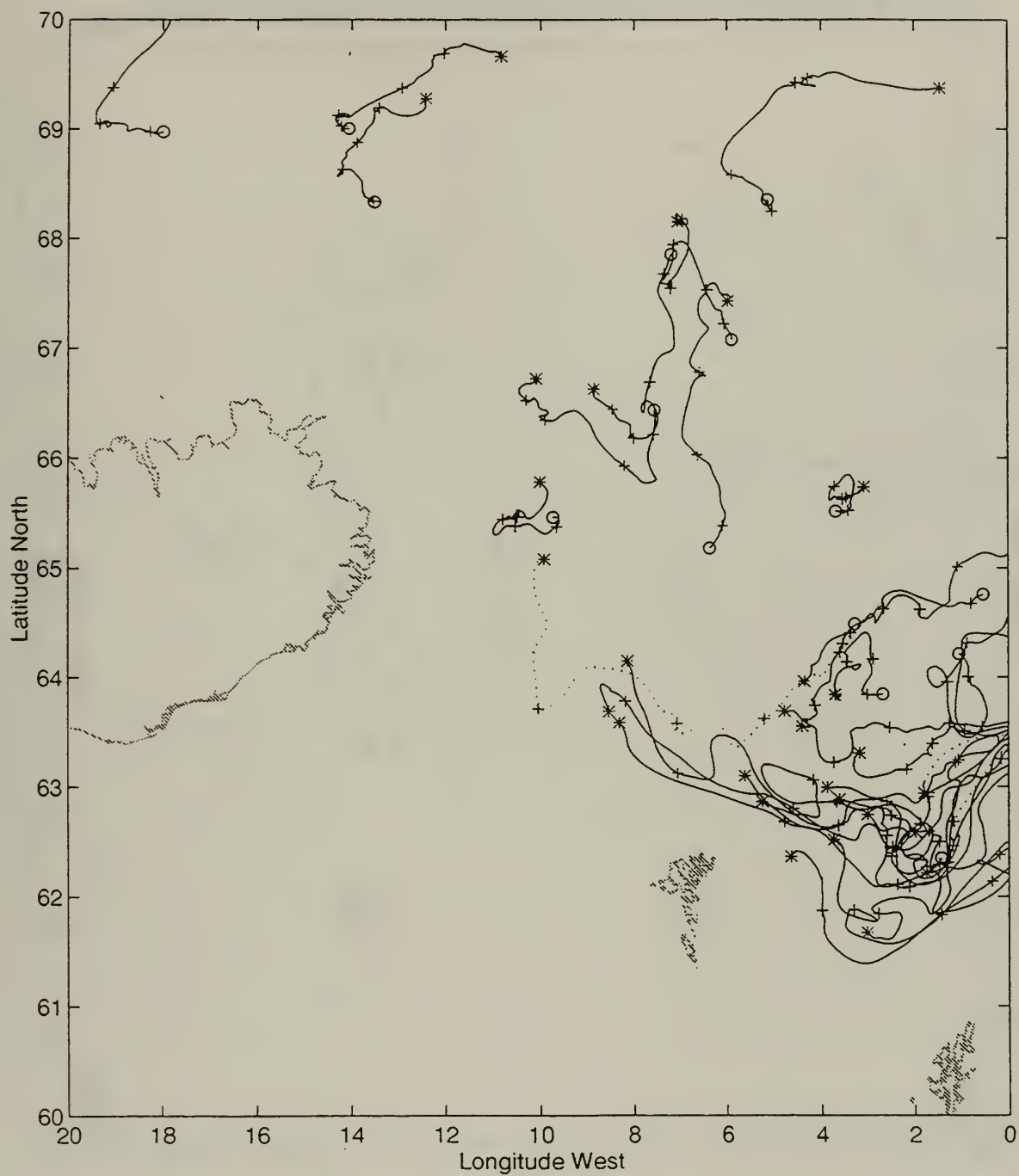


Figure 23. Same as Figure 19 for December 1992.

LAGRANGIAN DRIFTER TRACKS FOR JANUARY 1993

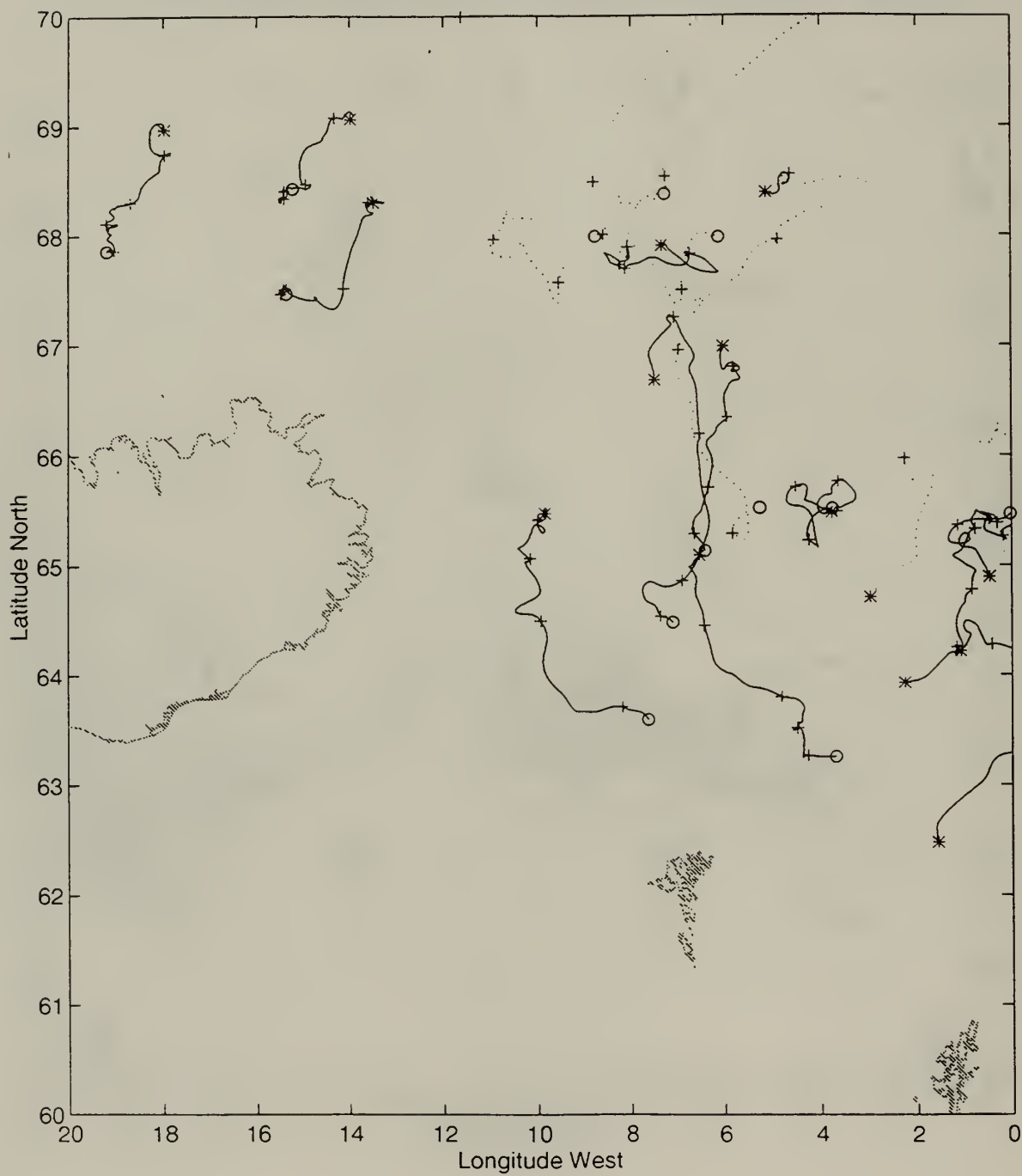


Figure 24. Same as Figure 19 for January 1993.

LAGRANGIAN DRIFTER TRACKS FOR FEBRUARY 1993

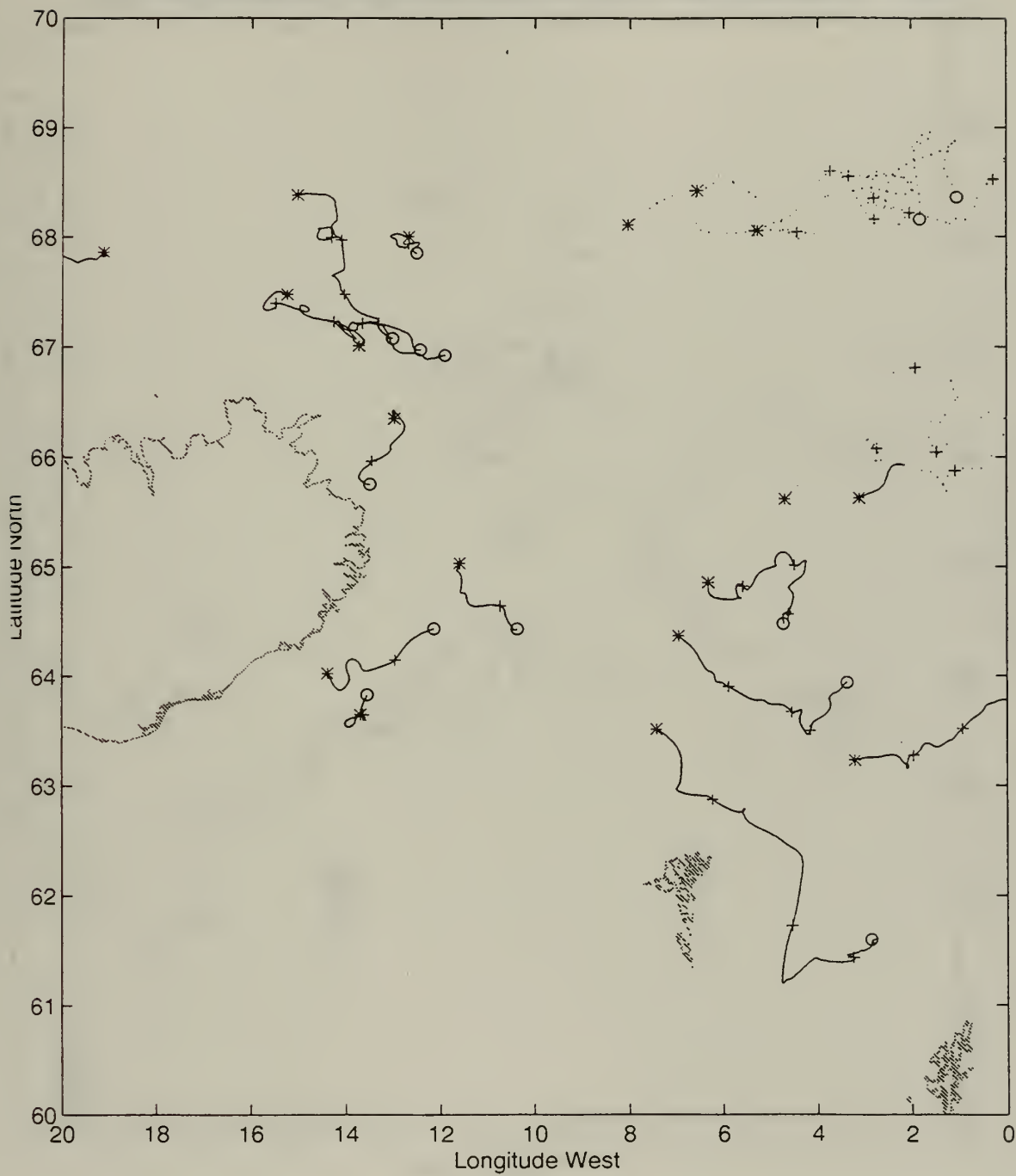


Figure 25. Same as Figure 19 for February 1993.

LAGRANGIAN DRIFTER TRACKS FOR MARCH 1993

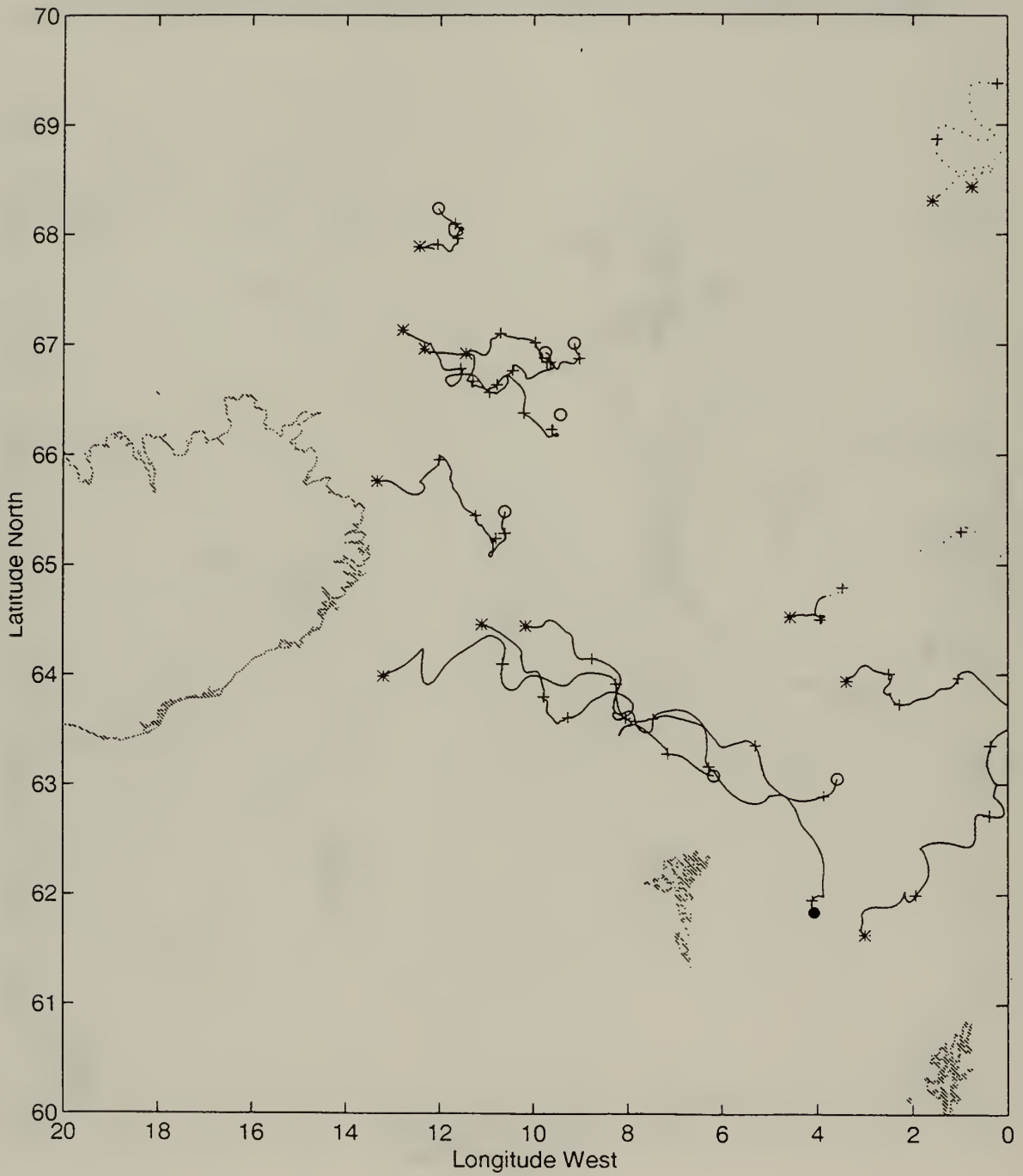


Figure 26. Same as Figure 19 for March 1993.

LAGRANGIAN DRIFTER TRACKS FOR APRIL 1993

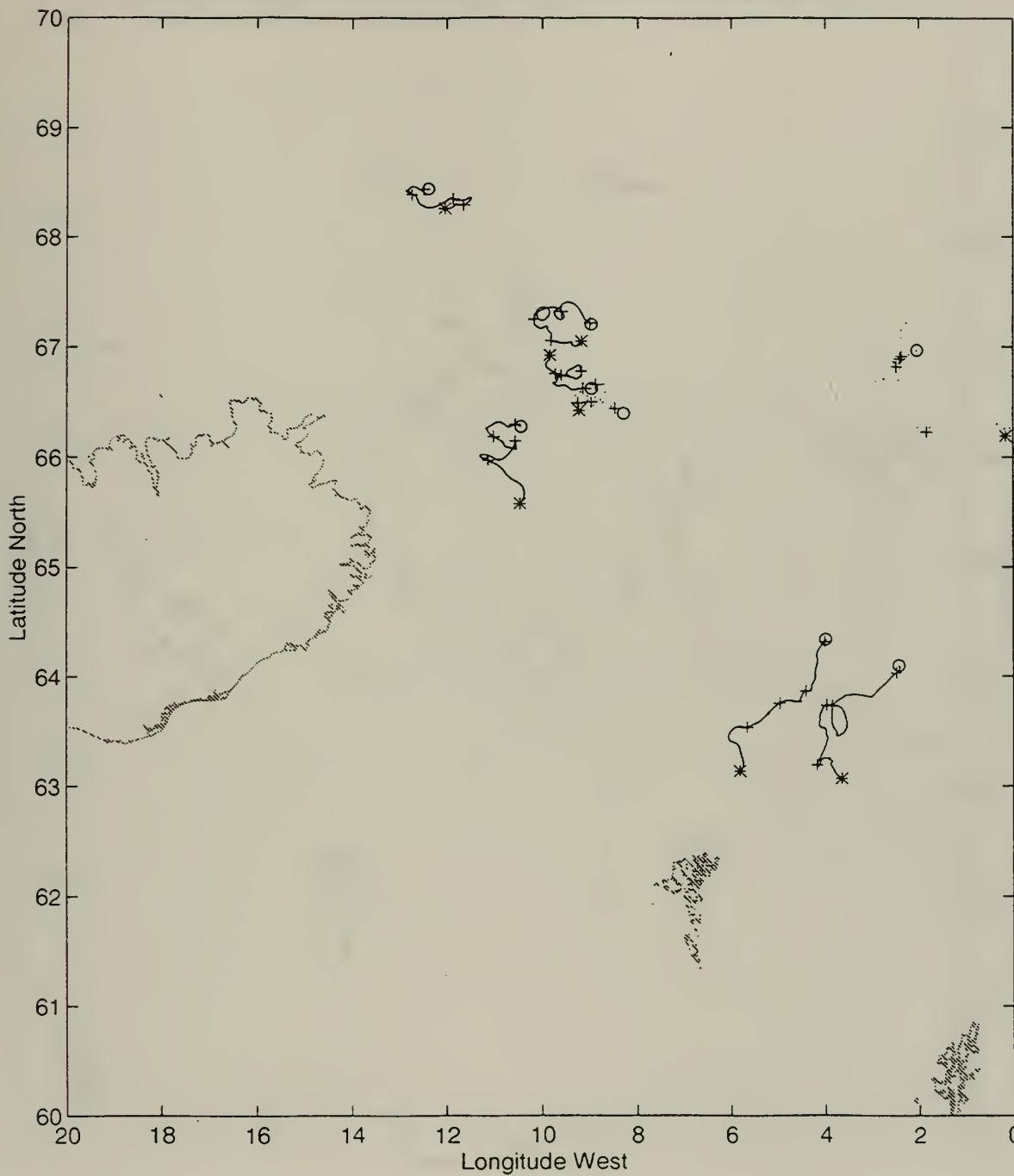


Figure 27. Same as Figure 19 for April 1993.

LAGRANGIAN DRIFTER TRACKS FOR MAY 1993

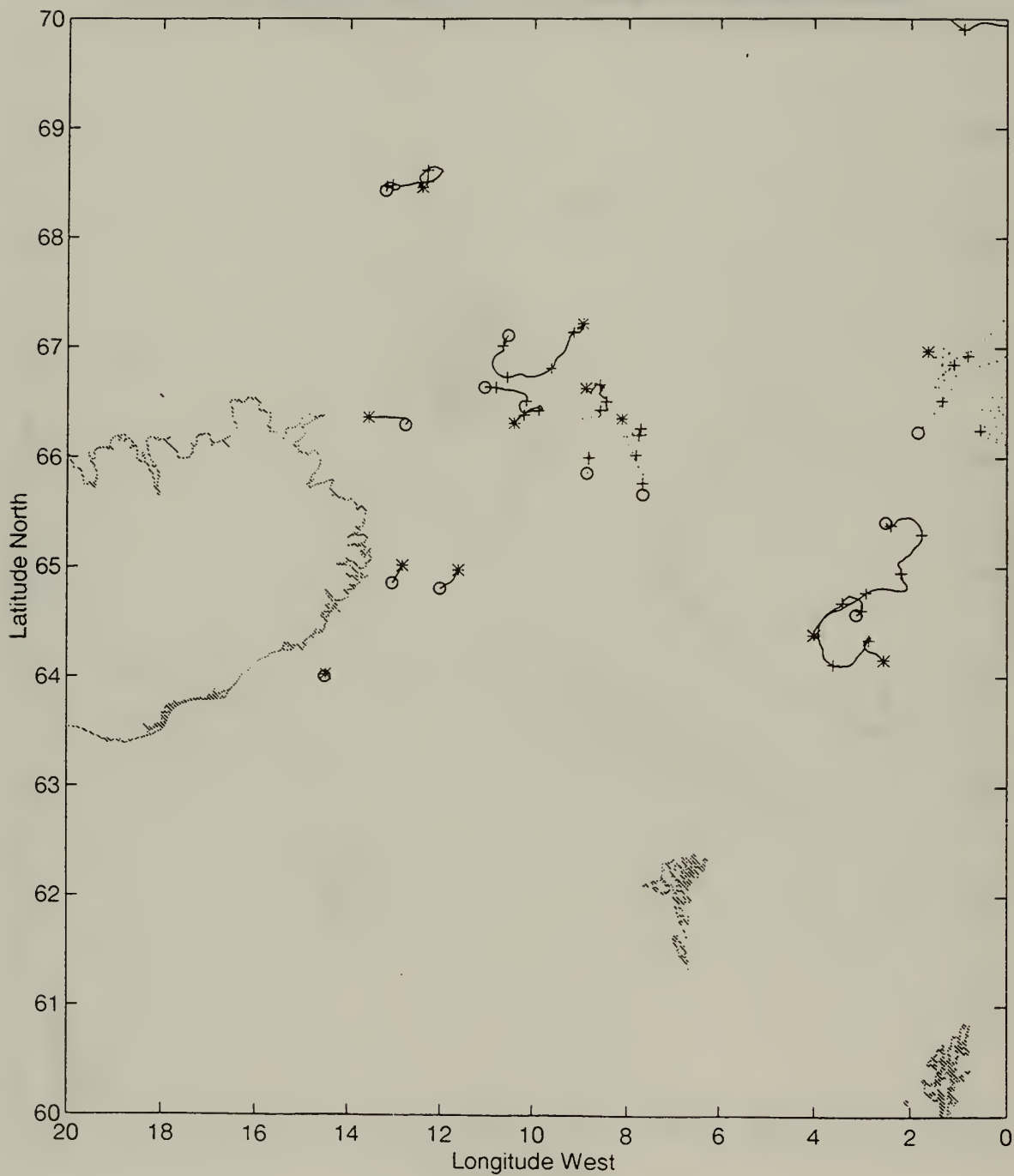


Figure 28. Same as Figure 19 for May 1993.

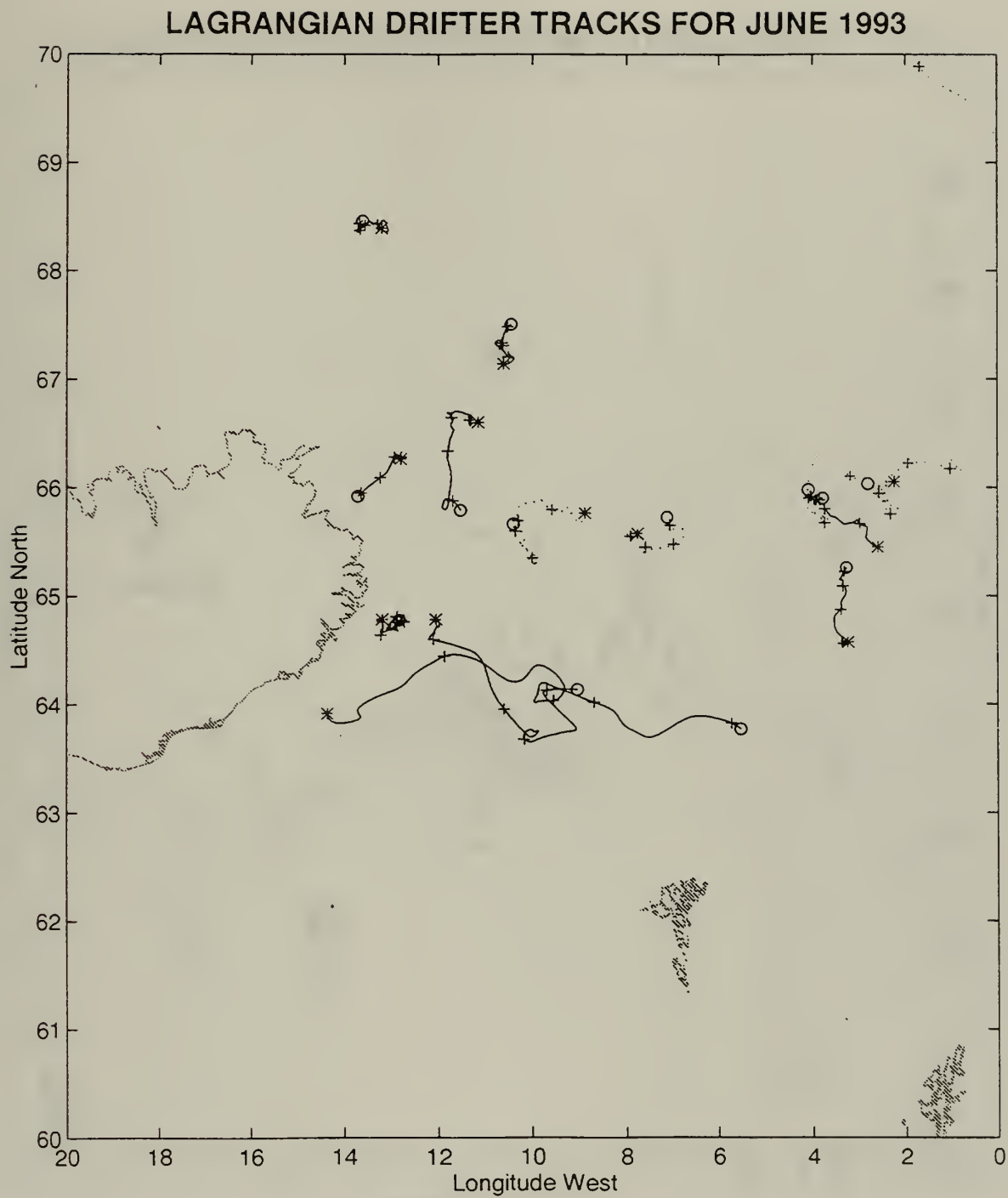


Figure 29. Same as Figure 19 for June 1993.

LAGRANGIAN DRIFTER TRACKS FOR JULY 1993

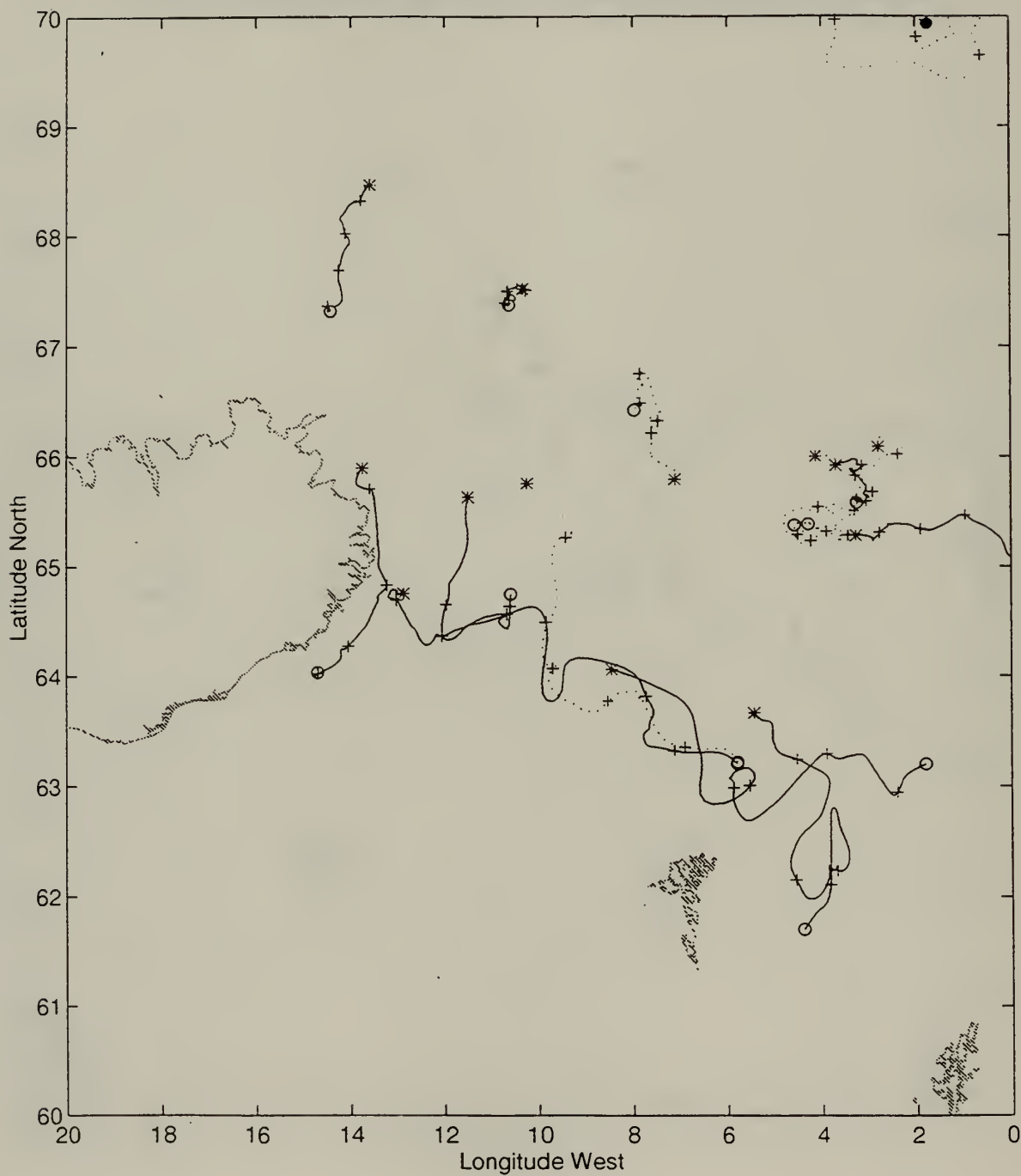


Figure 30. Same as Figure 19 for July 1993.

LAGRANGIAN DRIFTER TRACKS FOR AUGUST 1993

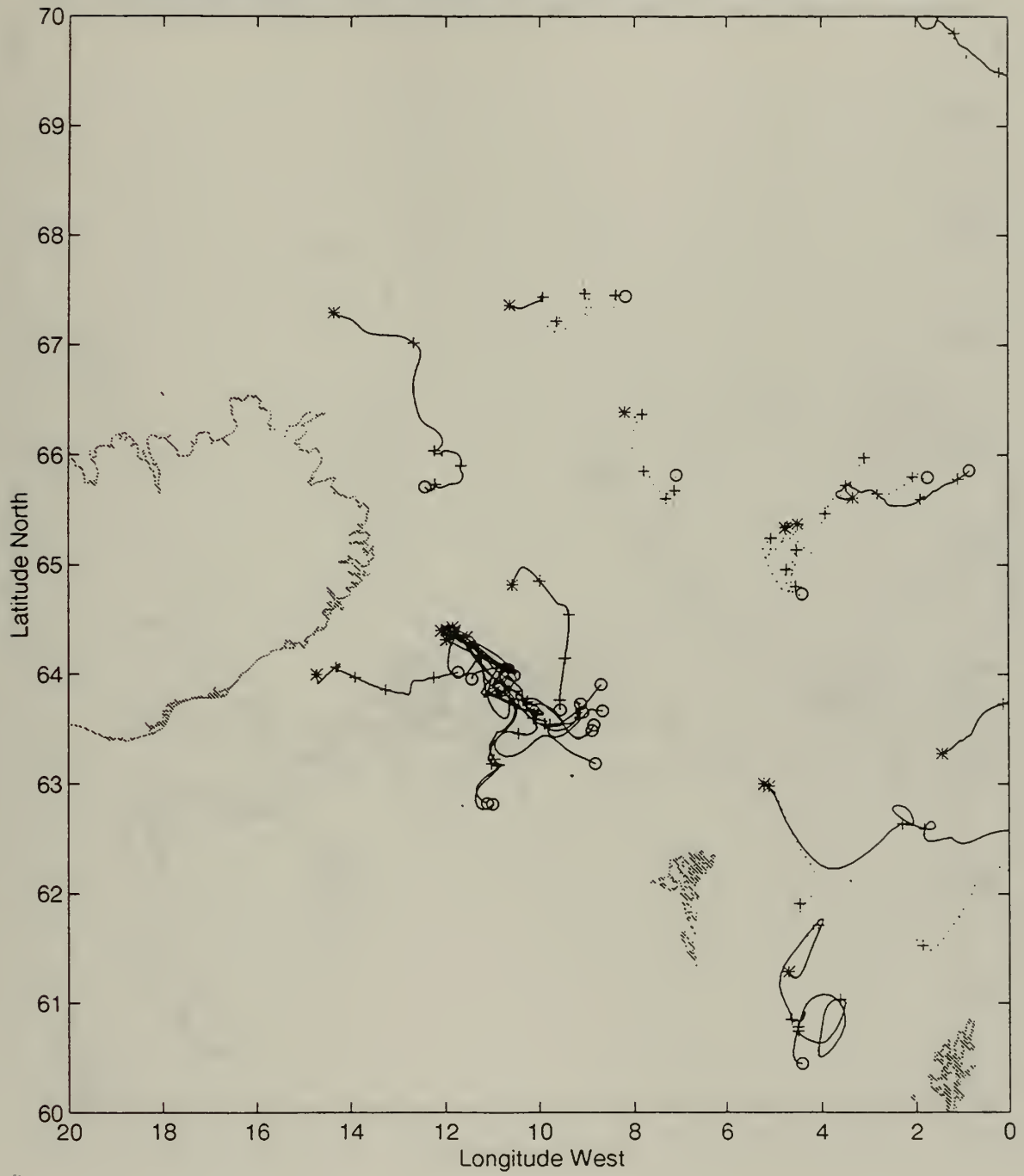


Figure 31. Same as Figure 19 for August 1993.

LAGRANGIAN DRIFTER TRACKS FOR SEPTEMBER 1993

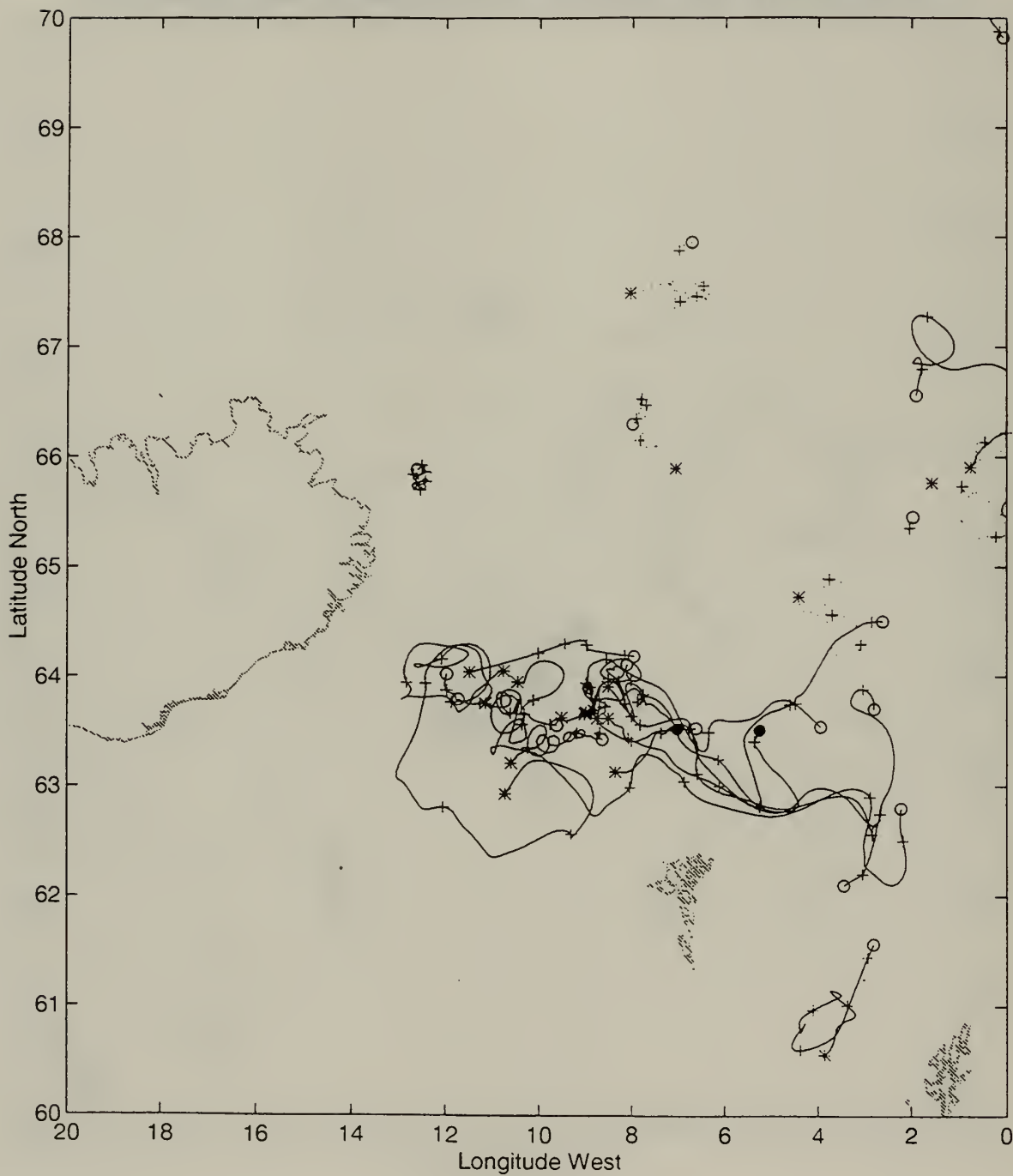


Figure 32. Same as Figure 19 for September 1993.

LAGRANGIAN DRIFTER TRACKS FOR OCTOBER 1993

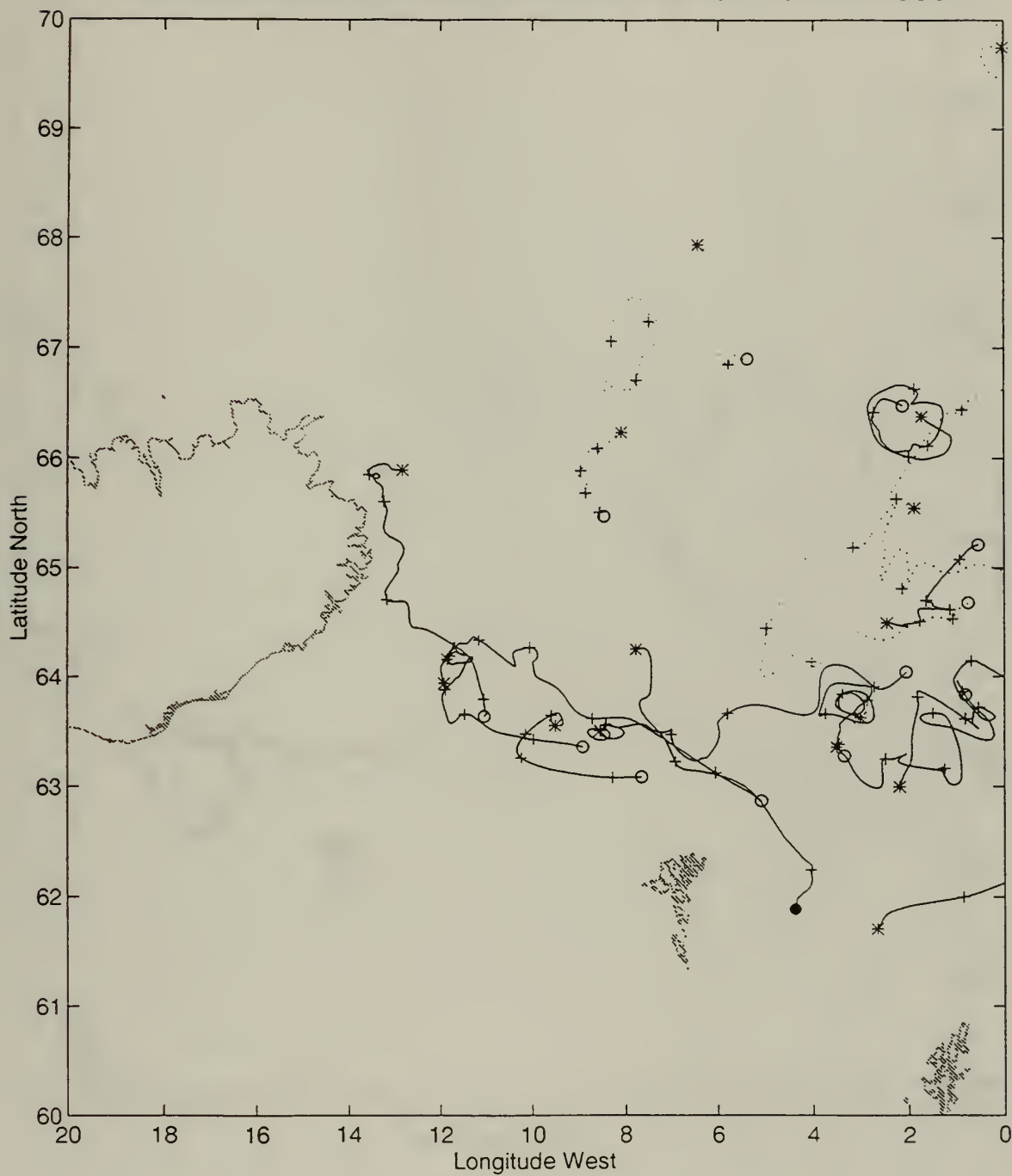


Figure 33. Same as Figure 19 for October 1993.

LAGRANGIAN DRIFTER TRACKS FOR NOVEMBER 1993

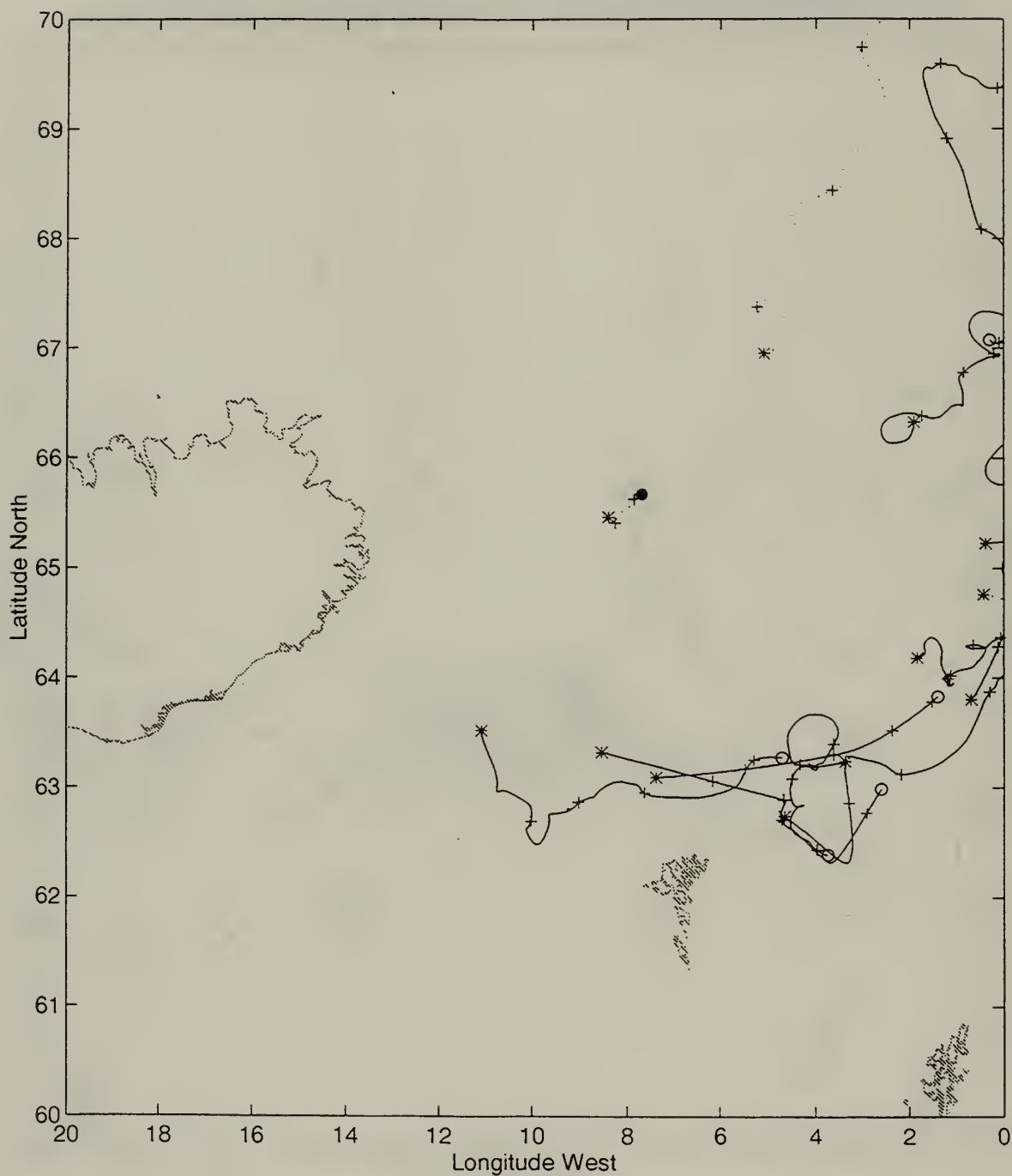


Figure 34. Same as Figure 19 for November 1993.

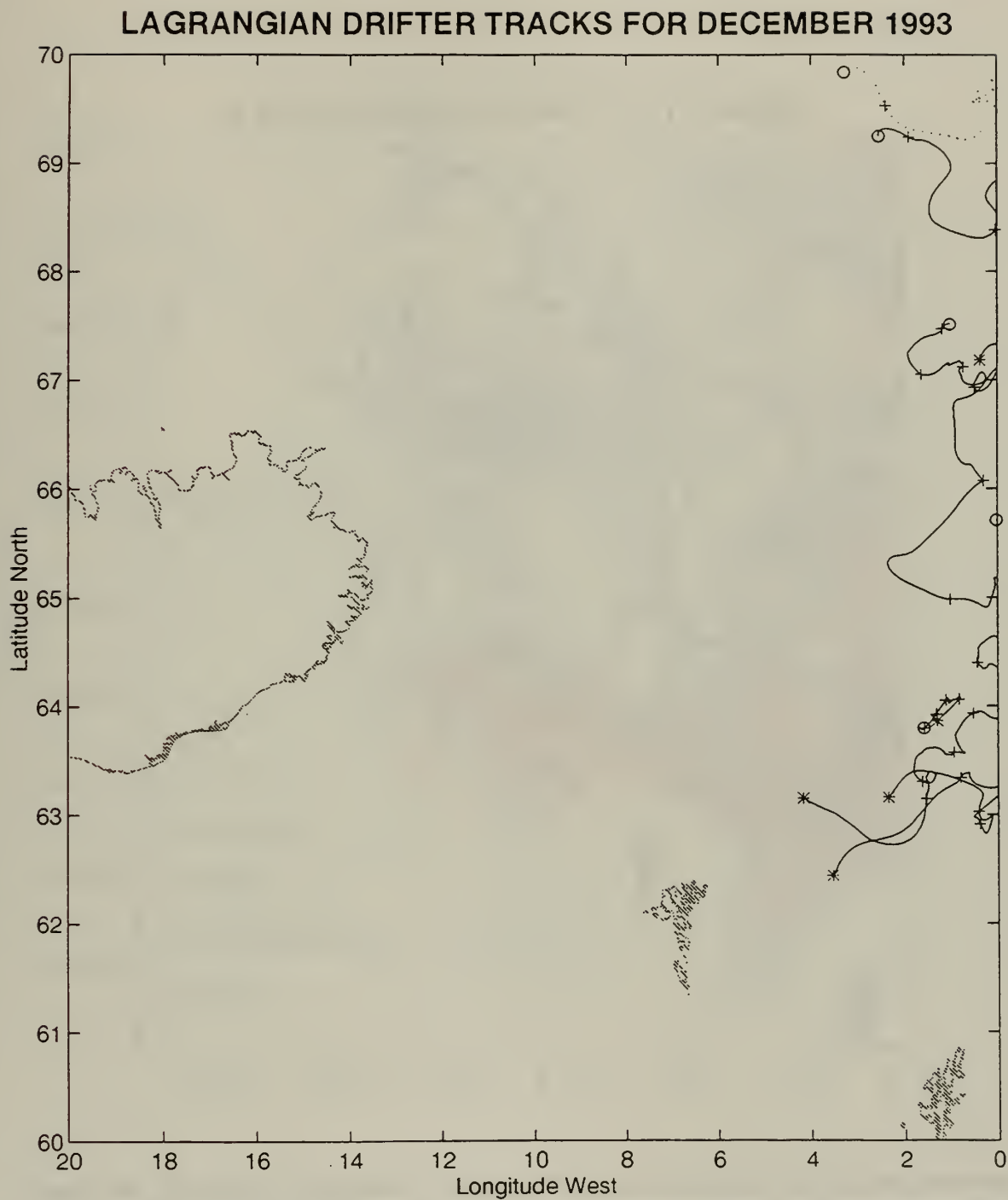


Figure 35. Same as Figure 19 for December 1993.

LAGRANGIAN DRIFTER TRACKS

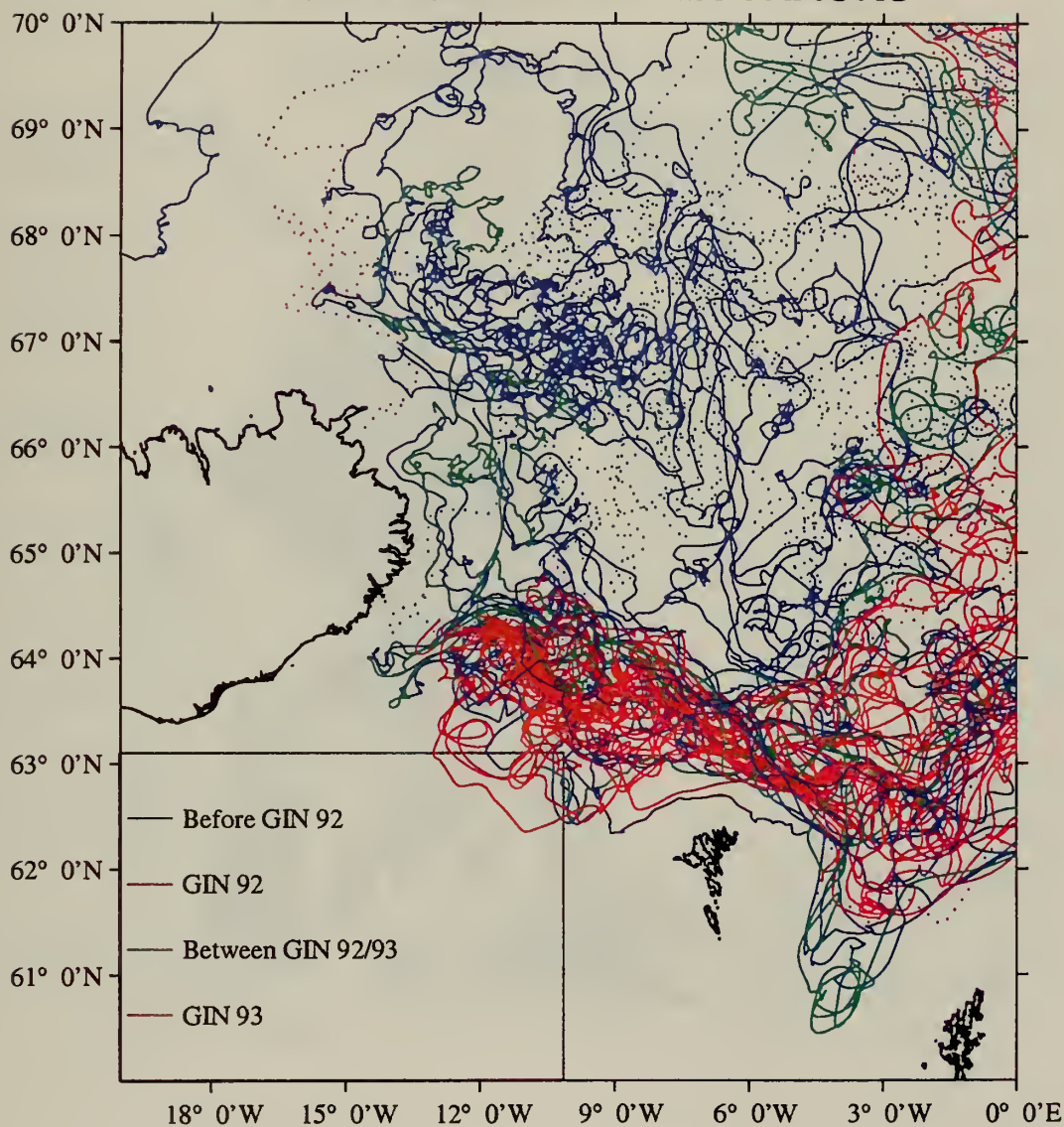


Figure 36. Composite "Spaghetti" Diagram Showing all the Drifter Tracks Between August 1992 and December 1993. The tracks are color-coded with respect to the deployment dates, i.e., blue (before GIN92), magenta (GIN92), green (between GIN92 and GIN93), and orange (GIN93). Dotted lines represent the tracks of un-drogued drifters.

16 OCTOBER 92: 1512 UTC

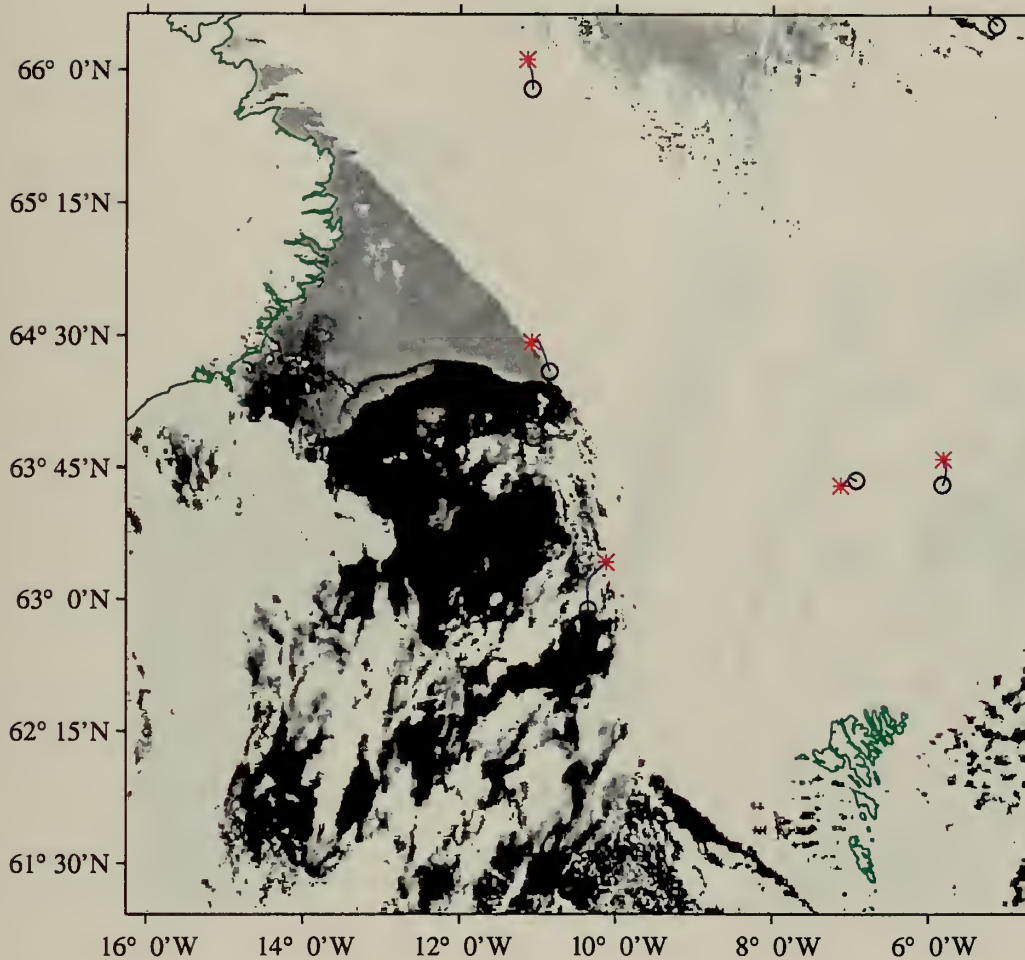


Figure 37. MCSST Image of the IFR Region on 16 October 1992 at 1512 UTC. Light (dark) gray shades correspond to relatively cold (warm) sea surface temperatures. Cloud-covered pixels are shown in white. Superimposed drifter displacements begin the day before the image and end the day after. Star (circle) symbols denote the drifter location at the beginning (end) of the day.

19 OCTOBER 92: 1435 UTC

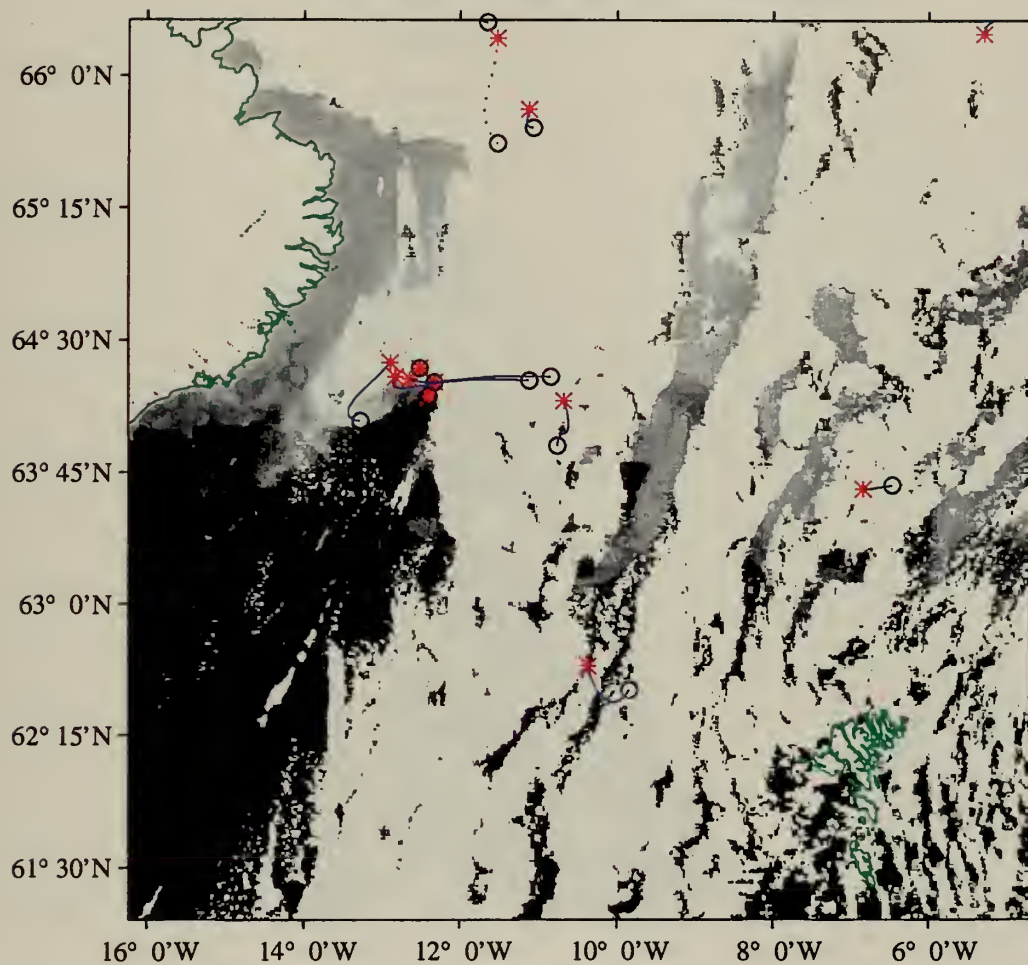


Figure 38. Same as Figure 37 for 19 October 1992 at 1435 UTC.

22 OCTOBER 92: 1359 UTC

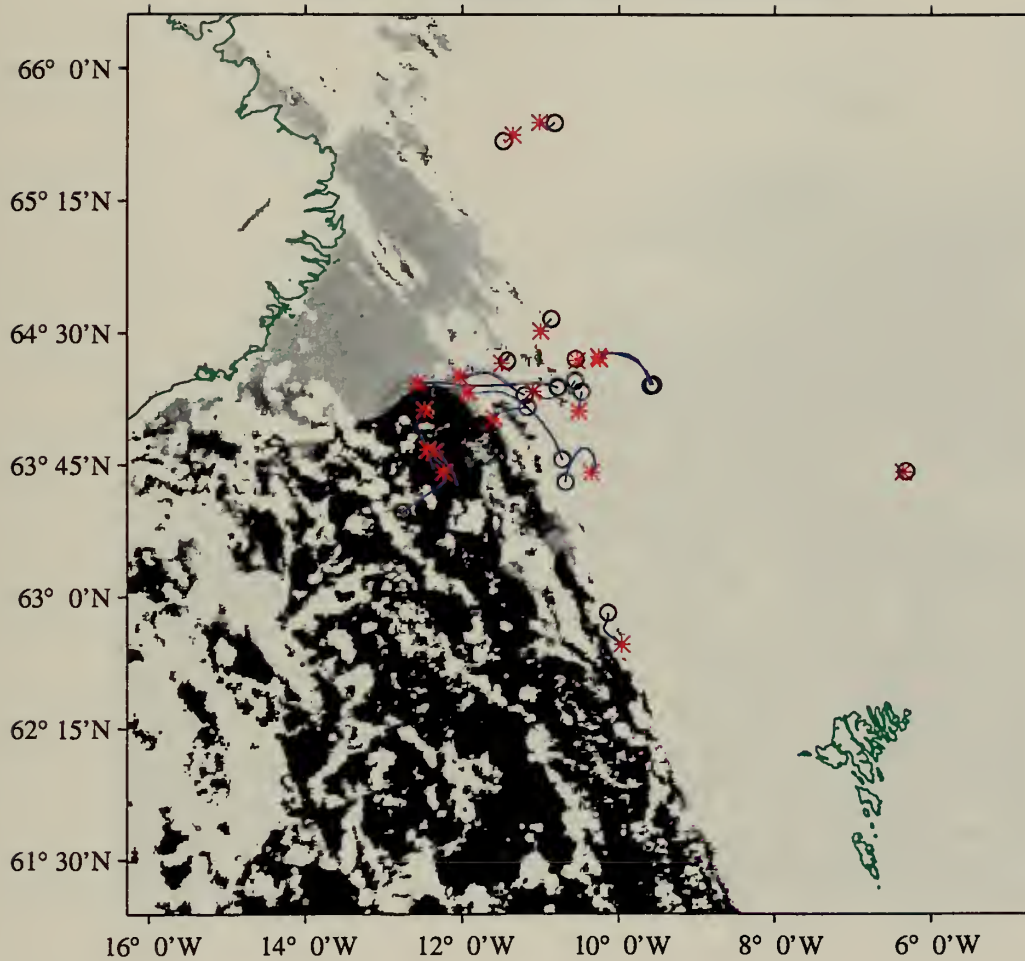


Figure 39. Same as Figure 37 for 22 October 1992 at 1359 UTC.

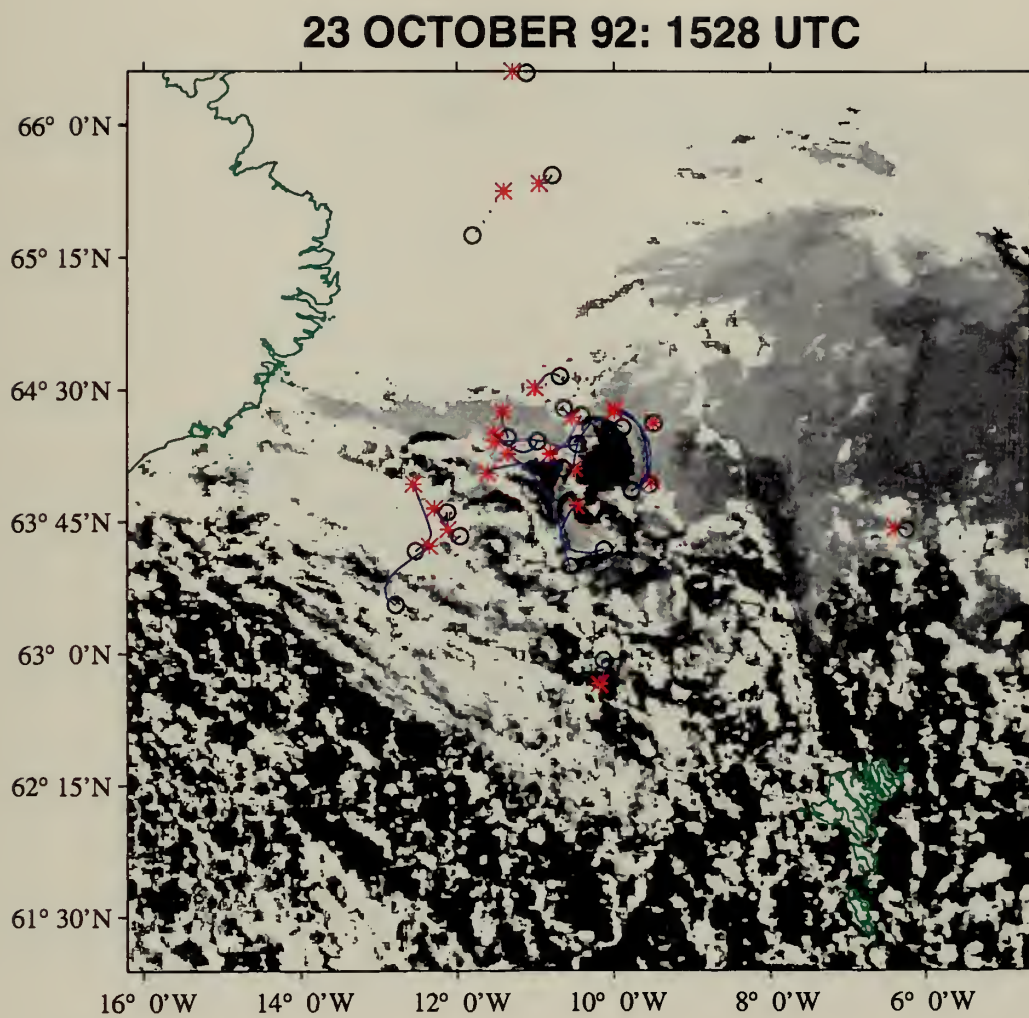


Figure 40. Same as Figure 37 for 23 October 1992 at 1528 UTC.

24 OCTOBER 92: 0845 UTC

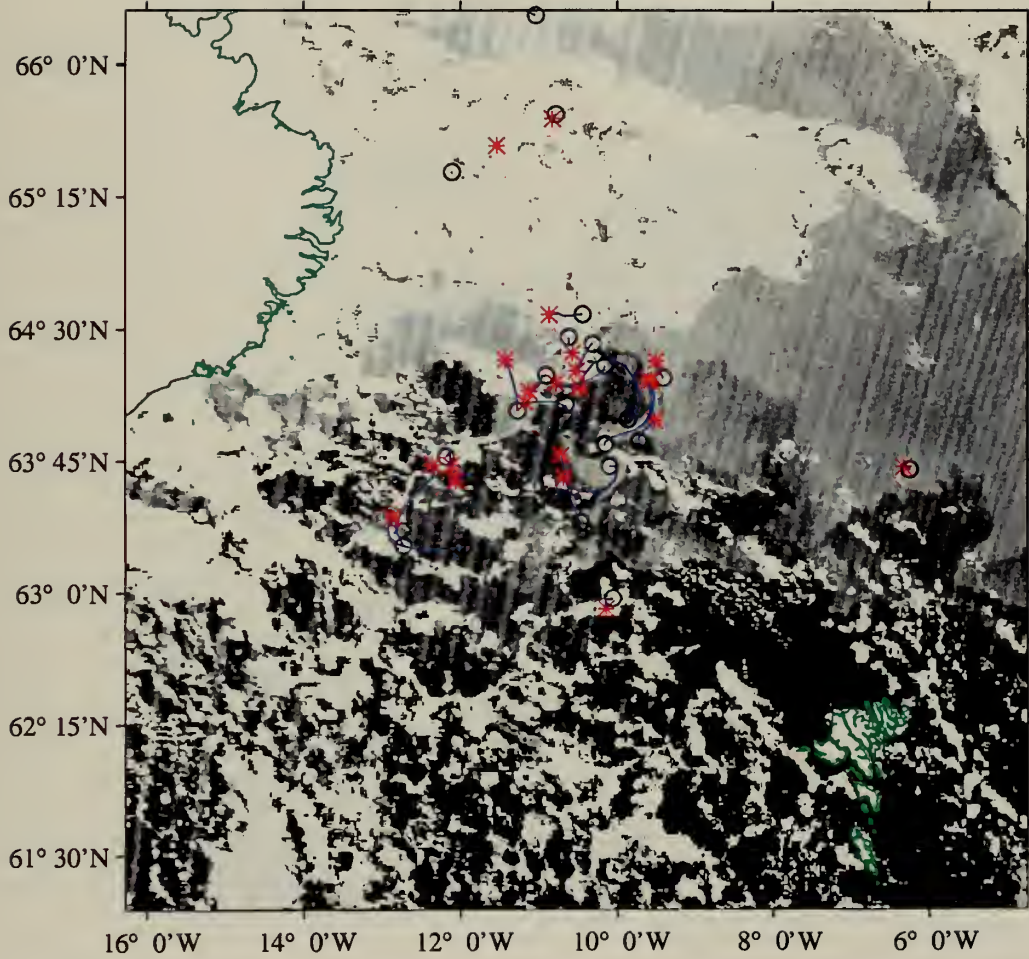


Figure 41. Same as Figure 37 for 24 October 1992 at 0845 UTC.

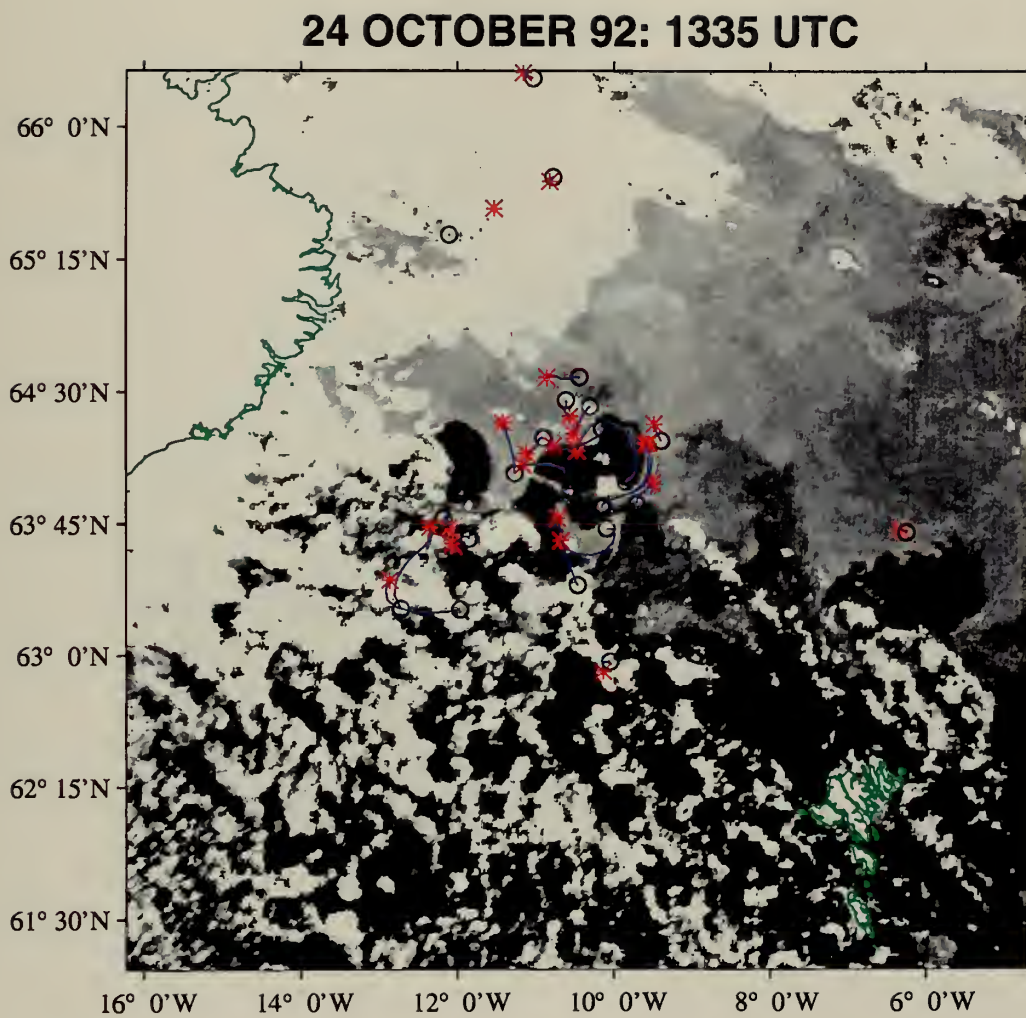


Figure 42. Same as Figure 37 for 24 October 1992 at 1335 UTC.

24 OCTOBER 92: 1514 UTC

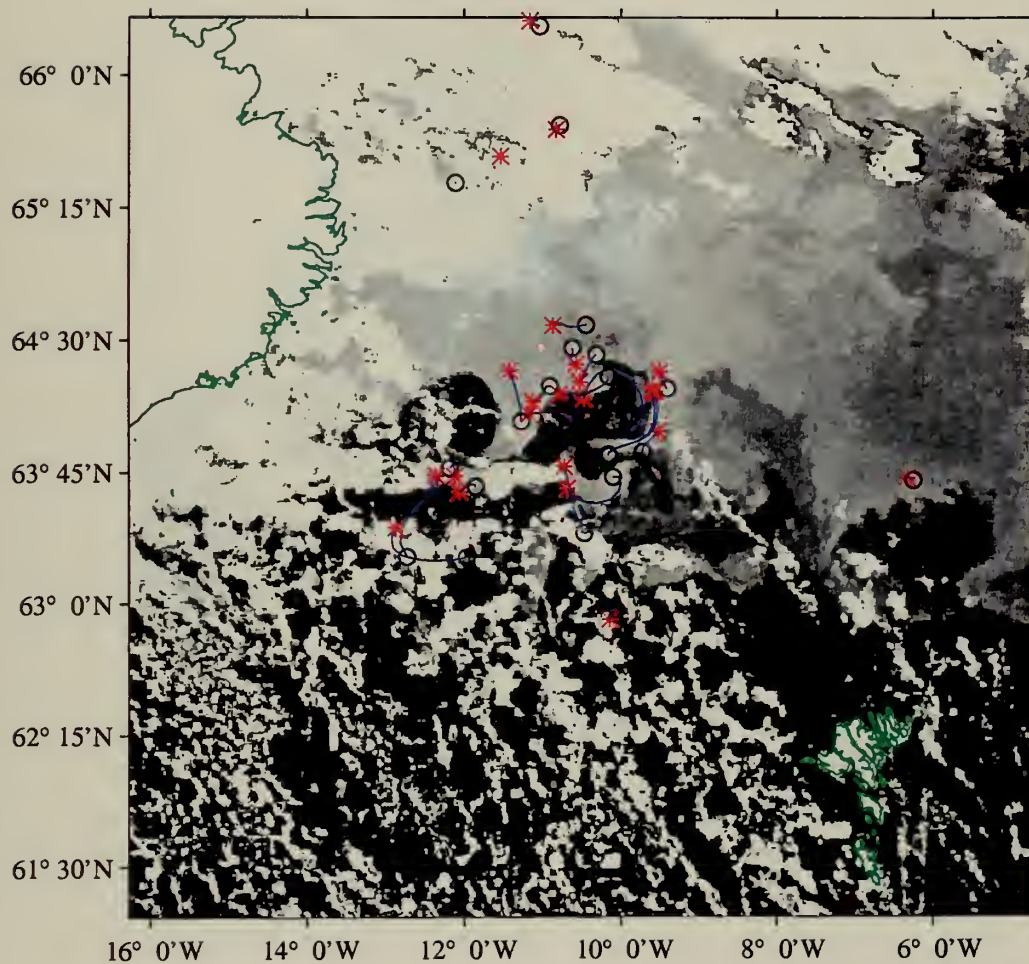


Figure 43. Same as Figure 37 for 24 October 1992 at 1514 UTC.

17 NOVEMBER 92: 1347 UTC

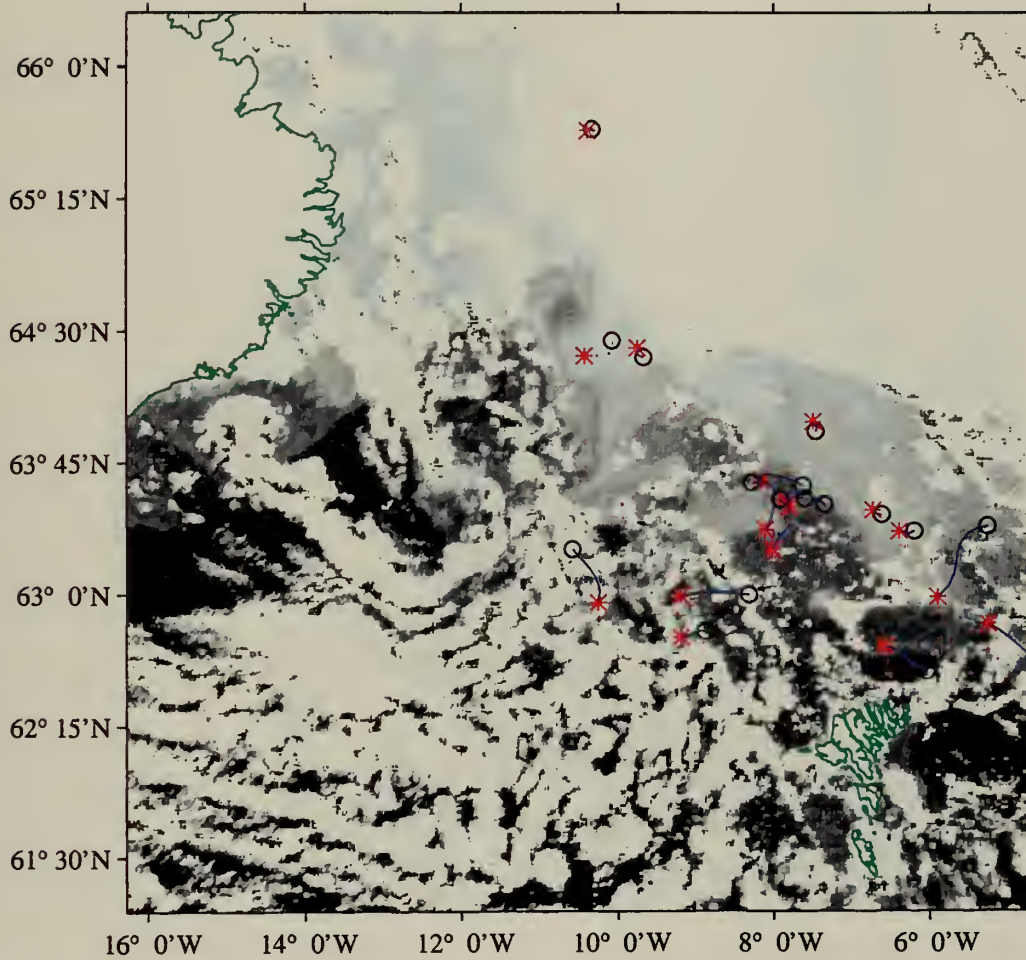


Figure 44. Same as Figure 37 for 17 November 1992 at 1347 UTC.

25 DECEMBER 92: 1432 UTC

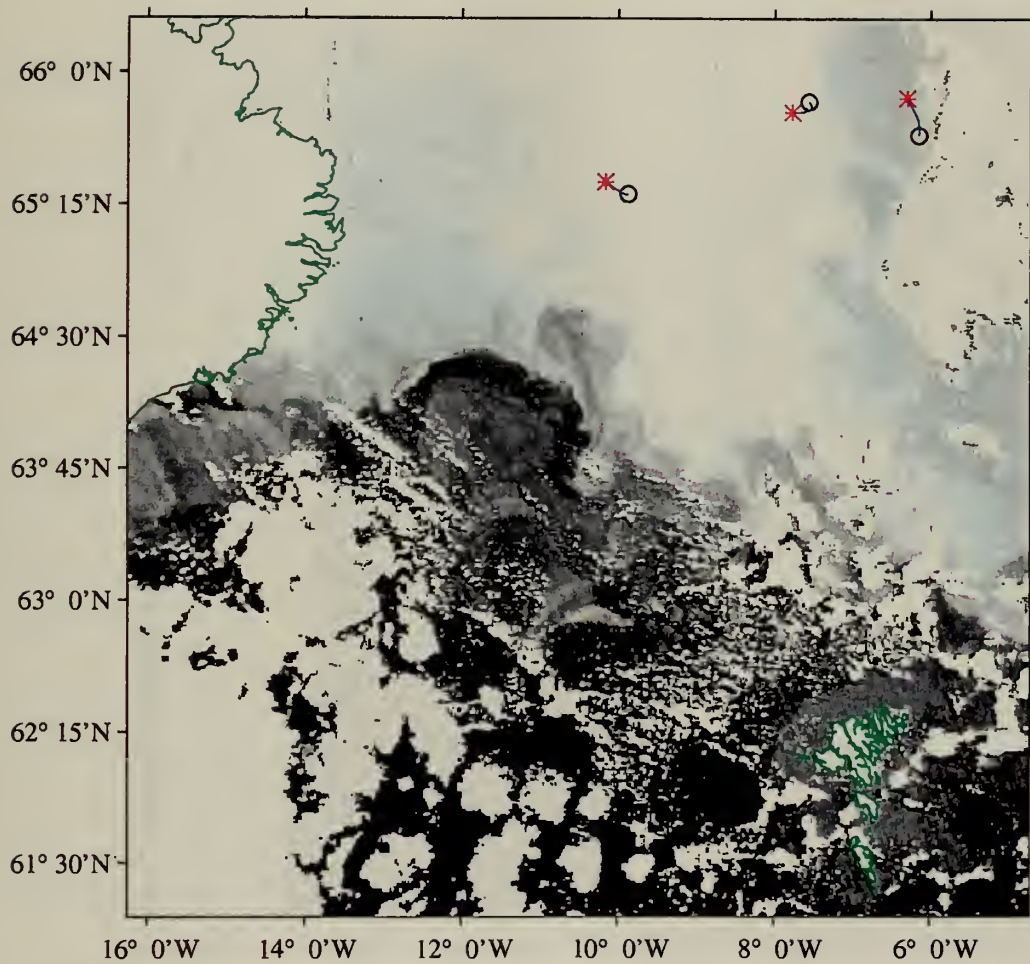


Figure 45. Same as Figure 37 for 25 December 1992 at 1429 UTC.

22 AUGUST 93: 1433 UTC

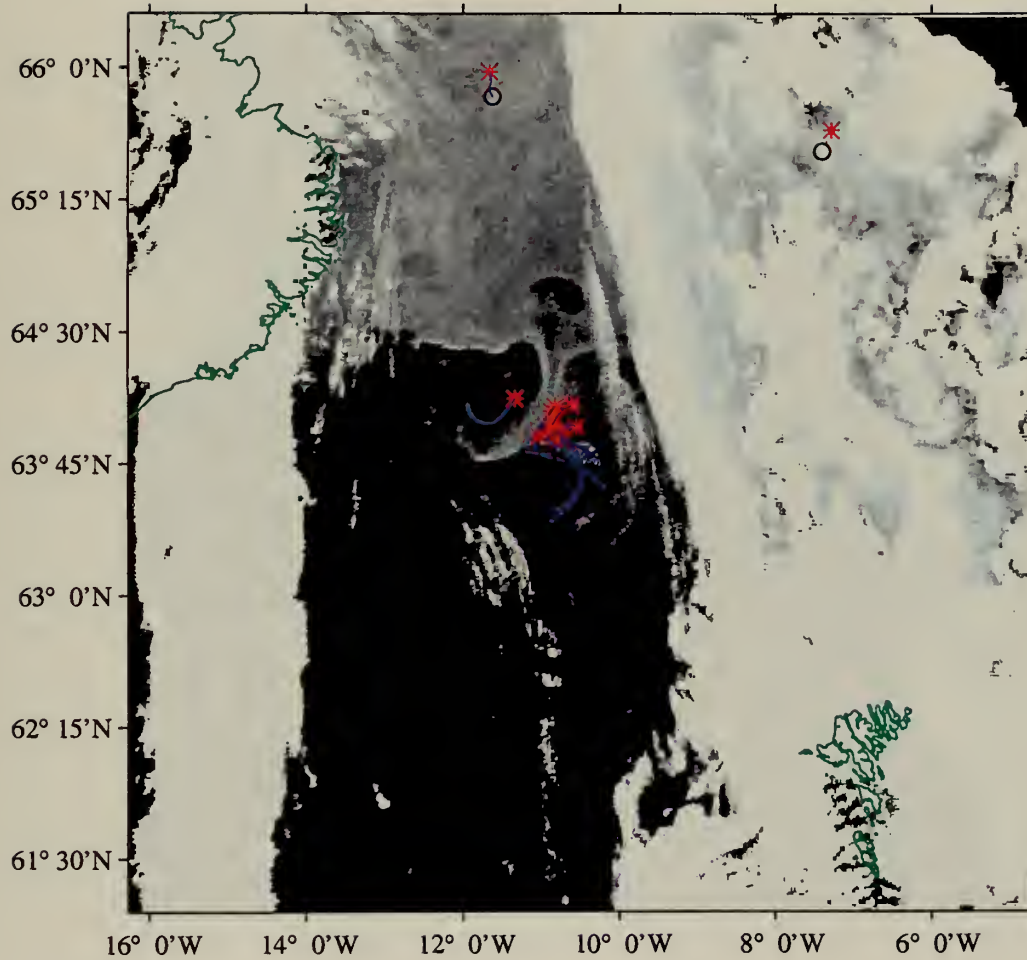


Figure 46. Same as Figure 37 for 22 August 1993 at 1433 UTC.

25 SEPTEMBER 93: 1601 UTC

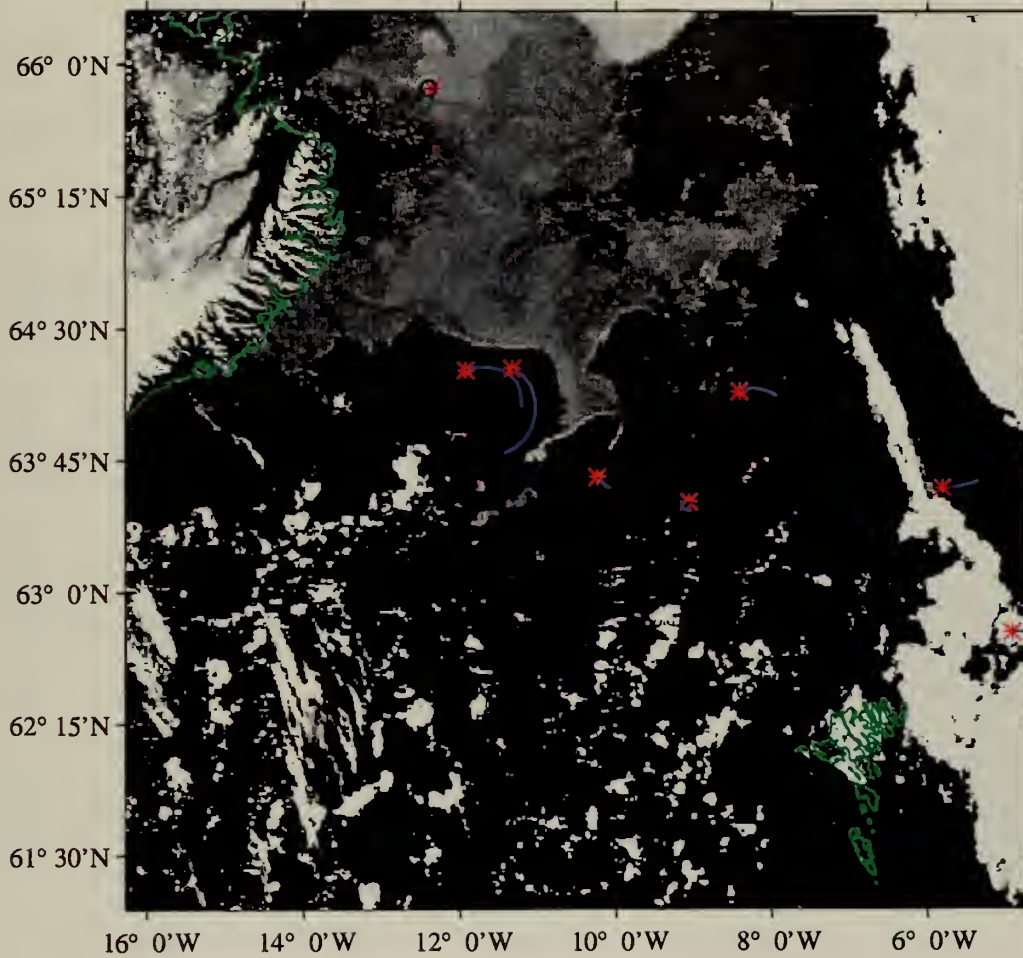


Figure 47. Same as Figure 37 for 25 September 1993 at 1601 UTC.

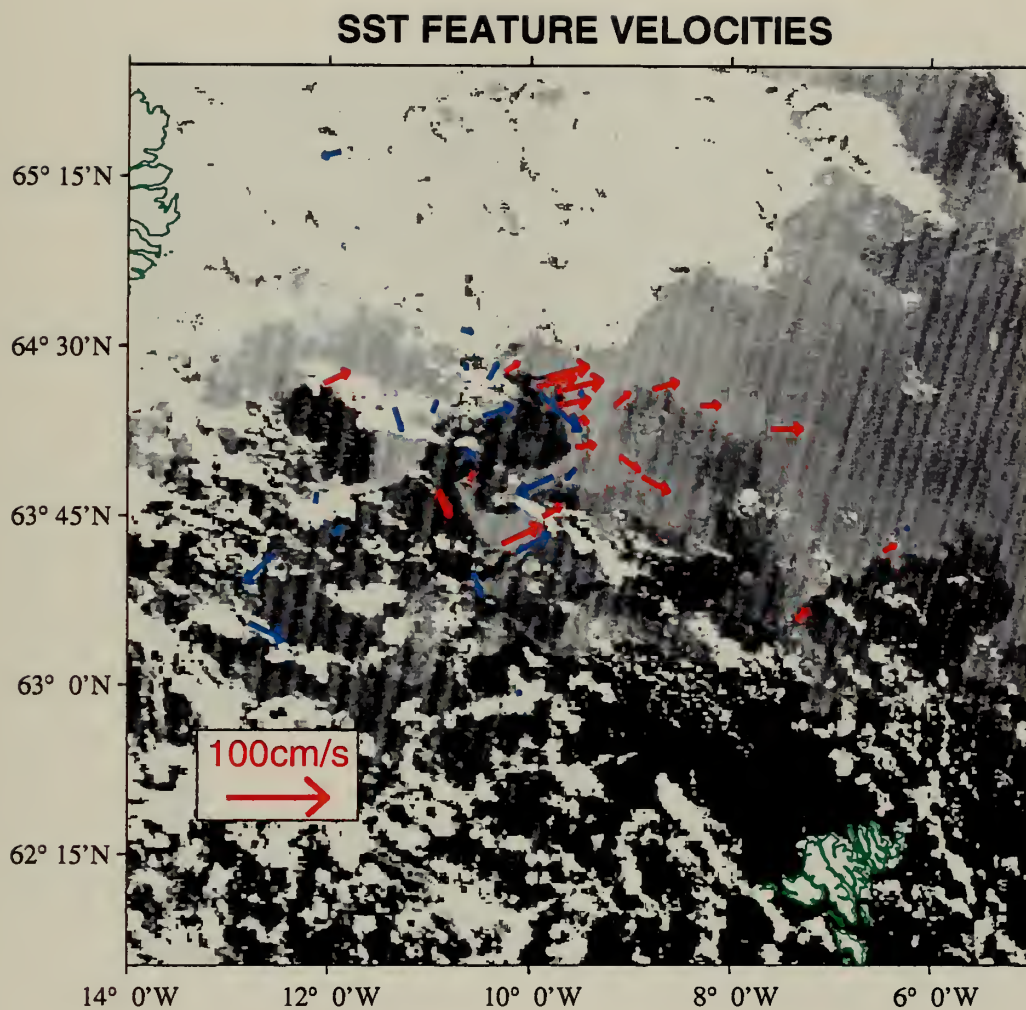


Figure 48. MCSST Image of the IFF on 24 October 1992 at 0845 UTC with Overlay Showing Surface Velocity Vectors (Red Arrows) as Estimated by Manually Tracking the Major SST features Between that Image and the Previous One (23 October 1992 at 1528 UTC). The cyan arrows are trajectories derived from the drifters.

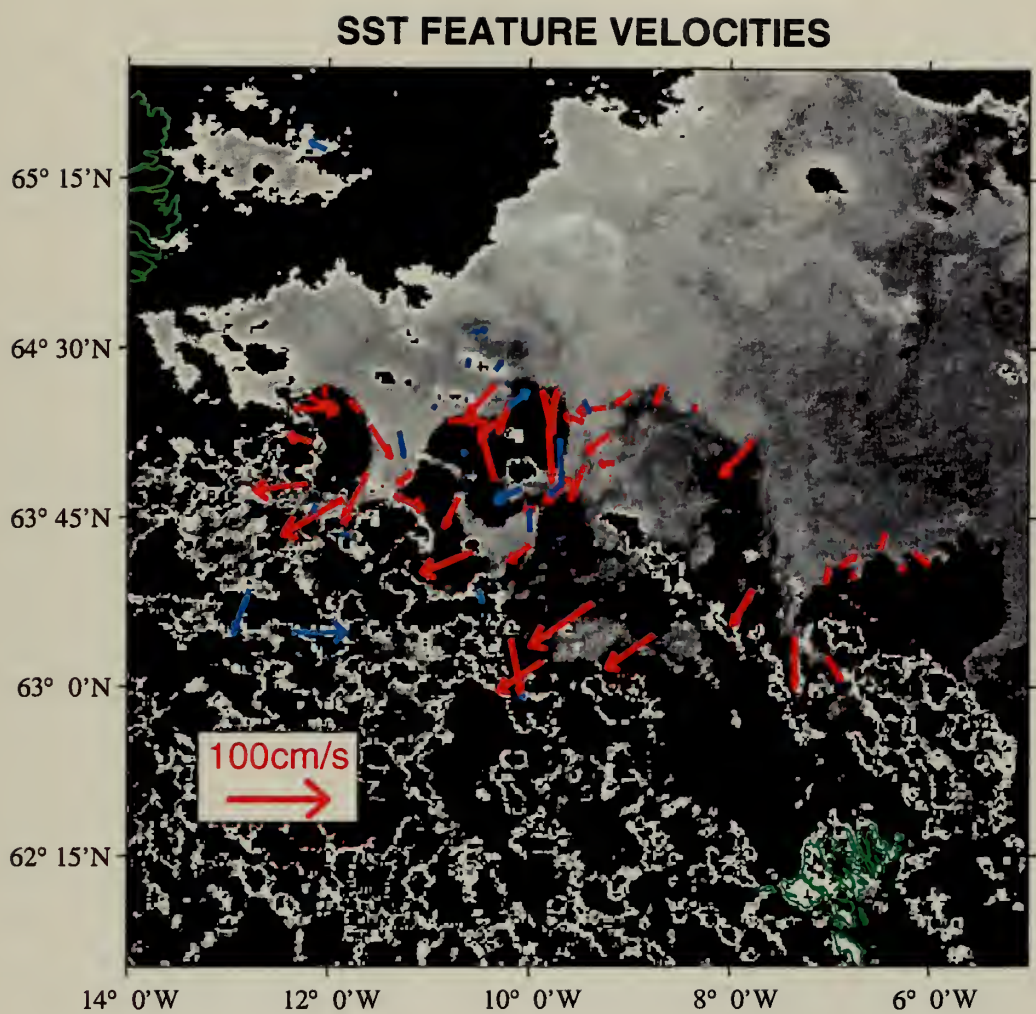


Figure 49. Same as Figure 48 for Image Pair 24 October 1992 at 0845 UTC and 24 October 1992 at 1335 UTC.

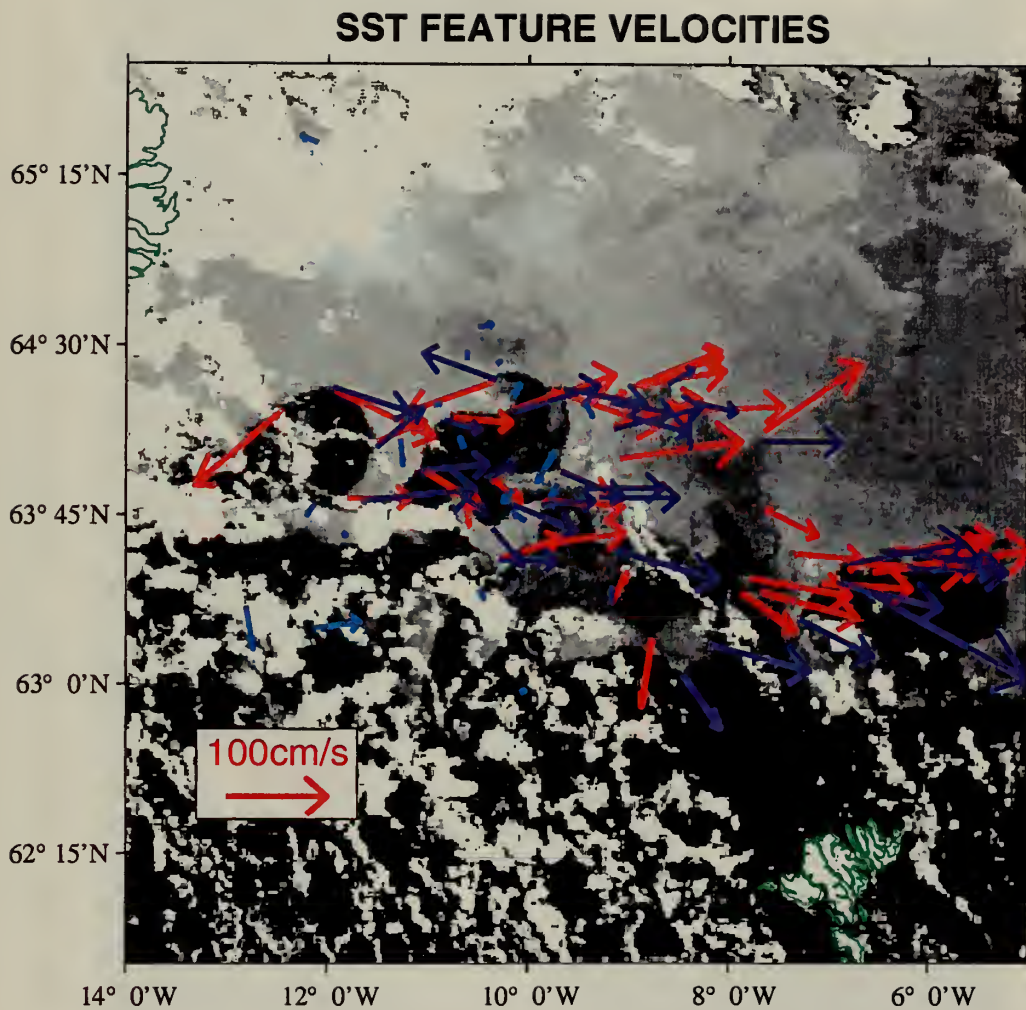


Figure 50. Same as Figure 48 for Image Pair 24 October 1992 at 1335 UTC and 24 October 1992 at 1514 UTC. Velocity vectors estimated by two independent operators are depicted with blue and red arrows.

MCSST 19OCT1435 - DRIFTER/SHIP SST 19OCT

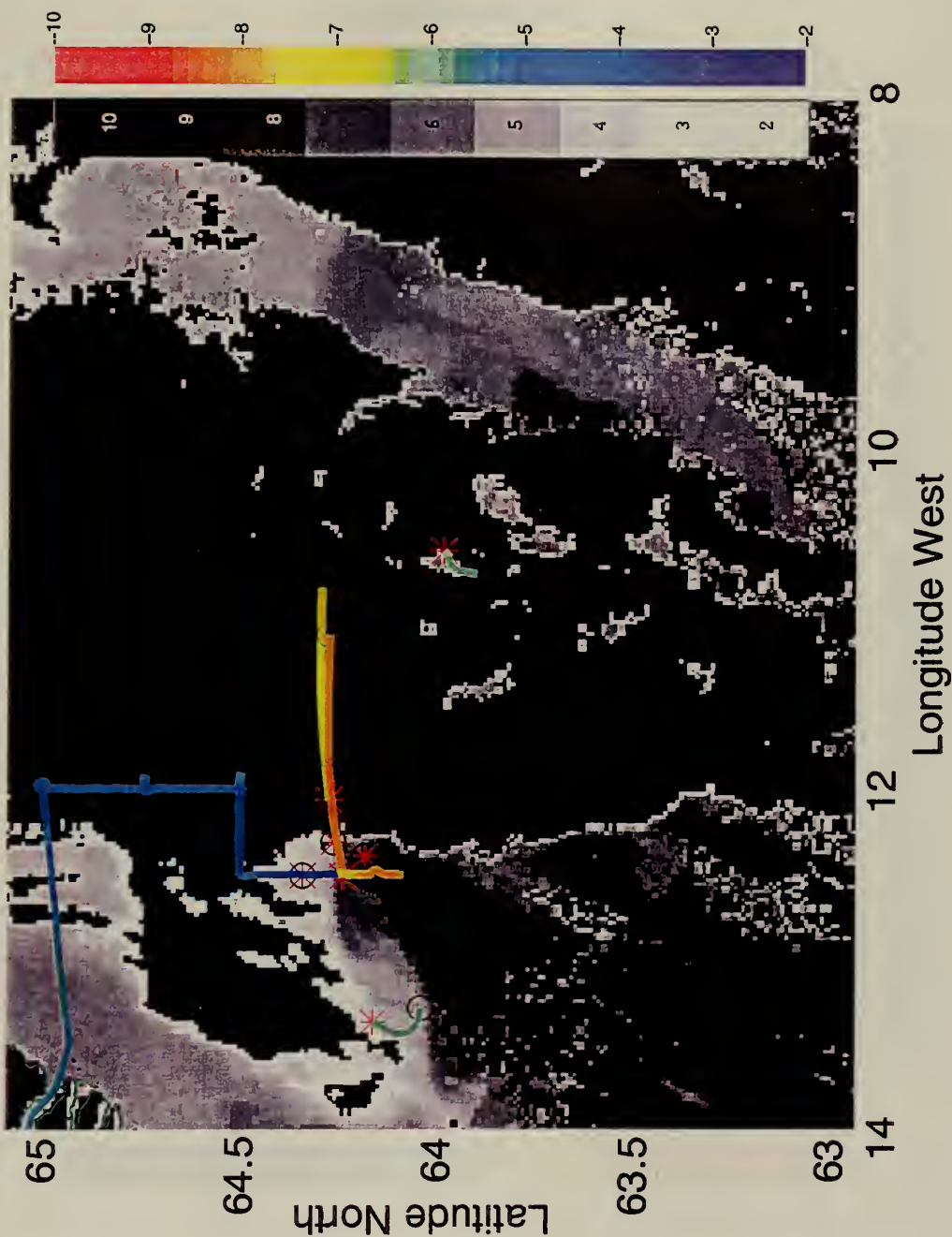


Figure 51. Close View of the IFF MCSST Field on 19 October 1992 at 1435 UTC. Cloud cover pixels are shown in black. Drifter and ship tracks for that day are overlaid on the satellite image and are color-coded with SST. The temperature scales for the satellite retrievals and the in-situ measurements are shown to the right of the image in units of degrees Celsius.

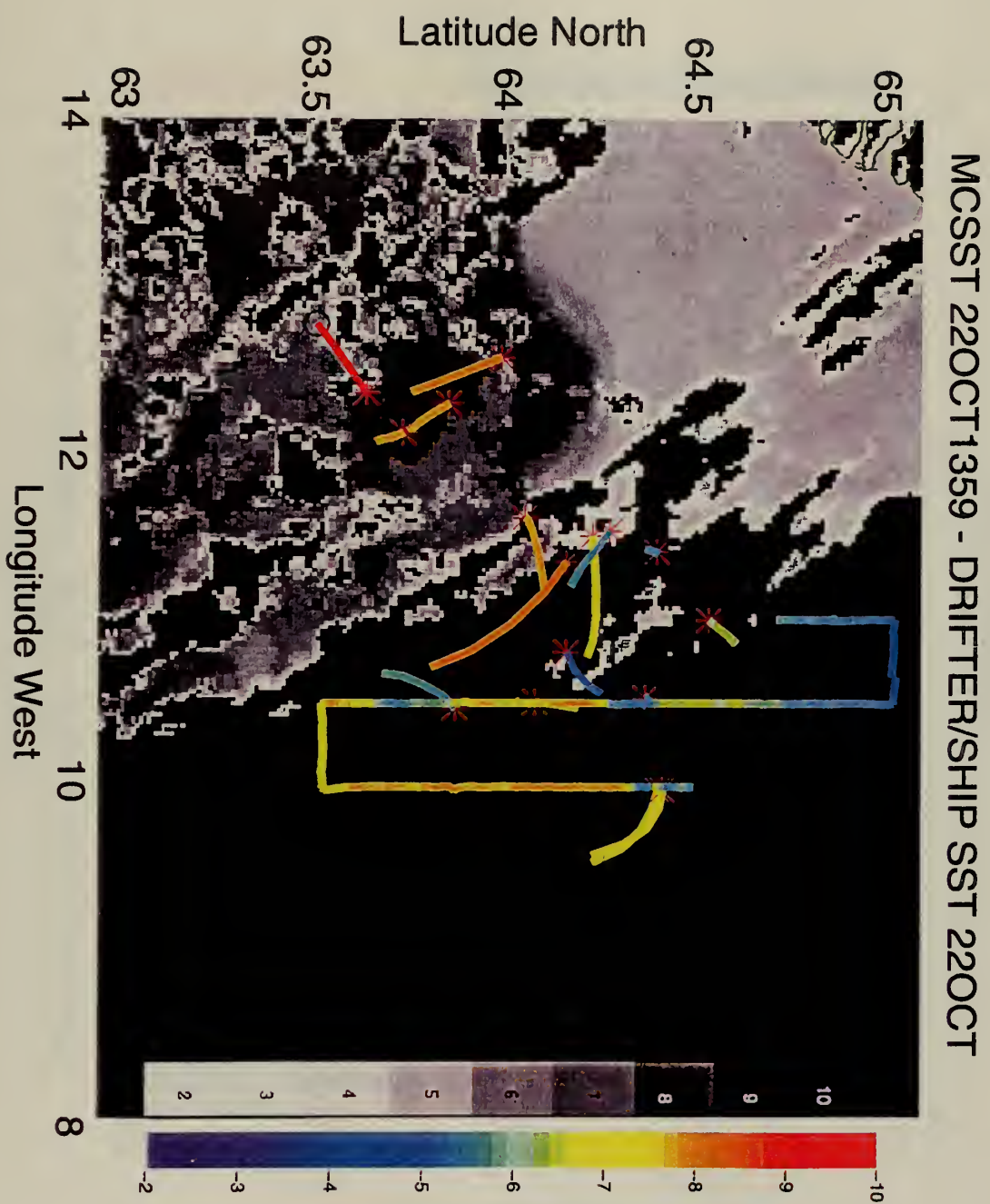


Figure 52. Same as Figure 51 for 22 October 1992 at 1359 UTC.

MCSST 23OCT1528 - DRIFTER/SHIP SST 23OCT

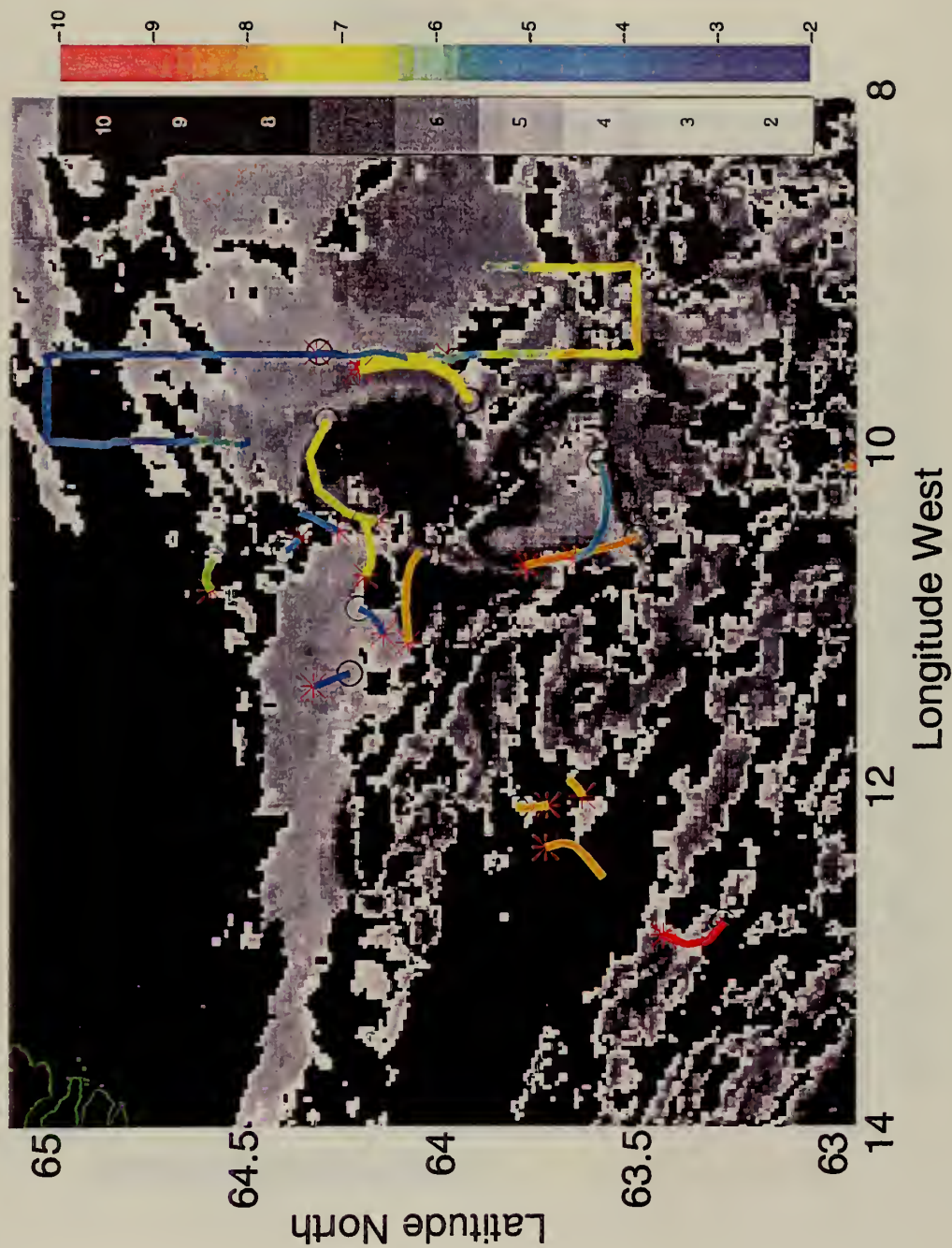


Figure 53. Same as Figure 51 for 23 October 1992 at 1528 UTC.

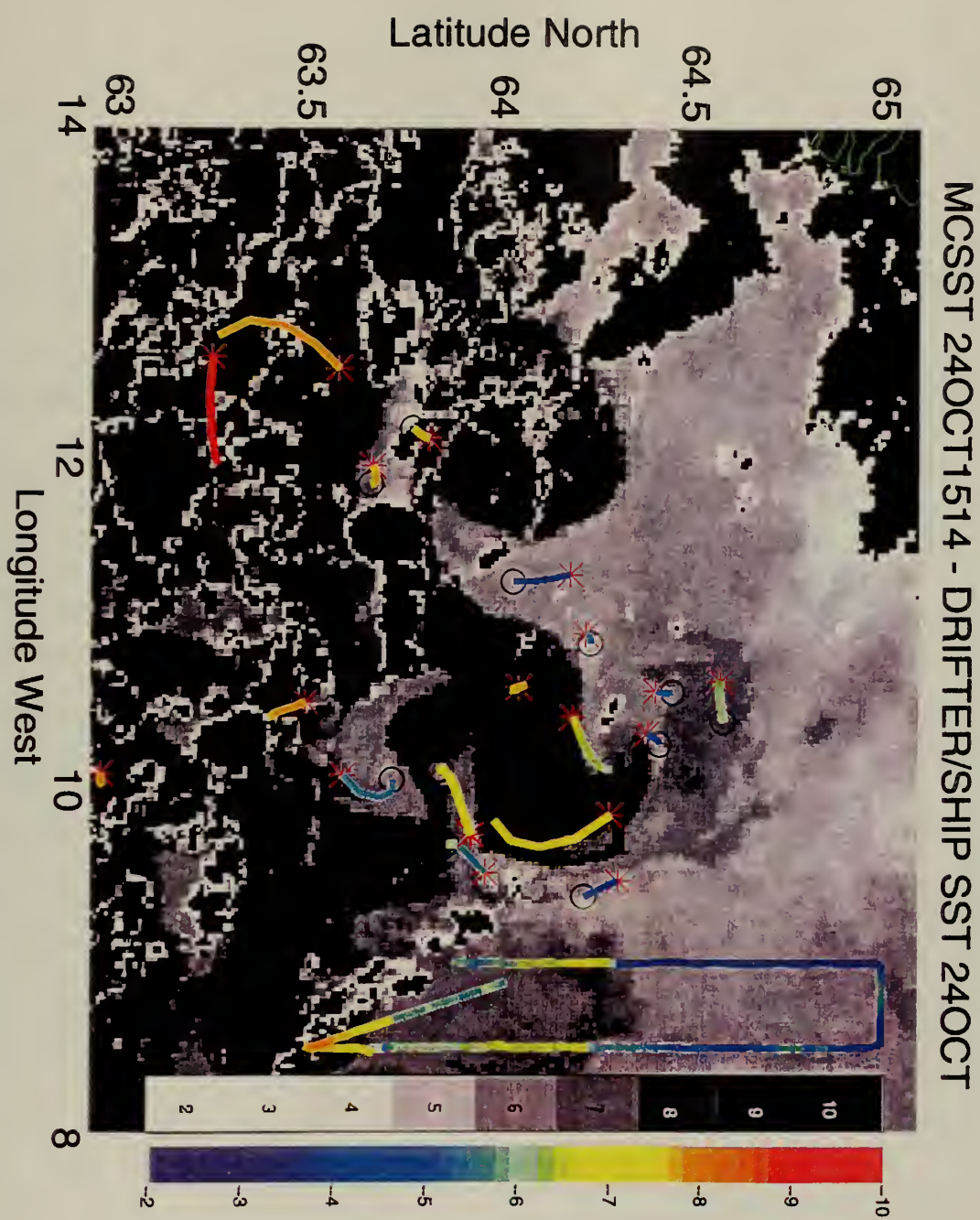


Figure 54. Same as Figure 51 for 24 October 1992 at 1514 UTC.

Table 6. Infrared Satellite Images Used from October 1992 to September 1993.

SATELLITE	DATE	TIME (UTC)	JULIAN DATE	MCSST ALGORITHM
NOAA-11	16 OCT 92	1512	655.6333	Split Window, Day
NOAA-11	19 OCT 92	1435	658.6076	Split Window, Day
NOAA-11	22 OCT 92	1359	661.5826	Split Window, Day
NOAA-11	23 OCT 92	1528	662.6444	Split Window, Day
NOAA-12	24 OCT 92	0845	663.3646	Dual Window, Day
NOAA-11	24 OCT 92	1335	663.5660	Split Window, Day
NOAA-11	24 OCT 92	1514	663.6347	Split Window, Day
NOAA-11	17 NOV 92	1347	687.5743	Split Window, Day
NOAA-11	25 DEC 92	1429	725.6035	Split Window, Day
NOAA-11	22 AUG 93	1431	965.6049	Split Window, Day
NOAA-11	25 SEP 93	1600	999.6666	Split Window, Day

DATE AND TIME (1992)	Δt (HOURS)	NUMBER OF POINTS	U (cm/s)	V (cm/s)	MEAN SPEED (cm/s)	MEAN BEARING (degrees)	RMS U (cm/s)	RMS V (cm/s)
23OCT1528 - 24OCT0845	17.28	20	23	3	23	81	12	11
24OCT0845 - 24OCT1335	4.83	48	-9	-16	19	210	24	21
24OCT1335 - 24OCT1514 Operator A	1.65	40	63	-4	63	94	47	29
24OCT1335 - 24OCT1514 Operator B	1.65	35	64	-9	65	98	42	26

Table 7. Results of SST Feature Tracking in the IFF.

V. RESULTS AND CONCLUSIONS

This thesis explored the structure and variability of the Iceland-Færoe Front (IFF) between August 1992 and December 1993 using surface drifter data and thermal satellite imagery. In particular, this study focused on the IFF variability during October 1992 when the maximum number of in-situ and remotely sensed data were obtained. Graphical analysis of drifter tracks and sea surface temperature (SST) features provided the best means of investigating the dynamics of the IFF both in qualitative and quantitative terms.

Drifter SST data were used successfully to validate satellite remotely-sensed SST. A regression analysis of the two spatially and temporally coincident data sets demonstrated an overall accuracy of less than one degree Celsius (as small as 0.1 °C for October 1992) for the satellite-retrieved temperatures. These results ensured that the radiometric SST data would be a valid tool for further quantitative analysis of the IFF. The combination of both drifter and satellite-derived temperatures is crucial to provide optimum SST maps since their respective sampling methods are complementary: satellite retrieved SST images provide instantaneous broad coverage but are limited by cloud cover. Drifter data are collected regardless of cloud cover but are limited spatially to specific locations.

Drifter displacements over the Iceland-Færoe Ridge (IFR) and in the southern GIN Sea accurately depicted the complex structures and temporal variability of the IFF and its vicinity over a year. Precise examination of the drifter trajectories revealed intricate mesoscale activity within the frontal zone comprised of intrusions, instabilities, and eddies. These SST features include both relatively warm and salty North Atlantic Water (NAW) and relatively cold and fresh GIN Sea Water patterns. Even though drifter and ship data were

limited by their respective trajectories, valuable data were collected during periods of extensive cloud coverage precluding infrared remote sensing data. Correlation between drifter tracks and the structure of satellite SST features was remarkable. Lack of coincident data, either satellite or in situ, was not necessarily a liability since each form of data provided accurate information about the flow field independently. The combination of satellite SST and drifter SST and displacement provided optimum representation of IFF surface structure and development.

SST feature tracking proved to be an effective means of estimating the flow field within a dynamic boundary such as the IFF. However, use of this method revealed it can be erroneous when the time difference between sequential satellite images is less than 6 hours. Caution should be exercised when using feature tracking without supplemental ground truth data.

IFF development was successfully sampled over a week time period (16-24 October 1992) with associated instability growth. These growth features were described by overlaying color coded drifter tracks corresponding to measured SST over the thermal satellite images. This description provided the first quantitative and high resolution description of IFF instability development over a few days. Spatial and temporal agreement between the two temperature data sets was excellent.

Areas of high mesoscale activity within the front were not completely random. Initial drifter deployments just east of the Icelandic shelf moved rapidly in a zonal direction before the flow became saturated with mesoscale features. The initial state of zonal flow followed by an intense area of instability was evident on the monthly plots. The instabilities were

eventually damped or the drifters moved out of the region of high instabilities, and the IFF returned into relatively zonal flow north-northeast of the Færoe Islands, as the IFF merged with the Norwegian Atlantic Current.

The IFF is best defined at its western end where it tends to have a steep temperature gradient in the vertical while bathymetrically controlled by the underlying IFR. A weaker gradient is evident on the eastern end, and the surface signature of the IFF varies considerably in a northerly position. Even though there is more variability at the eastern end, a large meander or intrusion of warm water was common in the central IFR near 10-11° W (Hansen and Meincke, 1979). The "knight's helmet" and "blob" instabilities developed rapidly in the warm meander. They can be associated with the warm intrusion, sometimes referred to as the "Red Square" area in the literature. Warm intrusions in this region represent a compromise between growth of instabilities arriving from the Iceland shelf and mixing farther to the east.

APPENDIX. SST DATA

Coincident SST data from in-situ drifters and AVHRR measurements (8a-8k).

Table 8a. Julian date: 655.6333

BUOY	LATITUDE (°N)	LONGITUDE (°W)	BUOY SST (°C)	SATELLITE SST (°C)
14384	67.8972	4.9401	7.5368	7.07
14386	69.9280	13.0170	4.2833	3.82
14387	66.2747	5.1657	6.8852	3.26
15915	64.3372	10.9209	5.8394	4.47
8638	68.4050	10.0707	5.3729	4.93

Table 8b. Julian date: 658.6076

BUOY	LATITUDE (°N)	LONGITUDE (°W)	BUOY SST (°C)	SATELLITE SST (°C)
15903	62.4588	9.9640	7.8907	7.47
15915	63.9739	10.6963	5.7550	5.23
2460	64.0854	13.3316	5.8120	4.57

Table 8c. Julian date: 661.5826

BUOY	LATITUDE (°N)	LONGITUDE (°W)	BUOY SST (°C)	SATELLITE SST (°C)
15895	64.186	10.6803	4.9604	4.93
15896	64.039	11.51	8.0141	7.31
15903	62.8579	10.1647	8.3855	7.97
15909	63.7743	12.2082	8.0475	7.80
15920	63.8304	12.4368	8.3627	7.64
15921	63.6676	12.0731	8.1102	7.64
2462	63.5556	12.5186	9.0978	7.39

Table 8d. Julian date: 662.6444

BUOY	LATITUDE (°N)	LONGITUDE (°W)	BUOY SST (°C)	SATELLITE SST (°C)
14384	67.4211	5.0172	6.7377	6.70
15890	64.3158	10.2039	6.6498	6.70
15893	63.9885	9.5044	5.5630	5.07
15896	64.0699	10.7464	8.0141	7.48
15897	63.5969	10.6218	8.2442	7.20
15899	64.2561	11.4098	5.0407	4.71
15902	63.7134	6.2729	6.0444	5.71
15903	62.9399	10.1658	8.6604	7.27
15914	64.5950	10.7069	6.1997	5.78
15915	63.6025	10.3427	5.4636	4.78
15926	64.3102	9.4805	4.7032	4.43
2461	64.1923	11.0165	5.2255	4.50
8633	68.9019	3.2815	6.7312	6.13
8638	68.6438	10.0551	4.3741	4.22

Table 8e. Julian date: 663.3646

BUOY	LATITUDE (°N)	LONGITUDE (°W)	BUOY SST (°C)	SATELLITE SST (°C)
15890	64.1840	9.6939	7.2517	7.07
15893	63.9266	9.5739	5.5635	5.38
15896	64.0444	10.6029	7.9641	6.88
15897	63.4811	10.5196	8.1624	6.62
15902	63.7092	6.2337	5.9633	5.31
15904	66.2871	11.1194	3.3076	1.99
15915	63.6491	10.0435	5.4434	5.12
15918	64.4265	10.5999	5.1298	4.60
15921	63.6621	11.9377	7.9555	7.20
15926	64.2909	9.4617	4.5500	4.21
2460	64.2314	10.3252	6.3126	5.57
8638	68.6625	10.0388	4.3333	4.01

Table 8f. Julian date: 663.5660

BUOY	LATITUDE (°N)	LONGITUDE (°W)	BUOY SST (°C)	SATELLITE SST (°C)
15890	64.0599	9.6558	7.4032	6.70
15893	63.9092	9.6619	5.5635	5.01
15895	64.4052	10.3291	5.0011	4.13
15896	64.0318	10.6183	7.9641	7.38
15899	64.1019	11.2352	5.0389	4.60
15902	63.7062	6.2395	5.9493	6.23
15909	63.8048	12.1391	7.7681	6.90
15914	64.5854	10.5292	6.0998	5.82
15915	63.6960	10.0545	5.4290	4.80
15918	64.4072	10.6033	5.1796	4.60
15926	64.2526	9.4279	4.5976	4.60
2460	64.2494	10.2546	6.2218	5.28
2461	64.2376	10.9422	5.3111	4.67
8638	68.6668	10.0368	4.3095	3.79

Table 8g. Julian date: 663.6347

BUOY	LATITUDE (°N)	LONGITUDE (°W)	BUOY SST (°C)	SATELLITE SST (°C)
14384	67.3335	4.8975	6.6878	7.01
15890	64.0325	9.7227	7.3559	6.84
15893	63.9001	9.7029	5.6135	5.43
15895	64.4132	10.3152	5.0011	4.59
15896	64.0310	10.6537	7.9150	7.17
15897	63.4648	10.4980	8.1818	7.34
15899	64.0834	11.2573	5.0407	4.01
15902	63.7056	6.2401	5.9444	5.51
15903	62.9369	10.1139	8.2884	7.84
15909	63.8041	12.1425	7.7632	7.09
15914	64.5880	10.5041	6.0998	5.43
15915	63.7120	10.0583	5.4241	4.76
15918	64.4089	10.6227	5.1796	4.18
15926	64.2385	9.4527	4.6000	4.43
2458	63.8790	10.1659	7.3218	5.93
2459	63.8736	10.1689	7.0885	5.93
2460	64.2555	10.2305	6.1908	5.26
2461	64.2455	10.9268	5.3164	3.68
2462	63.2748	12.2453	9.0919	7.17

Table 8h. Julian date: 687.5743

BUOY	LATITUDE (°N)	LONGITUDE (°W)	BUOY SST (°C)	SATELLITE SST (°C)
15890	63.6505	7.8109	7.0847	6.33
15895	63.1934	4.1934	5.6698	4.50
15896	63.0117	8.5800	7.2037	6.40
15897	61.9951	3.6313	6.4993	5.52
15899	63.5470	7.6630	6.8859	6.20
15903	62.5980	6.1961	7.9357	7.28
15909	62.6083	4.6548	7.5481	7.01
15914	63.4510	6.6561	4.6516	3.83
15915	63.3303	5.4657	6.7095	5.99
15918	64.3674	9.7064	3.9830	3.08
15920	62.7907	8.9344	7.7940	6.87
15921	63.5364	7.4915	7.4433	6.40
15926	63.1693	4.1211	5.6500	5.11
2459	63.4775	7.8116	7.7645	6.33
2460	63.9592	7.4587	5.2908	3.49

Table 8i. Julian date: 725.6035

BUOY	LATITUDE (°N)	LONGITUDE (°W)	BUOY SST (°C)	SATELLITE SST (°C)
14384	65.6642	6.1468	4.2909	3.57
15904	67.1759	7.1471	4.3625	3.94
15912	65.3153	9.9078	1.9350	1.59
15918	62.3708	2.5861	5.1796	5.05

Table 8j. Julian date: 965.6049

BUOY	LATITUDE (°N)	LONGITUDE (°W)	BUOY SST (°C)	SATELLITE SST (°C)
15916	65.8494	11.6421	5.6393	5.67
20321	63.7996	10.4274	5.8500	6.48
20323	63.8324	10.9785	8.1761	8.75
20324	63.8456	10.8941	6.4419	6.97
20326	63.6996	10.4431	8.3810	9.57
20328	63.7746	10.3057	5.9499	6.32
20329	63.8309	11.0060	8.1000	8.27
20333	63.8741	10.9554	6.5379	6.64
2465	63.4808	10.7790	8.0795	8.43
2466	64.0478	11.9167	8.0301	8.27
5581	63.8277	10.4628	5.8866	6.32
5582	63.7898	10.4872	5.9390	6.64
5587	63.5340	10.6900	8.2728	8.59
5588	63.9885	13.0104	8.1147	10.38

Table 8k. Julian date: 999.6666

BUOY	LATITUDE (°N)	LONGITUDE (°W)	BUOY SST (°C)	SATELLITE SST (°C)
15916	65.8603	12.3558	5.5884	5.59
20321	64.1408	8.0132	7.5032	8.20
20324	63.4766	9.1167	7.8477	8.37
20326	62.6209	2.7470	9.2261	10.64
20329	62.9580	4.6367	8.1435	9.33
20333	63.6012	10.1400	8.2354	8.98
2465	64.1203	11.2313	9.3192	10.03
2466	63.8535	11.2729	9.1752	9.77
5581	63.6392	5.4455	7.4943	8.72
5583	63.5360	7.3303	8.2303	9.16
5587	62.2830	2.9688	8.7304	10.20
5588	64.2303	8.7769	7.0503	7.07

LIST OF REFERENCES

- Allen, J.T., D.A. Smeed, and A.L. Chadwick, "Eddies and Mixing at the Iceland-Færoe Front," *Deep-Sea Res.*, 41, 51-79, 1994.
- Becker, G., K. Huber, K.P. Koltermann, and E. Mittelstaedt, "Meereskundliche Beobachtungen und Ergebnisse," *Meteor-Fahrt*, 20a, Nr. 37, Seegebiet Faroer, 1973.
- Borenås, K., and P.A. Lundberg, "On the Deep-Water Flow Through the Færoe Bank Channel," *J. Geophys. Res.*, 93, 1281-1292, 1988.
- Emery, W.J., C. Fowler, and C.A. Clayson, "Satellite-Image-Derived Gulf Stream Currents Compared with Numerical Model Results," *J. Ocean Atmos. Oceanic Technol.*, 9, 286-304, 1992.
- Essen, H.H., E. Nacini, and P.-M. Poulain, "Comparison of Satellite-Retrieved Sea Surface Temperatures with Drifter and Ship Borne Measurements," *SACLANTCEN Memo. SM-297*, 29 pp., SACLANT Undersea Research Center, La Spezia, 1996.
- Gould, W.J., J.F. Read, and J. Smithers, "SEASOAR Profiles in the Iceland-Scotland Area," *Inst. of Oceanogr. Sci., Rep.253*, 50 pp., Wormley, England, 1987.
- GSP Group, "A Venture Toward Improved Understanding of the Ocean's Role in Climate," *EOS Trans. AGU*, 71 (24), 75-755, 1990.
- Hallock, Z.R., "Variability of Frontal Structure in the Southern Norwegian Sea," *J. Phys. Oceanogr.*, 15, 1245-1254, 1985.
- Hansen, B., and J. Meincke, "Eddies and Meanders in the Iceland-Færoe Ridge Area," *Deep Sea Res.*, 26A, 1067-1082, 1979.
- Hansen, D.V., and A. Herman, "Temporal Sampling Requirements for Surface Drifting Buoys in the Tropical Pacific," *J. Ocean Atmos. Oceanic Technol.*, 6, 599-607, 1989.
- Hansen, D.V., and P.-M. Poulain, "Processing of WOCE/TOGA drifter data," *J. Ocean Atmos. Oceanic Technol.*, 13, 900-909, 1997.
- Hopkins, T.S., "The GIN Sea: A Synthesis of its Physical Oceanography and Literature Review 1972-1985," *Earth-Science Reviews*, 30, 175-318, 1991.
- Kidder, S. Q. and Vonder Haar, T. H. Satellite Meteorology: An Introduction. Academic Press, San Diego, CA., 1995.

Koltermann, K.P., J. Meincke, and T. Müller, "Overflow '73," Meteor and Meerkatze 2, Berichte des Instituts für Meereskunde, 23, 88 pp., 1976.

Krauss, W., "Currents and Mixing in the Irminger Sea and in the Iceland Basin," *J. Geophys. Res.*, 100, 10851-10871, 1995.

Krauss, W., R. Döschner, A. Lehmann, and T. Viehoff, "On Eddy Scales in the Eastern and Northern North Atlantic Ocean as a Function of Latitude," *J. Geophys. Res.*, 95, 18049-18056, 1990.

Malmberg, S., "Hydrographic Conditions in the East Icelandic Current and Sea Ice in North Icelandic waters," 1970-1980, *Rapp. P.-V. Reun. Cons. Int. Explor. Mer*, 185, 170-178, 1984.

Maskell, S.J., A.D. Heathershaw, and C.E. Stretch, "Topographic and Eddy Effects in a Primitive Equation Model of the Iceland-Færoes Front," *J. Marine Systems*, 3, 343-380, 1992.

Miller, A.J., P.-M. Poulain, A.R. Robinson, H.G. Arango, W.G. Leslie, and A. Warn-Varnas, "Quantitative Skill of Quasi-Geostrophic Forecasts of a Baroclinically Unstable Iceland-Færoe Front," *J. Geophys. Res.*, 100, 10833-10849, 1995a.

Miller, A.J., H.G. Arango, A.R. Robinson, W.G. Leslie, P.-M. Poulain, and A. Warn-Varnas, "Quasi-Geostrophic Forecasting and Physical Processes of Iceland-Færoe Frontal Variability," *J. Phys. Oceanogr.*, 25, 1273-1295, 1995b.

Minnett, P.J., "Consequences of Sea Surface Temperature Variability on the Validation and Applications of Satellite Measurements," *J. Geophys. Res.*, 96, 18475-18489, 1991.

Minnett, P.J., "The Regional Optimization of Infrared Measurements of Sea Surface Temperature From Space," *J. Geophys. Res.*, 95, 13497-13510, 1990.

Minnett, P.J., "A Numerical Study of the Effects of Anomalous North Atlantic Atmospheric Conditions on the Infrared Measurement of Sea Surface Temperature From Space," *J. Geophys. Res.*, 91, 8509-8521, 1986.

Niiler, P.P., S. Piacsek, L. Neuberg, and A. Warn-Varnas, "Sea Surface Temperature Variability of the Iceland-Færoe Front," *J. Geophys. Res.*, 97, 17777-17785, 1992.

Niiler, P.P., A.S. Sybrandy, K. Bi, P.-M. Poulain, and D. Bitterman, "Measurements of the Water Following Capability of Holey-Sock and TRISTAR Drifters," *Deep Sea Res.*, 42, 1951-1964, 1995.

Østerhus, 1991, unpublished notes.

Poulain, P.-M., A. Warn-Varnas, and P.P. Niiler, "Near-Surface Circulation of the Nordic Seas as Measured by Lagrangian Drifters," *J. Geophys. Res.*, 101, 18237-18258, 1996a.

Poulain, P.-M., P. Zanasca, and A. Warn-Varnas, "Drifter Observations in the Nordic Seas (1991-1995) Data Report," *SACLANTCEN Memo. SM-299*, 89 pp., SACLANT Undersea Research Center, La Spezia, 1996b.

Peggion, G., "Interpretation and Representation of the Synoptic Features in the Iceland-Færoe-Shetland Region," *SACLANTCEN Memo. SM-269*, 70 pp., SACLANT Undersea Research Center, La Spezia, 1993.

Perkins, H., T. S. Hopkins, S. A. Malmberg, P.-M. Poulain, and A. Warn-Varnas, "Oceanographic Conditions East of Iceland," *J. Geophys. Res.*, in press, 1997.

Robinson, A.R., H.G. Arango, A.J. Miller, A. Warn-Varnas, P.-M. Poulain, and W.G. Leslie, "Real-Time Operational Forecasting on Shipboard of the Iceland-Færoe Frontal Variability," *Bull. Amer. Meteor. Soc.*, 77, 243-258, 1996.

Ruddick, B.R., and J.S. Turner, "The Vertical Scale of Double-Diffusive Intrusions," *Deep Sea Res.*, 26A, 903-913, 1979.

Saunders, P.M., "Cold Outflow from the Færoe Bank Channel," *J. Phys. Oceanogr.*, 20, 29-43, 1990.

Scott, J.C., and N.A. Lane, "Frontal Boundaries and Eddies on the Iceland-Færoe Ridge," in *Proceedings on Ocean Variability and Acoustic Propagation*, edited by Kluwer Academic, Boston, Mass., 449-461, 1990.

Smart, J.H., "Spatial Variability of Major Frontal Systems in the North Atlantic-Norwegian Sea Area: 1980-81," *J. Phys. Oceanogr.*, 14, 185-192, 1984.

Steele, J.H., J.R. Barrett, and L.V. Worthington, "Deep Currents South of Iceland," *Deep Sea Res.*, 9, 465-474, 1962.

Stefansson, U., "Near-Shore Fluctuations of the Frontal Zone Southeast of Iceland," *Rapports et Porces-Verbaux*, 162, 201-205, 1972.

Sybrandy, A.L., and P.P. Niiler, "WOCE/TOGA Lagrangian Drifter Construction Manual," *SIO Ref. 91/6, WOCE Rep. 63*, 58pp., Scripps Inst. of Oceanogr., La Jolla, Calif., 1991.

Veronis, G., "On Properties of Seawater Defined by Temperature, Salinity and Pressure," *J. Marine Res.*, 30, 227-255, 1972.

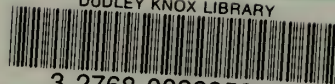
Willebrand, J., and J. Meincke, "Statistical Analysis of Fluctuations in the Iceland-Scotland Frontal Zone," *Deep Sea Res.*, 27A, 1047-1066, 1980.

INITIAL DISTRIBUTION LIST

1.	Defense Technical Information Center	2
	8725 John J. Kingman Road, Ste 0944	
	Ft. Belvoir, Virginia 22060-6218	
2.	Dudley Knox Library	2
	Naval Postgraduate School	
	411 Dyer Rd.	
	Monterey, California 93943-5101	
3.	Chairman, Code OC	2
	Department of Oceanography	
	Naval Postgraduate School	
	Monterey, California 93943-5002	
4.	Professor Pierre-Marie Poulain (Code OC/PN)	4
	Department of Oceanography	
	Naval Postgraduate School	
	Monterey, California 93943-5002	
5.	Director	1
	SACLANT Undersea Research Centre	
	SACLANTCEN CMR_426	
	APO-AE 09613-5000	
6.	LT Christopher J. Arends	4
	Naval Pacific Meteorology and Oceanography Facility	
	Box 357076	
	San Diego, California 92135-7076	

AND LIBRARY
ROYAL POSTGRADUATE SCHOOL
MONTEREY CA 93943-5101

DUDLEY KNOX LIBRARY



3 2768 00338536 0